A Study of the Interactions of Elementary Particles

Ian F. Corbett

Linacre House

Thesis Presented to the
University of Oxford
for the Degree of
Doctor of Philosophy

July, 1965

ABSTRACT

This thesis describes an experiment to investigate the reaction

$$p + p \rightarrow p + p + \pi^o$$

at 1 GeV incident proton energy. Optical spark chambers and scintillation counters were used to detect the final state protons. The geometry of the apparatus was such as to select events in which one of the protons had kinetic energy (T) between 50 MeV and 200 MeV and in which the invariant mass (ω) of the other proton + pion lay in the range ~ 1150 MeV to ~ 1300 MeV. Aluminium absorbers between spark chambers were used to measure T to $\pm$ 3.6 MeV. Events with 1185 $\leq \omega <$ 1285 MeV were selected for full analysis, and the variation of the reaction cross-section with and T is compared with the predictions of the one pion exchange (OPE) model. The data is in good agreement with calculations which take into account the virtual nature of the exchanged pion.

A Chew-Low extrapolation to the one pion exchange pole yields values for the $\pi^o p$ elastic scattering cross-section, averaged over ω in the ranges 1215 - 1245 MeV and 1245 - 1285 MeV, of -5.5 ± 132 mb and 84.2 ± 153 mb. These are compatible with cross-sections calculated from pion nucleon phase shifts.

A review of the scope and limitations of the OPE model and, more generally, the peripheral model, is given. This includes a discussion of the influence of absorption processes.

Acknowledgements

An experiment of the nature of this one can only be completed with the assistance and co-operation of many people. First of all the author would like to thank his supervisor, Dr. W.S.C. Williams, for his interest, encouragement and help throughout the past three years, and to thank other members, past and present, of the Oxford High Energy Physics (Spark Chambers) Group: Dr. A.B. Clegg, Dr. C.M.P. Johnson, Dr. R. Middlemas, C.J.S. Damerell, Dr. J.C. Madden and J.E. Swannack. His debt to all these is considerable.

The bulk of the work was carried out at the Nuclear Physics Laboratory of the University of Oxford, and the author would like to thank Professor D.H. Wilkinson F.R.S. for his hospitality.

The author is grateful to Professors P.B. Moon F.R.S. and W.E. Burcham F.R.S. of Birmingham University for the use of the proton synchrotron and other facilities of the Physics Department, to Dr. J. Dowell and Dr. B. Musgrave who designed and built the beam, to Dr. R. Van der Raay for the loan of equipment, and to the operating staff of the synchrotron, who provided the protons. Most of the equipment used was built in the Oxford laboratory workshops, under Mr. S.A. Tolan.

The initial stages of the computing were done on the Oxford Computing Laboratory "Mercury" computer, under Professor L. Fox, and the final stages on the "Atlas" computer at Chilton, Berkshire. The author would like to thank the operating staff at these installations for their assistance and co-operation, and Dr. Howlett for the use of the facilities of the "Atlas" Laboratory.

This thesis was typed by Miss G. Wymer, who certainly deserves the author's thanks. The photographs and duplication of diagrams were the work of Mr. C. Band of the Clarendon Laboratory.

While this research was carried out the author was supported by a D.S.I.R. Studentship.

Chapter 1 Introduction

This thesis describes the design, performance and analysis of an experiment to investigate neutral pi-meson production in proton-proton collisions at 1 GeV incident proton energy. At this energy single pion production dominates, and this was the process investigated. A small part of the allowed kinematic region was selected by the design of the experiment.

The reaction

$$p + p \rightarrow p + p + \pi^{0}$$

is one of a class of reactions, the so-called peripheral processes, apparently involving one particle exchange, which seem to dominate inelastic processes. Such reactions have been subjected to considerable theoretical investigation, the extent of which is outlined in chapter 2 with particular reference to the contributions of Ferrari and Selleri to the understanding of single pion production in nucleon-nucleon collisions.

The experiment, to be described in chapters 4 and 5, was intended to investigate the applicability of the Chew-Low extrapolation procedure to this reaction and to test the validity of the Ferrari-Selleri one pion exchange calculations which, at the time of the design of the experiment, were in fair agreement with bubble chamber data on the associated reaction

$$p + p \rightarrow p + n + \pi^+$$

at 0.97 GeV. Optical spark chamber and scintillation counter techniques were used to obtain, it was hoped, a large sample of interactions in the kinematical region selected. However, because of detection biasses only a small fraction of the events recorded could be used. This is a general limiting feature of the spark chamber technique.

The experiment was performed in summer 1963 and since that time, while it was being analysed, the calculations of Ferrari and Selleri have been refined and bubble chamber data on $pp \rightarrow pp\pi^0$ at 1 GeV has been published. The agreement between theory, with a somewhat ad hoc cut-off function, and experiment is good; the results of this experiment confirm this agreement over the narrower kinematical region covered.

Recent theoretical developments, discussed in chapter 2, involving explicit consideration of the influence of absorptive processes in the initial and final channels lead to the belief that the cut-off function procedure used in Ferrari-Selleri type calculations is little removed from curve fitting, being an empirical representation of the effects of many processes on the initial and final channels. This view is strengthened by the evaluation in chapter 6 of the expected one pion exchange distributions for the reaction $pp \rightarrow pp\pi^0$ by three different methods, two being rather crude approximations, the other more sophisticated. Suitable choice of a cut-off function for each method allows the data of this experiment, and of the bubble chamber experiment, to be fitted.

In the one pion exchange model the cut-off function required should be indepandent of the incident proton energy. This would not appear to be true of the functions needed for the less sophisticated calculations but would appear to be true of the latest Ferrari-Selleri calculations. This implies that the basic ideas of the one pion exchange model are sound, and that the modification to its predictions, possibly caused by absorption, can be represented by an empirical factor only slowly varying with the incident proton energy. No absorption model calculations have been made for nucleon-nucleon collisions, but this would appear to be inagreement with qualitative expectations based on absorptive considerations since the total pp inelastic cross-section, which indicates the strength of the absorptive channels, is very nearly constant at high energies.

Absolute cross-sections from this experiment are in some doubt because of normalisation uncertainties so the best that can be said is that the results are in agreement with one pion exchange predictions normalised to bubble chamber data.

An attempt to extract the $\pi^{o}p$ elastic scattering cross-section at two energies by means of the Chew-Low extrapolation procedure was hampered by the poor statistical accuracy of the data and the range of the extrapolation. The results were consistent with cross-sections calculated from pion-nucleon phase shifts.

Chapter 2

This chapter will comprise a discussion of pion production in nucleon-nucleon interactions. These processes appear to be well described by the peripheral model, so some space will be devoted to a consideration of the general principles of this model.

Throughout the chapter a nucleon, neutron or proton, will be denoted by N, an anti-nucleon by $\bar{N}$, and the nucleon mass by m. The pi-meson (π) mass will be denoted by μ. Reactions will be written without "+" signs between particles e.g. NN $\rightarrow$ NNπ denotes an interaction in which a single pion is produced in a nucleon-nucleon collision. Full charge independence will be assumed.

2.1 Early Ideas

Cosmic ray work (1) first showed that pions were produced in nucleon-nucleon collisions. To explain such high energy interactions Fermi (2) advanced a statistical theory which proposed that in any such interaction thermodymamic equilibrium was established inside an interaction volume of radius equal to the range of nuclear forces. The relative probability of a given final state was taken to be proportional to the phase space available to it; that is, nuclear interactions were ignored except in so far as they established equilibrium and all final state matrix elements were assumed to be identical. This theory agreed fairly well with cosmic ray data, but not with the more accurate work of Lindenbaum and Yuan (3) on pion production in proton-beryllium and proton-proton collisions at 1.0 - 3.0 GeV. They suggested that the dominant process was the excitation of one, or both, of the nucleons to the I, $J^P = 3/2, 3/2^+$ 1238 MeV isobar ($N^*(1238)$), followed by its subsequent decay into nucleon plus pion.

The existence of this isobar had early been shown in $\pi^\pm p$ scattering (4) where it appears as a peak in the I = 3/2 cross-section at an incident pion energy of approximately 200 MeV. At this energy the $\pi^+ p$ elastic scattering cross-section is only slightly larger than the limit for pure J=3/2 elastic scattering and the angular distribution is very near the $1 + 3\cos^2\theta$ expected of J=3/2. Since the I=1/2 cross-section does not show this peak the conclusion, confirmed by phase shift analysis (4), is that there is an I=3/2, $p_{3/2}$ pion nucleon excited state at ~ 1238 MeV (the mass at which the resonant phase shift = $\pi/2$).

Kovacs (5) modified the statistical model to take into account final state interactions between pion and nucleon and on the basis of $N^*(1238)$ isobar dominance Peaslee (6) deduced the ratios of π^+, π^-, π^0 mesons expected in either single or double production by applying the principle of conservation of isotopic spin. The predictions of both Kovacs and Peaslee were in much better agreement with the data than the statistical theory.

Lindenbaum and Sternheimer (7) then advanced the 'isobar model', superseding the approach of Kovacs. In this model one pion production is simply

$$NN \rightarrow NN^{*}, \qquad N^{*} \rightarrow N\pi \tag{2.1.1}$$

and the probability P of exciting an isobar of mass ω is

$$\frac{dP(\omega)}{d\omega} \propto F(\omega, W)\ \sigma_{\pi N}(\omega) \tag{2.1.2}$$

where W is the total centre of mass energy available and $F(\omega, W)$ is the two-body phase-space for isobar production. $\sigma_{\pi N}(\omega)$ is the πN scattering cross-section at a pion-nucleon centre of mass energy ω.

By assuming specific angular distributions for N^{*} production and decay (for which the model can make no predictions) the spectrum of all final state particles was calculated; agreement with experiment was very good for the distributions in ω, rather less good for the distribution in kinetic energy of the reaction products.

Conservation of isotopic spin, applied to reaction (2.1.1) makes definite predictions for the ratios of π^{+}, π^{-}, π^{0} in the final states. Considering pp collisions as an example, the isobar model predicts

$$\frac{pp \rightarrow pn\pi^{+}}{pp \rightarrow pp\pi^{0}} = \frac{5}{1} \tag{2.1.3}$$

Any deviation from this indicates that channels other than $N^{*}(1238)N$ are of importance. The experimental values, at various energies, are

$$4.95 \pm 0.5 \quad \text{at} \quad 1 \text{ GeV } (8),$$
$$4.17 \pm 0.25 \quad \text{at} \quad 2 \text{ GeV } (9) \text{ and}$$
$$3.95 \pm 0.48 \quad \text{at} \quad 2.85 \text{ GeV } (10).$$

That is, the I=1/2 channel which can contribute strongly to the $p\pi^o$ relative states in $pp \rightarrow pp\pi^o$ becomes more important as energy increases. This is in agreement with pion nucleon scattering data, which shows a steady increase in the I=1/2 total cross-section up to about 1700 MeV, and the existence of two I=1/2 resonances at 1512 MeV and 1688 MeV. (In fact, at very high incident energies ($\gtrsim$5 GeV) the N^*(1238) resonance seems scarcely excited at all (11).) Lindenbaum and Sternheimer extended their model to take into account the I=1/2 resonances (12) and applied the results with some success to pion-nucleon inelastic processes.

2.2 Chew-Low Extrapolation

The isobar model does not include any details of the interaction mechanism leading to isobar production. Similarly the approach of Chew and Low (13) does not consider the detailed dynamics of the interaction, but provides a recipe for isolating the contributions of certain pole terms in the S-matrix element linking the reaction initial and final states.

Any S-matrix element can be considered as the sum of the contributions of many Feynmann diagrams (though this should not be taken too literally as such summations involving strong interactions are notoriously divergent).

If the diagram of Fig. 2.2.1 can contribute to the process $aB \rightarrow Cab$ (which implies that $B\bar{C}$ has the same quantum numbers as b) then the overall S-matrix element for the process will contain a term, the contribution of this diagram, of the form

$$M = M_{BC} \frac{1}{\Delta^2 + m_b^2} M_{ab} \qquad (2.2.1)$$

Here M_{BC}, M_{ab} are the matrix elements corresponding to the upper and lower vertices linked by the propagator for the exchange of the virtual particle b (of mass m_b). Δ^2, the 4-momentum transfer between B and C, squared, is defined by

$$\Delta^2 = (p_C - p_B)^2$$

where the p's are the 4-momenta of the subscript particles. M has a pole at $\Delta^2 = -m_b^2$, an unphysical value of Δ^2 corresponding to the exchange of a real particle b. At the pole M_{ab} will therefore be the matrix element for the real scattering process $ab \rightarrow ab$. Chew and Low suggested that extrapolating the (measurable) cross-section for $aB \rightarrow Cab$ from the physical region ($\Delta^2 \geqslant 0$) to $\Delta^2 = -m_b^2$ would allow the evaluation of the residue of the pole and hence a determination of the cross-section for the process $ab \rightarrow ab$. Since this process could well be incapable of direct investigation (e.g. $\pi\pi$ scattering) the procedure is clearly

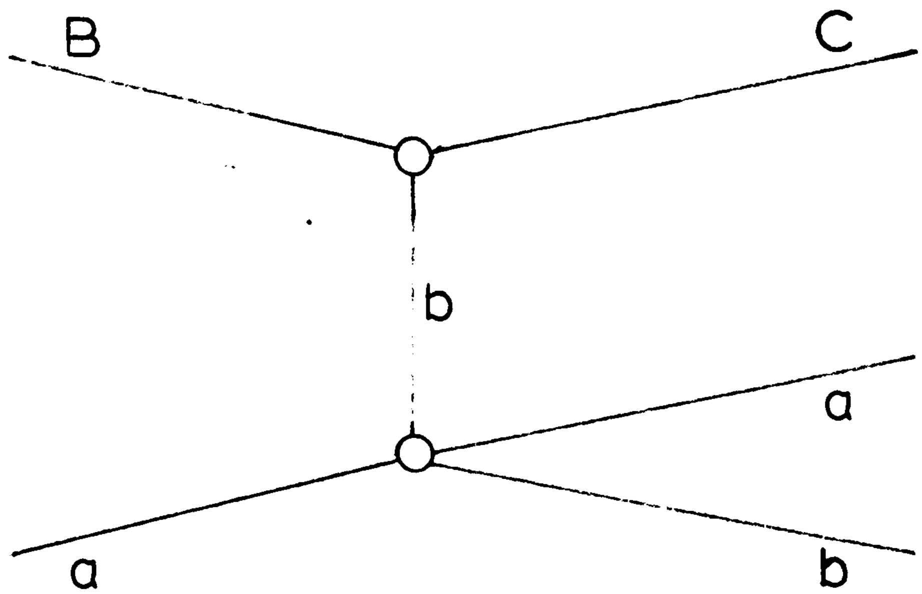

FIGURE 2.2.1

Chew-Low single particle exchange diagram

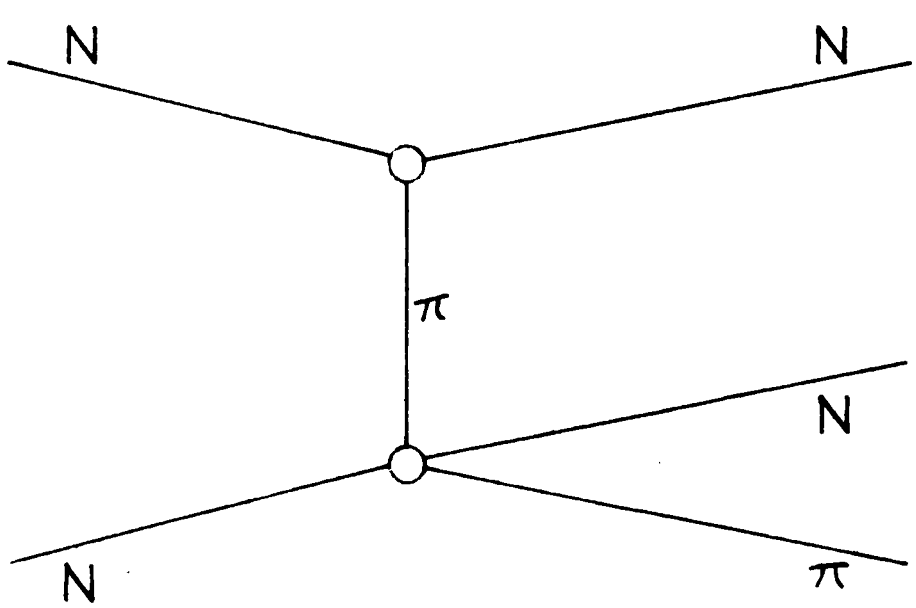

FIGURE 2.2.1a

[illegible]

of considerable value. It does, however, demand that M_{BC} be known as a function of Δ^2. Field theory will give the structure of M_{BC} for all meson-nucleon vertices, and its value at $\Delta^2 = -m_b^2$ as long as the relevant coupling constant is known.

The S-matrix element for the interaction $NN \rightarrow NN\pi$ will have a pole term corresponding to the exchange of a single pion, since both $N\bar{N}$ and $N\bar{N}\pi$ can have the quantum numbers of a single pion (Fig. 2.2.1a). There will, of course, be other pole terms corresponding to the exchange of other particles or composite systems of zero strangeness and baryon number, but these will be further removed from the physical region. Similarly the S-matrix element for the interaction $\pi N \rightarrow N\pi\pi$ will also have a one pion exchange pole term and Goebel (14) first suggested extrapolating data from the physical region to this pole to obtain information on the $\pi\pi$ interaction. The complete Chew-Low expression for the contribution of the one pion exchange diagram is

$$\frac{\partial^2 \sigma}{\partial \Delta^2 \partial \omega^2} \underset{\Delta^2 \to -\mu^2}{\longrightarrow} \frac{1}{2\pi q_i^2} \cdot \frac{G^2}{4\pi} \cdot \frac{\Delta^2}{4m^2} \, \omega \sqrt{\frac{\omega^2}{4} - \mu^2} \cdot \frac{\sigma_{\pi\pi}(\omega)}{(\Delta^2 + \mu^2)^2}$$

$$= \frac{f^2}{2\pi} \, \frac{\omega\sqrt{\omega^2/4 - \mu^2}}{q_i^2} \cdot \left(\frac{\Delta^2/\mu^2}{\Delta^2 + \mu^2}\right)^2 \sigma_{\pi\pi}(\omega) \qquad (2.2.2)$$

where σ = cross-section for $\pi N \rightarrow N\pi\pi$

ω = $\pi\pi$ invariant mass

q_i = lab. momentum of incident pion

f^2 = rationalized pion-nucleon coupling constant

$= 0.08$ for $\pi^0 N$

0.16 for $\pi^{\pm} N$

G = rationalized, renormalised pion-nucleon coupling constant. $G^2/4\pi \simeq 14.5$ and

$f^2 = (G^2/4\pi)(\mu^2/4m^2)$

$\sigma_{\pi\pi}(\omega)$ $=\pi$-π scattering cross-section at $\pi\pi$ centre of mass energy ω.

The extrapolation is performed at constant ω.

Such an extrapolation was performed by Carmony and Van de Walle (15) in the analysis of

$$\pi^{\pm} p \rightarrow p \, \pi^{\pm} \pi^{0}$$

at 1.25 GeV/c and a marked increase in $\sigma_{\pi^+\pi^0}$ at $\omega \sim 750$ MeV was seen: this corresponds to the ρ-meson. The extrapolation was performed by fitting the function (derived from the data)

$$G(\Delta^2,\omega) = (\Delta^2+\mu^2)^2 \frac{2\pi q_1^2}{f^2\omega\sqrt{\frac{\omega^2}{4} - \mu^2}} \frac{\partial^2\sigma}{\partial\Delta^2\,\partial\omega^2} \qquad (2.2.3)$$

with the polynomial expansion

$$G(\Delta^2, \omega^2) \sim A_0 + A_1 (\Delta^2 + \mu^2) + A_2 (\Delta^2 + \mu^2)^2 + \ldots$$

for each region of ω^2 considered. Then $\sigma_{\pi\pi}(\omega) = - A_0$.

If this pole term dominates the physical region, which it could as it is the nearest singularity, this expansion reduces to

$$G (\Delta^2, \omega^2) \simeq A_0 - A_0 (\Delta^2 + \mu^2)/\mu^2 \qquad (2.2.4)$$

giving a fit linear in Δ^2. For the data of Carmony and Van de Walle ($\Delta^2 < +7\mu^2$) a linear fit was more than adequate, supporting the hope that the one pion exchange pole dominates the nearby physical region (small Δ^2).

For the process $pp \rightarrow pp\pi^0$ the expression is

$$\frac{\partial^2\sigma}{\partial\Delta^2\partial\omega} \underset{\Delta^2\rightarrow-\mu^2}{\rightarrow} \frac{f^2 R(\omega)\ \sigma_{\pi^0 p}(\omega)}{2\pi q_i^2} \frac{\Delta^2/\mu^2}{(\Delta^2+\mu^2)^2} \tag{2.2.5}$$

where $R(\omega) = \frac{1}{2}\left\{\omega^4 - 2\omega^2(m^2+\mu^2) + (m^2-\mu^2)^2\right\}^{\frac{1}{2}}$, and the extrapolation procedure is based on

$$\lim_{\Delta^2\rightarrow-\mu^2} \left\{\frac{-2\pi q_i^2}{f^2 R(\omega)} (\Delta^2+\mu^2)^2 \frac{\partial^2\sigma}{\partial\Delta^2\partial\omega^2}\right\} = \sigma_{\pi^0 p}(\omega) \tag{2.2.6}$$

Terms other than the exchange term being isolated will be removed by the $(\Delta^2+\mu^2)^2$ in the numerator above; only those terms with a second order pole at $\Delta^2 = -\mu^2$ will remain.

The extrapolation needs very good statistics over a wide range of Δ^2 and ω^2 if it is to be meaningful. For this reason $\sigma_{\pi^0 p}$ has never been investigated in this fashion. However, the analogous reaction $pp \rightarrow pn\pi^+$ has been used (16) to obtain values of $\sigma_{\pi^+ p}$ in the region of the $N^*(1238)$ resonance in good agreement with direct $\pi^+ p$ scattering experiments.

It should be noted that the N^* is not explicitly considered. However, if the pole term is taken to dominate the nearby physical region then (2.2.5) may be integrated over Δ^2, for small Δ^2, to give

$$\frac{d\sigma}{d\omega^2} \sim \frac{R'(\omega)}{q_i^2} \quad \sigma_{\pi p}(\omega) \tag{2.2.7}$$

where $R'(\omega)$ is slowly varying with ω. This is very similar to the isobar model expression (2.1.2) with the addition that the one pion pole model gives absolute values for the cross-section. Thus the qualitative success of the isobar model is not unexpected.

2.3 The Peripheral Model

Goebel (14) in discussing inelastic pion nucleon collisions had assumed that the one pion exchange (OPE) pole strongly influenced the nearby physical region. Bonsignori and Selleri (17), considering both $\pi N \rightarrow N\pi\pi$ and $NN \rightarrow NN\pi$, argued that the OPE process would be dominant in the physical region, at least for small values of the 4-momentum transfer. Their calculations reproduced the qualitative features of the data available at the time: no quantitative comparisons were made.

Drell (18), Salzman and Salzman (19) and others extended the ideas of OPE to other processes and to higher energies: the model was quite successful. It has since been generalised to include the exchange of particles other than a single pion, leading to the "peripheral" or single particle exchange model. This has been particularly successful in describing the production of resonances in quasi two-body processes, in which the exchanged particle is taken to be a meson, either pseudo-scalar or vector. The principal feature of these processes is a strong forward/backward collimation of the reaction products (or, equivalently, the dominance of interactions involving low momentum transfers). This collimation is much more severe than that given by the field theoretical propagator of the exchanged particle; the simple peripheral model needs modification to explain this.

It is an experimental fact that most multiparticle final states are reached via resonance production. Work on the peripheral model has therefore been confined mainly to quasi two-body processes. Fig. 2.3.1 shows the peripheral diagram for such a process. Four such diagrams, related by the interchange of initial and/or final state nucleons, are possible for the process $NN \to NN\pi$: these diagrams, in which $N^*(1238)$ formation need not be explicitly considered, are shown in Fig. 2.3.2, in which the p's and q's represent four-momenta. In diagram 1 the four-momentum transfer, squared, is

$$\Delta^2 = (q_2 - p_2)^2 \qquad (2.3.1)$$

and other invariants are

$$\omega^2 = -(q + q_1)^2$$

$$t^2 = (q_1 - p_1)^2.$$

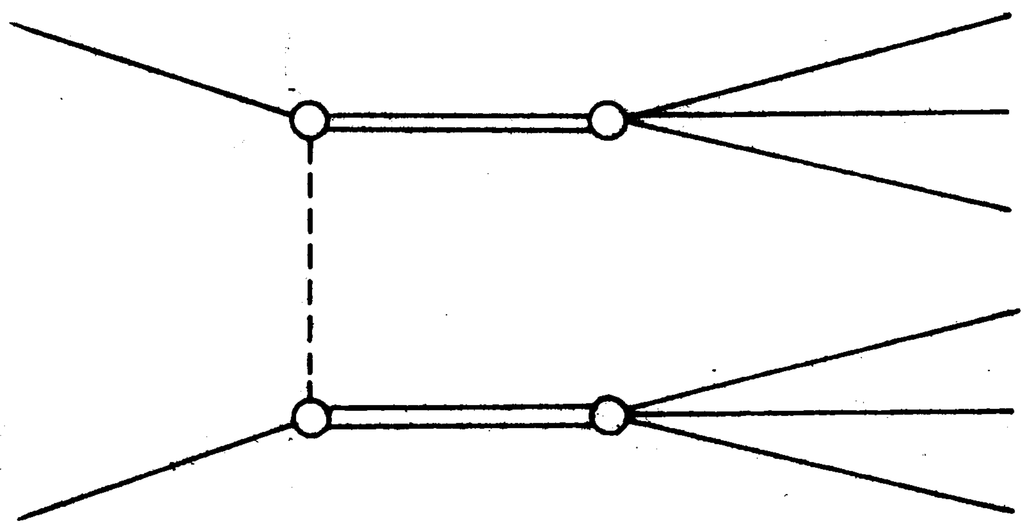

FIGURE 2.3.1

Peripheral diagram for a multiparticle final state produced via a quasi two-body process

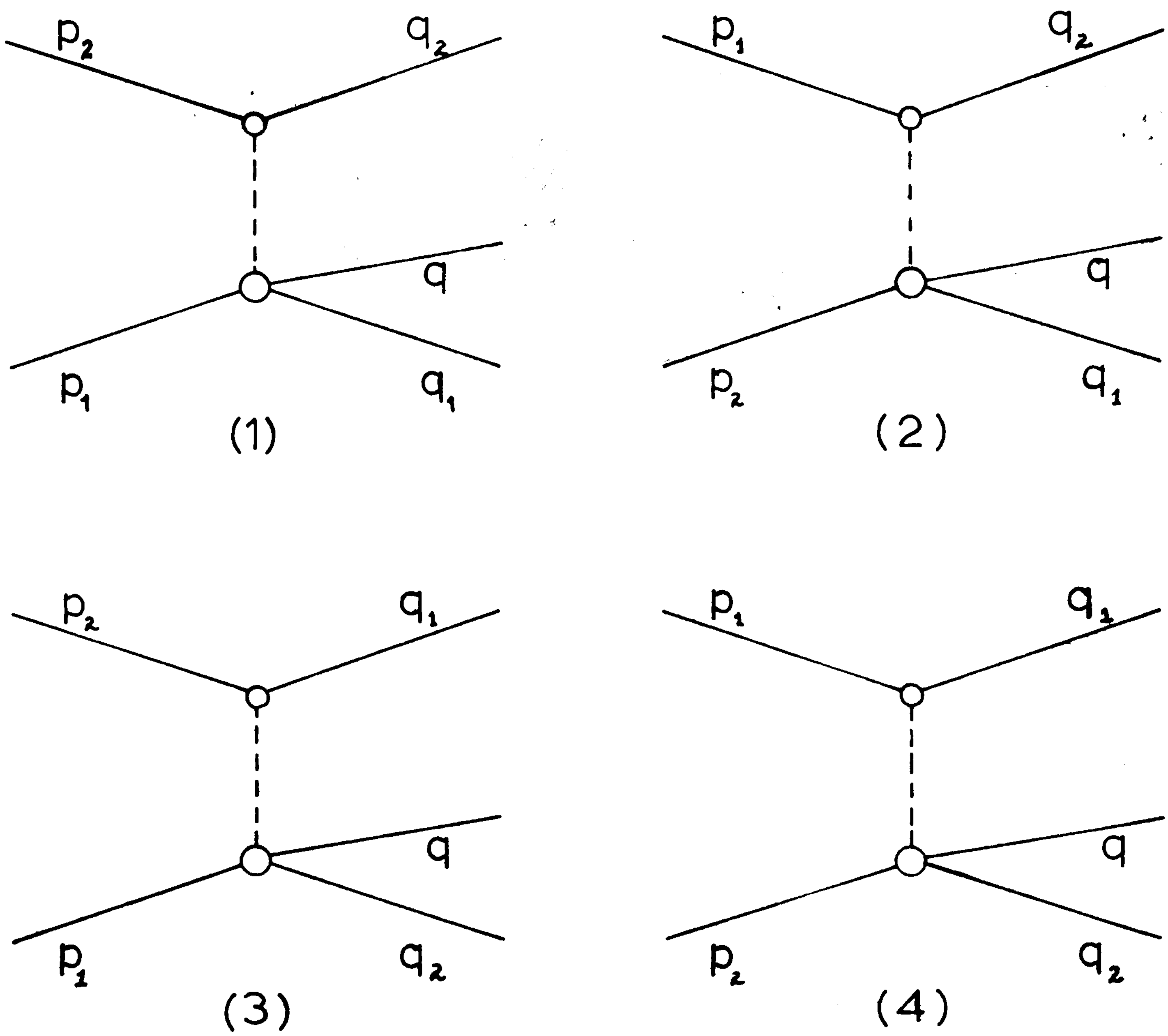

FIGURE 2.3.2

Peripheral diagrams for $NN \to NN\pi$

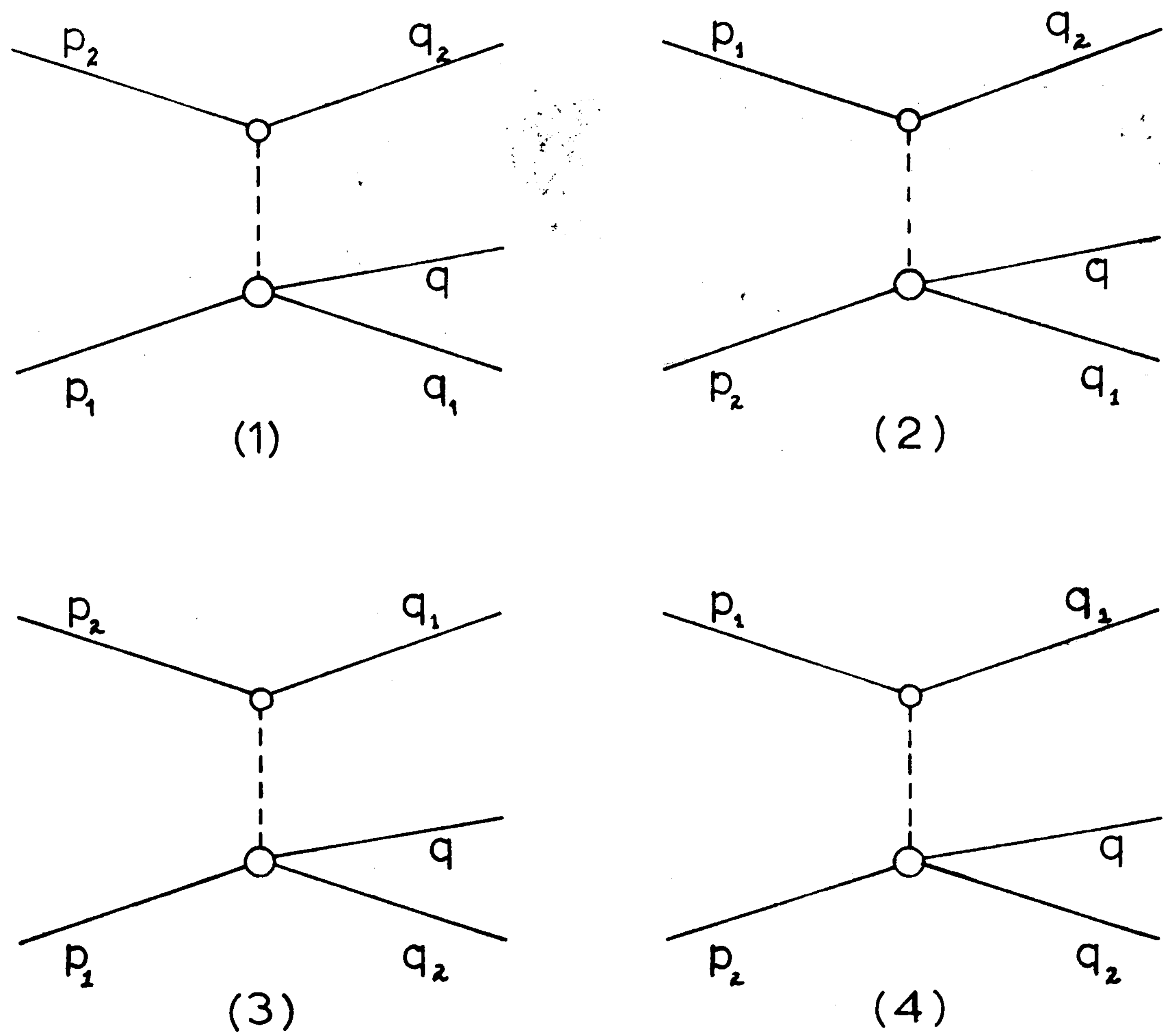

FIGURE 2.3.2

Peripheral diagrams for $NN \rightarrow NN\pi$

Similar invariants can be defined for each of the diagrams; a total of five independent invariants is needed to describe the process.

The S-matrix element for the process can be written (26)

$$S_{fi} = - i\frac{1}{(2\pi)^{7/2}} \left\{ \frac{m^4}{2q_0 q_{10} q_{20} p_{10} p_{20}} \right\}^{\frac{1}{2}} \delta^4(P_f - P_i) M_{fi} \quad (2.3.2)$$

with $P_f = q + q_1 + q_2$ and $P_i = p_1 + p_2$.

$$M_{fi} = M_1 - M_2 - M_3 + M_4, \quad (2.3.3)$$

M_i being the matrix element corresponding to the i^{th} diagram and the + or - signs being due to the identity of initial and final nucleons.

The M_i are related to M_1 by the exchanges $p_1 \rightarrow p_2$ $(M_1 \rightarrow M_2)$, $q_1 \rightarrow q_2$ $(M_1 \rightarrow M_3)$ and $p_1 \rightarrow p_2$, $q_1 \rightarrow q_2$ $(M_1 \rightarrow M_4)$. Suppressing spin variables,

$$M_1 = \bar{u}(q_2)\, G\gamma_5\, u(p_2)\, K(\Delta^2)\, \frac{K'(\Delta^2)}{\Delta^2 + \mu^2}$$

$$\bar{u}(q_1) \left\{ -A(\omega_1^2\, t_1^2\, \Delta^2) + i(\gamma.q)B(\omega^2, t^2, \Delta^2) \right\} u(p_1) \quad (2.3$$

The component parts of this expression are

a) the pseudo-scalar pion nucleon vertex matrix element, with G the pion nucleon coupling constant $(G^2/4\pi = 14.5)$ and $K(\Delta^2)$ the vertex structure form factor,

b) the first order perturbational pion propagator $(\Delta^2 + \mu^2)^{-1}$ and its correction function $K'(\Delta^2)$,

c) the off-shell pion-nucleon scattering matrix element (21) (through which the $N^*(1238)$ resonance would appear).

The general differential cross-section is

$$d\sigma = \frac{1}{(2\pi)^5} \cdot \frac{1}{F} \cdot \frac{m^4}{2} \sum |M_{fi}|^2 \ \delta^4(P_f - P_i) \ \frac{d^3q \ d^3q_1 \ d^3q_2}{q_0 \ q_{10} \ q_{20}} \qquad (2.3.5)$$

where $\sum$ indicates a sum over final, and an average over initial, spin states. F is the invariant flux factor. Since G is known the predictions of (2.3.5) are absolute in magnitude.

In order to extract a particular cross-section from (2.3.5) $|M_{fi}|^2$ must be evaluated; there are two difficulties:

a) the (unmeasurable) off-shell pion-nucleon scattering matrix element has to be evaluated,

b) there are interference terms of the form $2 \, \mathrm{Re} \sum_{i,j} M_i M_j^*$ whose values depend strongly on the amplitudes appearing in the off-shell scattering.

The former point was considered by Iizuka and Klein (22) and Ferrari and Selleri (23) who used dispersion relations in the various amplitudes to extend them into the non-physical region. The normal approximation, however, is to assume that the off-shell amplitude is given by an empirical Δ^2-dependent function times the on-shell amplitude, but to take the full Δ^2 dependence of the scattering angle into account. The on-shell scattering differential cross-section can be written

$$\frac{d\sigma}{d\Omega}(\omega^2, \cos\theta, \Delta^2 = -\mu^2) = \frac{m^2}{4\omega^2} \cdot \frac{1}{(2\pi)^2} \cdot \frac{q}{k} \left| M(\omega^2, \cos\theta) \right|^2 \qquad (2.3.6)$$

where $M(\omega^2, \cos\theta)$ is the $\pi N \rightarrow N\pi$ matrix element, θ = centre of mass scattering angle and $k(q)$ = centre of mass three-momentum of the incident (final) pion. In a physical process $k = q$.

The standard partial wave expansion is

$$\frac{d\sigma}{d\Omega} = \frac{q}{k} \left| \sum_{\ell=0} \left\{ (\ell+1) f_{\ell+}(\omega) + \ell f_{\ell-}(\omega) \right\} P_\ell(\cos\theta) \right|^2 +$$

$$\frac{q}{k} \left| \sum_{\ell=1} \left\{ f_{\ell+}(\omega) - f_{\ell-}(\omega) \right\} \sin\theta \, P'_\ell(\cos\theta) \right|^2 \qquad (2.3.7)$$

where $\ell_{\pm}$ refer to total angular momentum $\ell \pm \frac{1}{2}$ and $f_{\ell\pm}$ are the partial wave amplitudes, related to the phase-shifts $\delta_{\ell,j}$ by

$$f_{\ell\pm} = e^{i\delta_{ij}} \sin \delta_{\ell,j} / q \qquad (2.3.8)$$

If $\Delta^2 \neq -\mu^2$ the f's depend on Δ^2, as do k and $\cos\theta$. The simplest approximation consists of keeping the full Δ^2 dependence of k and $\cos\theta$ but replacing $f_{\ell\pm}(\omega, \Delta^2)$ by $\psi(\Delta^2) f_{\ell\pm}(\;)$ where $\psi(\Delta^2)$ is some function, evaluated explicitly by Ferrari and Selleri (23) for the $p_{3/2}$ state i.e. for f_{1+}. This is useful since in making calculations often only f_{1+} is retained. Putting $\psi(\Delta^2) = 1$ results in the "pole approximation". This is not the same as replacing $M(\omega^2, \cos\theta, \Delta^2)$ by $M(\omega^2, \cos^2\theta, -\mu^2)$, which is equivalent to extending the Chew-Low expression (2.2.5) to the physical region. However, as $\Delta^2 \to -\mu^2$ the OPE expression reduces to the Chew-Low expression (since $K(-\mu^2) = K'(-\mu^2) = 1$), and the extrapolation remains valid.

Da Prato (24) considered the interference effects between OPE diagrams for the reactions $pp \to pn\pi^+$ and $pp \to pp\pi^0$, evaluating all diagrams in the pole approximation. He concluded that only interference between diagrams 1 and 2, and 3 and 4 was significant, while interferences between 1 and 4, 2 and 3 were identically zero. In the region of $N^*(1238)$ formation $pp \to pn\pi^+$ will have diagrams 3 and 4, in which the pion and neutron emerge from the same vertex, suppressed relative to 1 and 2 by an isotopic spin factor of 1/9 so that, essentially, only diagrams 1 and 2 need be considered. This is the basis of the expression for $d\sigma/dT$ (Δ^2=2mT) (evaluated without form factors) given by Selleri (20) and compared with data at 0.97 GeV. (Barnes et al. (16)). The agreement is good at low Δ^2, poor at high ($\Delta^2 \gtrsim 10\mu^2$).

Later calculations by Ferrari and Selleri (25,26) included the form factors: they used a cut-off function

$$\phi(\Delta^2) = K^2(\Delta^2)\, K'(\Delta^2)\, \psi(\Delta^2) \qquad (2.3.9)$$

and found an empirical fit to data at 0.97, 2.02 and 2.85 GeV (8, 9, 10), taking into account all possible diagrams, with

$$\phi(\Delta^2) = \frac{1}{1 + \frac{\Delta^2 + \mu^2}{\alpha\mu^2}} \qquad (2.3.10)$$

and α in the range 60 - 90.

More elaborate calculations have been made (26, 27) which include the effects of higher pion-nucleon resonances and in which different forms of $\phi(\Delta^2)$ have been used. Ferrari and Selleri used, for the $N^*(1238)$ production region where they assumed only f_{1+} to be significant

$$K^2(\Delta^2)\, K'(\Delta^2) = \frac{0.72}{1 + \dfrac{\Delta^2+\mu^2}{4.73\mu^2}} + 0.28 \qquad (2.3.11)$$

with $\psi(\Delta^2)$ as determined in their earlier work (23, 25).

The reaction $\pi N \rightarrow N\rho$ can be considered in the same way (26, 27) and Amaldi and Selleri (28) fitted data with (2.3.11). However, Goldhaber et al. (29), considering $KN \rightarrow K^* N^*$, used $(0.132-\mu^2)/(0.132+\Delta^2)$ $\left[\mu^2, \Delta^2 \text{ in } (\text{GeV/c})^2\right]$ so that although empirical fits were good there was no unanimous choice of cut-off function.

Objections were raised to the use of these ad hoc functions, the principal objections being that they involved unphysically small characteristic masses with no real relationship to the nucleon electromagnetic form factors, and that they varied too strongly with Δ^2 to satisfy the dispersion relations they should obey (44, 45). So in spite of the model's success in many different interactions (34) its physical justification was uncertain.

This was even more true of interactions involving vector meson exchange (35), where the form factors required were so drastic as to mask the effect of the exchange propagator.

As a result, it is impossible to deduce the nature of the exchanged particle from the distribution in momentum transfer, $d\sigma/d\Delta^2$.

An approach to this problem was suggested by Treiman and Yang (30) as a test of the OPE model. Since the particle spin states at the two vertices in the peripheral diagram are linked only by the spin state of the exchanged particle a process involving pion exchange (zero spin) should result in no angular correlations between the products at the two vertices. This conclusion is valid independently of any assumed vertex structure. For the common final state of resonance plus stable particle the Treiman-Yang criterion reduces to the requirement that the production cross-section should not depend on the angle between the decay plane of the resonance and the reaction production plane, as seen in the rest frame of the resonance, or, equivalently, that the rest frame decay angular distribution of the resonance should show no azimuthal dependence about the direction of the exchanged particle. (This equivalence was proved by Jackson (31)).

ρ-exchange, with the ρ interaction analogous to photon excitation via M1 radiation, was considered by Stodolsky and Sakurai (32) and by Jouvet et al. (33) and another isotropy requirement formulated.

Interactions (34) expected to go dominantly via OPE gave decay distributions in agreement with OPE predictions (for example, ρ -decay must be $\propto \cos^2\theta$ since only the $j_z=0$ state of the ρ can be populated in $\pi N \rightarrow N\rho$, and in $NN \rightarrow N^*N$ the N^* decay must be $\propto 1 + 3\cos^2\theta$ since only the $|j, j_z\rangle = |3/2, \pm 1/2\rangle$ states of the N^* can be populated). The Treiman-Yang criterion was also satisfied. Interactions in which pion exchange was forbidden (35) gave distributions in fair agreement with the predictions of Stodolsky and Sakurai who would, for example, have N^* decay $\propto 5 - 3\cos^2\theta$ if formed via ρ-exchange.

The Treiman-Yang (or Stodolsky-Sakurai) distributions are easily calculated when there is only one diagram contributing, as in $\pi N \rightarrow N\rho$. The four diagrams possible in nucleon-nucleon collisions are all kinematically different as far as the resonance direction is concerned, and all interfere coherently, complicating the problem considerably. This has been considered by Ferrari (36). A full solution required the evaluation of each diagram plus interference terms, which strongly affect angular distributions. The theory is not sufficiently refined for these distributions to be any more than a guide, so the Treiman-Yang test is indecisive when applied to $NN \rightarrow NN\pi$ and any admixture of vector exchange (expected at energies $\gtrsim$ 2 GeV) would be difficult to establish.

Jackson and Gottfried (38) gave a unified treatment, based on the density matrix formalism, of decay angular distributions. The values of the various density matrix elements of the resonance are related to the spins of the exchanged particle and of the resonance, and immediate comparison with experimental data is possible. Such comparisons have proved powerful tools for the interpretation of data and have shown deviations from the expectation of pure pseudo-scalar or vector exchanges (44) although their qualitative predictions were well satisfied.

2.4 Absorption Effects in the Peripheral Model

Ball and Frazer (39) had pointed out that the lowest OPE partial wave amplitudes violated the unitarity limit of $\pi \lambda\!\!\!^{-2}(2j+1)$ and, although this was disputed by Amaldi and Selleri (28, 40) several authors (41, 42, 43, 44) considered the effects of absorption in both the initial and final channels as a way of reducing these partial amplitudes. The absorptive model modifies the peripheral diagram to look schematically like Fig. 2.4.1, the absorption being represented by a 'blob'.

This model has been developed in a manner analogous to the distorted wave Born approximation of low energy physics by Durand and Chiu (45) and by Jackson and others (46) to the point where good fits to experimental data have been obtained, both for production distributions and decay angular distributions including, gratifyingly, deviations in the latter from simple peripheral model predictions. With certain simplifying assumptions (see below) the j^{th}

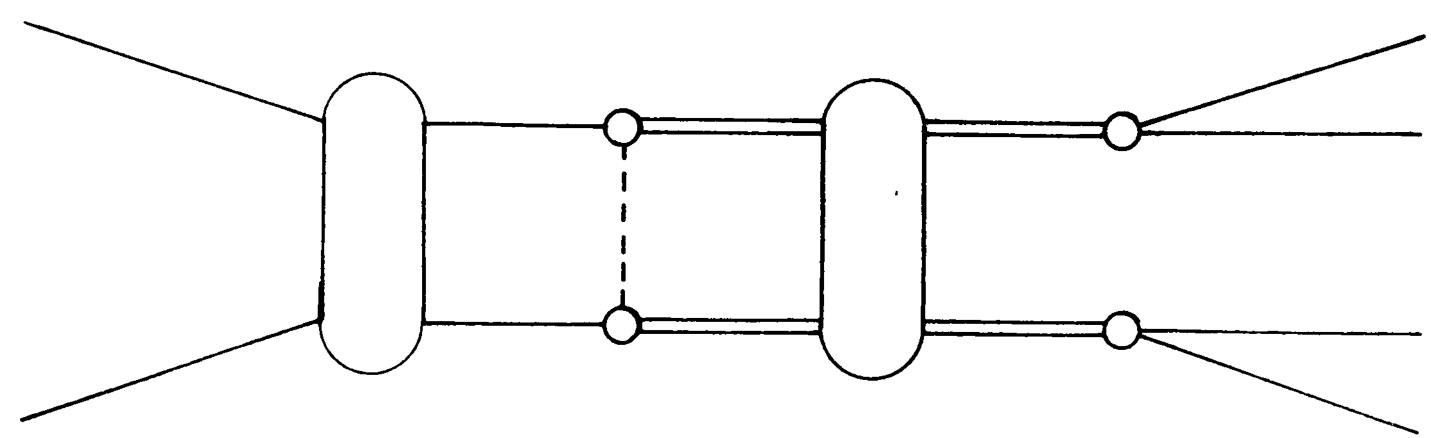

FIGURE 2.4.1

Peripheral diagram with absorption in initial and final channels amplitude can be written

$$T^j = e^{i\delta_f^j} \; T_p^j \; e^{i\delta_i^j} \qquad (2.4.1)$$

where T_p^j is the peripheral amplitude and δ_i^j, δ_f^j are the phase shifts for scattering in the initial and final states; the δ_i are obtainable from elastic scattering experiments, the δ_f are usually not obtainable and are left in parametric form to be determined by a best fit to data. The model, which does not use form factors in calculating T_p^j, is most successful for pion exchange: Jackson suggested that a mild form factor could be reasonable for ρ exchange, but neither experiment nor theory is sufficiently refined to confirm this. With absorptive effects taken into account the Chew-Low extrapolation scheme can no longer give the correct answer since the $e^{i\delta}$ factors remain in the residue and must be taken into account.

Absorptive calculations have not been made for $NN \rightarrow N^*N \rightarrow NN\pi$ and, furthermore, the basic assumptions of Jackson's approach are of doubtful validity in this case. These assumptions are (46) that

(i) the absorptive interactions are of much larger range than the peripheral interaction,

(ii) the peripheral process, while contributing to the initial and final state absorptive processes, is not a significant part of either,

(iii) both initial and final state elastic scattering amplitudes are purely imaginary (i.e. the elastic scattering is purely diffractive or "black sphere" in nature and the real parts of the phase shifts are zero),

(iv) the absorption can be described by a complex potential.

For $NN \rightarrow N^*N$ the only significant competing channel at incident energies $\lesssim 2$ GeV (8, 9) is elastic or charge exchange scattering: the tacit assumption in (ii) above of many competing inelastic channels is not valid. Measurements of the pp elastic scattering amplitude (47) show that it is about 30% real at high energies, so (iii) is doubtful, while (iv) is a rather gross assumption to make about high energy collisions.

Development of the absorptive model continues (47, 48) with approaches incorporating unitarity ab initio but the basic conclusions are not much altered. That is, that the four-momentum transfer poles in the S-matrix element, corresponding to the exchange of one particle, strongly affect the nearby physical region to the extent of dominating inelastic matrix elements (but approaches to, for example, pion-nucleon charge exchange via ρ-exchange have been less successful), while interactions in the initial and final channels, although significant, do not mask the characteristic effects of such exchange processes.

The Interaction $pp \rightarrow pp\pi^o$

This thesis is concerned with the reaction $pp \rightarrow pp\pi^o$
.t is relevant at this point to relate the previous
ssion to this interaction.

The interaction $pp \rightarrow pp\pi^o$ has been investigated in
bubble chamber experiments, at 0.97, 2.02 and 2.85
8, 9, 10). The observed processes were dominated by
ic scattering and $pp \rightarrow pn\pi^+$, and statistics were poor.
er, the reaction was clearly peripheral with processes
ving low momentum transfer dominant. Only at 970 MeV
the experimental distributions for $d\sigma/dT$ compared with
errari-Selleri OPE predictions, with and without form
rs. The dominance of $N^{*+}(1238) \rightarrow p\pi^o$ was not marked,
-space being adequate at 970 MeV, but both $N^*(1238)$
$^*(1520)$ (at higher energies) appeared, so the predictions
e isobar model were satisfied. The poor statistics
a Chew-Low extrapolation impossible.

ngular distributions, including the Treiman-Yang
ibution, are of doubtful significance (as remarked
er) and were not given for the $pp\pi^o$ final state.
were given for $pn\pi^+$ and were in fair agreement with
ified pion exchange calculations (36). It would,
er, be impossible to rule out vector exchanges on
evidence.

Data from all three experiments were used by Ferrari
elleri (26) when finding the best cut-off factor:

2.5 The Interaction $pp \rightarrow pp\pi^o$

This thesis is concerned with the reaction $pp \rightarrow pp\pi^o$ and it is relevant at this point to relate the previous discussion to this interaction.

The interaction $pp \rightarrow pp\pi^o$ has been investigated in three bubble chamber experiments, at 0.97, 2.02 and 2.85 GeV (8, 9, 10). The observed processes were dominated by elastic scattering and $pp \rightarrow pn\pi^+$, and statistics were poor. However, the reaction was clearly peripheral with processes involving low momentum transfer dominant. Only at 970 MeV were the experimental distributions for $d\sigma/dT$ compared with the Ferrari-Selleri OPE predictions, with and without form factors. The dominance of $N^{*+}(1238) \rightarrow p\pi^o$ was not marked, phase-space being adequate at 970 MeV, but both $N^*(1238)$ and $N^*(1520)$ (at higher energies) appeared, so the predictions of the isobar model were satisfied. The poor statistics made a Chew-Low extrapolation impossible.

Angular distributions, including the Treiman-Yang distribution, are of doubtful significance (as remarked earlier) and were not given for the $pp\pi^o$ final state. They were given for $pn\pi^+$ and were in fair agreement with simplified pion exchange calculations (36). It would, however, be impossible to rule out vector exchanges on this evidence.

Data from all three experiments were used by Ferrari and Selleri (26) when finding the best cut-off factor:

with (2.3.10) they fitted the data at all three energies.

An experiment to investigate $pp \rightarrow pp\pi^o$ in the region where one of the outgoing protons plus the pion would be initially in the $N^*(1238)$ state could enable

(a) values of $d^2\sigma/d\omega^2 d\Delta^2$ to be measured and compared with the OPE predictions of Ferrari and Selleri so that any variation of the cut-off factor with ω^2 could be seen,

(b) the experimental peak in the $p\pi^o$ mass distribution to be found, compared with that expected (31) for N^{*+} production and the N^{*+} intrinsic mass and width found (production experiments (50) showed the N^{*++} peak to be at ~ 1215±5 MeV),

(c) a Chew-Low extrapolation to the OPE pole at $\Delta^2=-\mu^2$ to be made, from which π^op elastic scattering cross-sections could be deduced. Deviations from cross-sections calculated from pion-nucleon phase-shifts could show the influence of absorptive effects.

Selecting events with π^op mass around 1238 MeV greatly simplifies the OPE calculations since to good approximation only the $p_{3/2}$ amplitude need be retained in the partial wave expansion (2.3.7). Even so, the angular distributions so calculated for the π^op decay must be treated with caution since it is known (4) that the I=1/2, J=1/2, 3/2 amplitudes are not negligible, even at the resonance, and will markedly affect the angular distributions if not total elastic cross-sections.

References

(1) See B. Rossi "High Energy Physics" (Prentice Hall, New York, 1952) for a review, and references

(2) E. Fermi Prog. Theor. Phys. 5, 570 (1950), Phys. Rev. 92, 452, (1953), Phys. Rev. 93, 1435 (1954)

(3) S.J. Lindenbaum and L.C.L. Yuan Phys.Rev. 93, 917 (1954) Phys. Rev. 93, 1431 (1954), Phys. Rev. 103, 404 (1956)

(4) W.O. Lock, "High Energy Physics" (Methuen, London, 1960) Chapter 4.
G. Källen, "Elementary Particle Physics" (Addison-Wesley, Reading, Mass. 1964) Chapter 4.

(5) J.S. Kovacs Phys. Rev. 101, 397 (1956)

(6) D.C. Peaslee Phys. Rev. 94, 1085 (1954), Phys. Rev. 95, 1580 (1954)

(7) S.J. Lindenbaum and R.M. Sternheimer Phys. Rev. 105, 1874 (1957), Phys. Rev. 109, 1723 (1958)

(8) D.V. Bugg, A.J. Oxley, J.A. Zoll, J.G. Rushbrooke, V.E. Barnes, J.B. Kinson, W.P. Dodd, G.A. Doran, L. Riddiford. Phys. Rev. 133, B1017 (1964)

(9) W.J. Fickinger, E. Pickup, D.K. Robinson, E.O. Salant Phys. Rev. 125, 2082 (1962)

(10) G.A. Smith, H. Courant, E.C. Fowler, H. Kraybill, J. Sandweiss, H. Taft. Phys. Rev. 123, 2160 (1961)

(11) G. Cocconi, A.N. Diddens, E. Lillethun, A.M. Wetherell Phys. Rev. Letters 6, 231 (1961)
G. Cocconi, A.N. Diddens, E. Lillethun, G. Manning, A.E. Taylor, T.G. Walker, A.M. Wetherell Phys. Rev. Letters 7, 450 (1961)
M.A.R. Kemp, G.B. Chadwick, G.B. Collins, P.J. Duke, T. Fujii, H.C. Hein, F. Turkot Phys. Rev. 128, 1923 (1962)
G. Cocconi, E. Lillethun, J.P. Scanlon, C.A. Stahlbrandt, C.C. Ting, J. Walters, A.M. Wetherell Physics Letters 8, 134 (1964)
C.M. Ankenbrandt, A.R. Clyde, B. Cork, D. Keefe, L.T. Kerth, W.M. Layson, W.A. Wenzel Nuovo Cimento 35, 1052 (1965)

(12) S.J. Lindenbaum and R.M. Sternheimer Phys. Rev. Letters 5, 24 (1960)

(13) G.F. Chew and F.E. Low Phys. Rev. 113, 1640 (1959)

(14) C. Goebel Phys. Rev. Letters 1, 337 (1958)

(15) D.D. Carmony and R.T. Van de Walle
Phys. Rev. 127, 959 (1962)
See also J.A. Anderson, V.X. Bang, P.G. Burke, N. Schmitz
Phys. Rev. Letters 6, 365 (1961)
Rev. Mod. Phys. 33, 431 (1961)

(16) G.A. Smith, H. Courant, E. Fowler, H. Kraybill,
J. Sandweiss, H. Taft Phys. Rev. Letters 5, 571 (1960)
V.E. Barnes, D.V. Bugg, W.P. Dodd, J.B. Kinson,
L. Riddiford Phys. Rev. Letters 7, 288 (1961)

(17) F. Bonsignori and F. Selleri
Nuovo Cimento 15, 465 (1960)

(18) S.D. Drell Phys. Rev. Letters 5, 278 and 342 (1960)
Rev. Mod. Phys. 33, 458 (1961)

(19) F. Salzman and G. Salzman Phys. Rev. 120, 599 (1960)
Phys. Rev. Letters 5, 377 (1960)

(20) F. Selleri Phys. Rev. Letters 6, 64 (1961):
his expression for $d\sigma/dT$ should be multiplied by 2.

(21) G.F. Chew, M.L. Goldberger, F.E. Low, Y. Nambu
Phys. Rev. 106, 1377 (1957)

(22) J. Iizuka and A. Klein Prog.Theor. Phys. 25, 1017 (1961),
Phys. Rev. 123, 669 (1961)

(23) E. Ferrari and F. Selleri Nuovo Cimento 21, 1028 (1961),
F. Selleri Nuovo Cimento (to be published)
See also Jackson (31) appendix B

(24) G. Da Prato Nuovo Cimento 22, 123 (1961)

(25) E. Ferrari and F. Selleri Phys. Rev. Letters 7, 387 (1962)

(26) E. Ferrari and F. Selleri
Suppl. Nuovo Cimento 24, 453 (1962)

(27) E. Ferrari and F. Selleri Nuovo Cimento 27, 1450 (1963)

(28) U. Amaldi and F. Selleri Nuovo Cimento 31, 360 (1964)

(29) G. Goldhaber, W. Chinowsky, S. Goldhaber, W. Lee,
T. O'Halloran Physics Letters 6, 62 (1963)

(30) S.B. Treiman and C.N. Yang Phys. Rev. Letters 8, 140 (1962)

(31) J.D. Jackson Nuovo Cimento 34, 1644 (1964)

(32) L. Stodolsky and J.J. Sakurai
Phys. Rev. Letters 11, 90 (1963)
See also L. Stodolsky Phys. Rev. 134, B1099;
Y. Li and M.B. Martin Phys. Rev. 135, B561 (1964)

(33) B. Jouvet, J.M. Abillon and G. Bordes
Physics Letters 6, 273 (1963)

(34) V. Alles-Borelli, S. Bergia, E. Perez Ferreira, P. Waloschek Nuovo Cimento 14, 211 (1959)
J.G. Rushbrooke and D. Radojicic
Phys. Rev. Letters 5, 567 (1960)
E. Pickup, F. Ayer, E.O. Salant
Phys. Rev. Letters 5, 161 (1960)
I. Derado Nuovo Cimento 15, 853 (1960)
A.R. Erwin, R. March, W.D. Walker, E. West
Phys. Rev. Letters 6, 628 (1961)
H. Foelsche, E.C. Fowler, H.L. Kraybill, J.R. Sandford, D. Stonehill. Proc. 1962 Int. Conf. on High Energy Physics, Geneva, 4-11 July 1962, p. 36.
G. Goldhaber, W. Chinowsky, S. Goldhaber, W. Lee, T. O'Halloran. Phys. Rev. Letters 9, 330 (1962), Physics Letters 6, 62 (1963)
C. Alff, D. Berley, D. Colley, N. Gelfand, U. Nauenberg, D. Miller, J. Schultz, J. Steinberger, T.H. Tan, H. Brugger, P. Kramer, R. Plano
Phys. Rev. Letters 9, 322 (1962)
R. Kraemer, L. Madansky, I. Miller, A. Pevsner, C. Richardson, R. Singh, R. Zdanis
Proc. Athens Topical Conference on Recently Discovered Resonances, April 1963, p. 130
R.L. Lander, W. Mehlhop, N. Xuong. P.M. Yager
Proc. Athens Conf. p. 294
Saclay-Orsay-Bari-Bologna Collaboration Proc. Sienna Int. Conf. on Elementary Particles, October 1963, Vol. I p. 239
Aachen-Berlin-Birmingham-Bonn-Hamburg-London(I.C.)-München Collaboration Nuovo Cimento 34, 495 (1964)
Nuovo Cimento 31, 729 (1964), 35, 659 (1965)
Aachen-Berlin-CERN Collaboration
Physics Letters 12, 356 (1964)

(35) B. Kehoe Phys. Rev. Letters 11, 93 (1963)
G.B. Chadwick, D.J. Crennell, W.T. Davies, M. Derrick, J.H. Mulvey, P.B. Jones, D. Radojicic, C.A. Wilkinson, A. Bettini, M. Cresti, S. Limentani, L. Peruzzo, R. Santangelo Physics Letters 6, 309 (1963)
S. Goldhaber Proc. Athens Topical Conf. on Recently Discovered Resonances, April 1963, p. 80
M. Ferro-Luzzi, R. George, Y. Goldschmidt-Clermont, V.P. Henri, B. Jongegans, D. Leith, G. Lynch, F. Muller, J.M. Perreau Nuovo Cimento 36, 1101 (1965), Physics Letters 9, 359 (1964)
Saclay-Orsay-Bari-Bologna Collaboration Proc. Sienna Conference on Elementary Particles, October 1963, Vol. I, p. 239
A. Daudin, M.A. Jabiol, C. Kochowski, C. Lewin, F. Selleri, S. Mongelli, A. Romano, P. Waloschek Physics Letters 7, 125 (1963)
V. Barger and E. McCliment Physics Letters 9, 91 (1964)
Aachen-Berlin-Birmingham-Bonn-Hamburg-London(I.C.)-München Collaboration Physics Letters 10, 229 (1964), Nuovo Cimento 34, 495 (1964) 35, 659 (1965)
M. Abolins, D.D. Carmony, D.N. Hoa, R.L. Lander, C. Rindfleisch, N.H. Xuong Phys. Rev. 136, 3195 (1964)
Saclay-Orsay-Bari-Bologna Collaboration Phys. Letters 13, 341 (1964)
H.O. Cohn, W.M. Bugg, G.T. Condo Phys. Letters 15, 344 (1965)

(36) E. Ferrari Phys. Letters 2, 66 (1962)

(37) J.D. Jackson and H. Pilkuhn Nuovo Cimento 33, 906 (1964)

(38) K. Gottfried and J.D. Jackson Phys. Letters 8, 144 (1964), Nuovo Cimento 33, 309 (1964)

(39) J. Ball and W. Frazer Phys. Rev. Letters 7, 204 (1961)

(40) F. Selleri Physics Letters (to be published)

(41) N. Sopkovitch Nuovo Cimento 26, 186 (1962)

(42) M. Baker and R. Blankenbecler Phys. Rev. 128, 415 (1962)

(43) A. Dar, M. Kugler, Y. Dothan, S. Nussinov Phys. Rev. Letters 12, 82 (1964)
A. Dar and W. Tobocman Phys. Rev. Letters 12, 511 (1964)
A. Dar Phys. Rev. Letters 13, 91 (1964)

(44) M.H. Ross and G.L. Shaw Phys. Rev. Letters 12, 627 (1964)

(45) L. Durand and Y.T. Chiu Phys. Rev. Letters 12, 399 (1964),
Phys. Rev. 137, B1530 (1965)

(46) K. Gottfried and J.D. Jackson
Nuovo Cimento 34, 735 (1964)
J.D. Jackson Rev. Mod. Phys. (to be published)
J.D. Jackson, T.D. Donohue, K. Gottfried, R. Keyser,
B.E.Y. Svensson Phys. Rev. (to be published)

(47) J.D. Dowell, R.J. Homer, Q.H. Khan, W.K. McFarlane,
J.S.C. McKee, A.W. O'Dell Phys. Letters 12, 252 (1964)
L. Kirillova, L. Khristov, V. Nikitin, M. Shafranova,
L. Strunov, V. Sviridov, Z. Korbel, L. Rob, P. Markov,
Kh. Tchernev, T. Todorov, A. Zlateva
Phys. Letters 13, 93 (1964)
A.E. Taylor, A. Ashmore, W.S. Chapman, D.F. Falla, W.H. Range,
D.B. Scott, A. Astbury, F. Capocci, T.G. Walker
Phys. Letters 14, 54 (1965)

(48) K. Dietz and H. Pilkuhn Nuovo Cimento 37, 1561 (1965),
H.D.D. Watson Physics Letters 17, 72 (1965)

(49) J.S. Ball and W. Frazer Phys. Rev. Letters 14, 746 (1965)

(50) M. Ferro-Luzzi, R. George, Y. Goldschmidt-Clermont,
V.P. Henri, B. Jongejans, D. Leith, G. Lynch, F. Muller,
J.M. Perreau Nuovo Cimento 36, 1101 (1965)
E. Boldt, J. Duboc, N.H. Duong, P. Eberhard, R. George
V.P. Henri, F. Levy, J. Poyen, M. Pripstein, J. Cussard,
A. Trau Phys. Rev. 133, B220 (1964)

Chapter 3. Design Considerations

The experiment to be described was designed to investigate the interaction

$$p + p \rightarrow p + p + \pi^0$$

at an incident proton energy (governed by the Birmingham proton synchrotron) of 1 GeV. The target matter was liquid hydrogen, for which the loss in density compared with, say, polythene is adequately compensated by the lack of correction factors (apart from those due to interactions in the container vessel) to be applied.

The experiment was intended to measure $\frac{d^2\sigma}{d\omega^2 d\Delta^2}$ (notation as previous chapter) for a small range of ω (1238±15 MeV), and for Δ^2 from about 5 to 20 μ^2 (μ = pion mass). In the design dominance of OPE diagrams 1 and 2 was assumed (see Fig. 2.3.2) so that a measurement of the direction and energy of the recoil proton fully defined ω and Δ^2. To complete identification of the event the other (isobar) proton had to be detected within its kinematically allowed volume.

The kinematics for the interaction

$$pp \rightarrow pN^{*+}$$

are summarised, for the region of interest, in Figs. 3.1 and 3.2. Clearly, the scintillation counter spark chamber

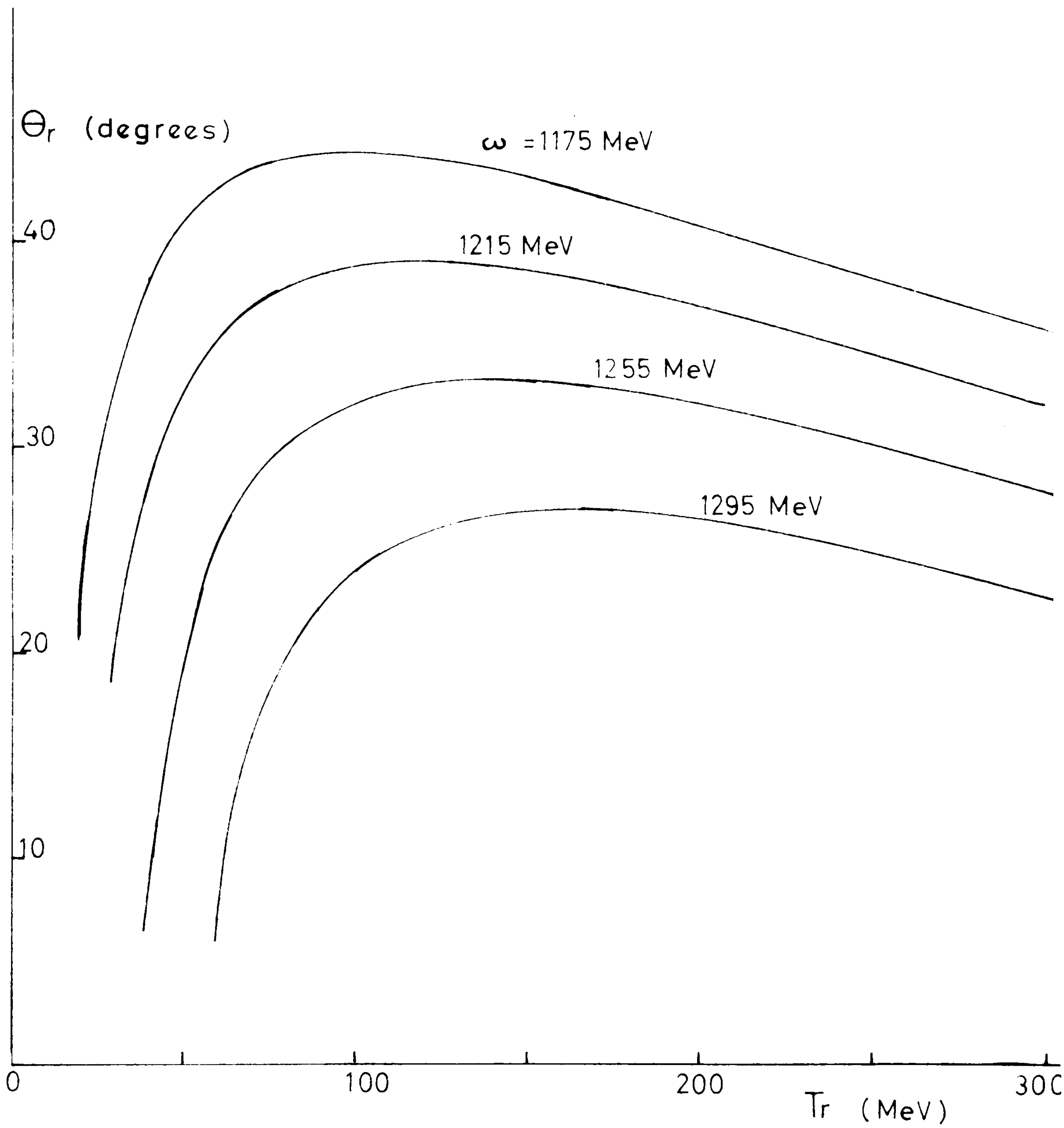

Figure 3.1

$pp \rightarrow p_r(p\pi^0)$

Lab. Scattering Angle (Θ_r) vs. Kinetic Energy (T_r) for various ($p\pi^0$) masses (ω).

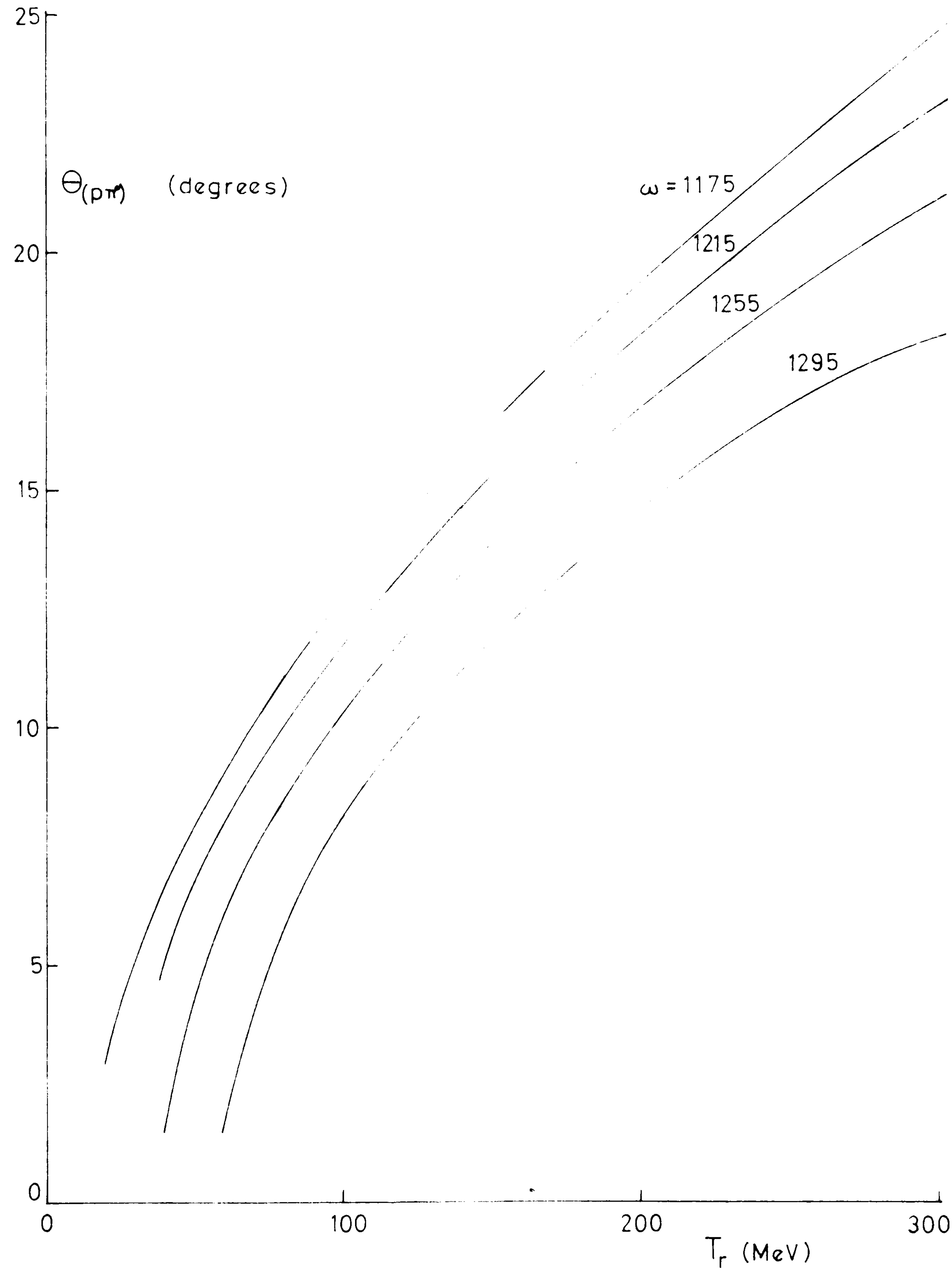

Figure 3.2

$pp \rightarrow p_r\,(p\pi^0)$

system to detect the recoil proton had to be mounted at about 30° to the beam line and had to be about 20° wide. To measure the recoil proton energy, a stack of chambers, with aluminium absorber between each, was used. (The energy absorption for protons traversing Al is well known.) This had an energy resolution of 7 MeV, but multiple scattering in the aluminium made it inadequate for measuring the proton direction. Two pairs of chambers, between the range stack and the target, were used for this. Two counters before the stack and one after were required to indicate that a charged particle had entered, but not traversed, the set of recoil chambers.

The proton from the isobar decay lies within a cone centred about the isobar direction. The opening angle for this cone varied between about 10° and 20° (<u>Fig. 3.3</u>) and could, in most cases, intersect the outgoing beam. The counters and two pairs of spark chambers to detect this proton had to be mounted with adequate clearance for the beam; they fully covered one half the decay cone of events of interest.

The detection system as described above would be triggered by any interaction giving rise to two charged particles entering the counters. pp elastic scattering at 1 GeV has a minimum opening angle of 78° and so could not enter the counters, but

$$pp \rightarrow d\pi^{+}$$
$$\rightarrow pn\pi^{+}$$

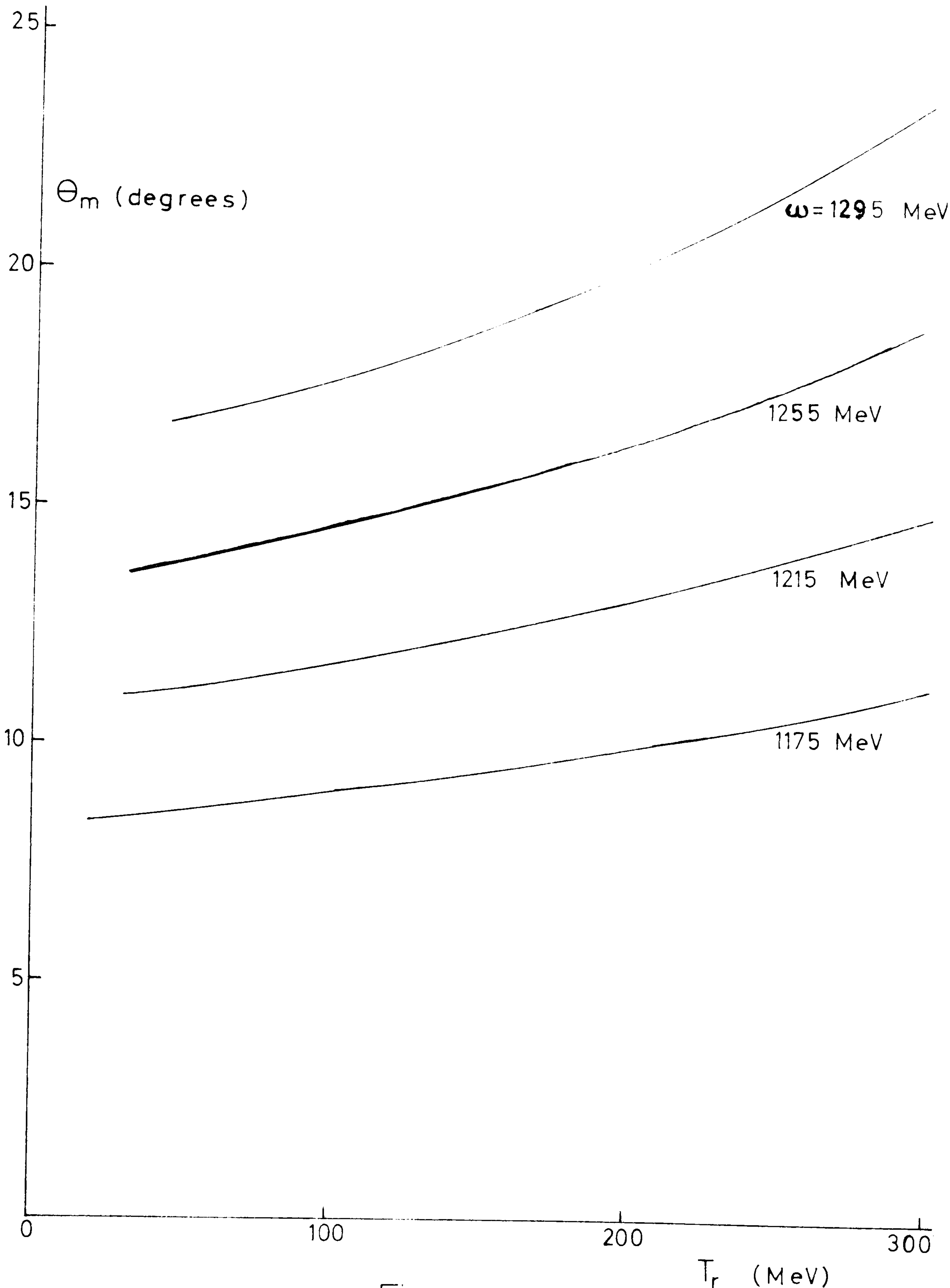

Figure 3.3

$pp \rightarrow p_r(p\pi^\circ)$

Maximum Lab. Angle (Θ_m) between p and ($p\pi^\circ$) direction vs. Kinetic Energy (T_r) of p_r.

would both trigger the system. Interactions with more than one pion can be ignored at 1 GeV, and of the above $pn\pi^+$ has a much larger (~100x) cross-section than $d\pi^+$. Any π^+ entering the system was rejected by

a) requiring a minimum energy loss in the scintillation counters before the range chambers (at the same energy, the π energy loss is ~ 50% that of a proton)

b) putting a threshold Cerenkov counter in the isobar proton detection arm. Typically, this had to distinguish between pions with velocity $\geqslant$95% that of light and protons with velocity $\leqslant$ 84% that of light.

So that geometrical correction factors should not vary too much, the target had to be as small as was compatible with an event rate of about 1 per machine pulse. A cylindrical target,~3 cms diamter, equivalent to 0.21 gms/cm^2 hydrogen, was used. The walls of this were 0.005" thick nylon, to minimise interactions in the walls and hence reduce background subtraction.

The beam had to be well collimated and focussed, so that at the target its dimensions were small compared to the target.

Coincidences between the first two counters of the recoil telescope were to be used as a monitor of the number of protons into the target, per event. This is necessary, of course, to establish magnitudes for cross-sections measured, the ratio of monitor counts to total beam being established by simultaneous measurement at low beam intensities. This roundabout procedure was necessary because the operating beam intensity ($\sim 10^8$ protons/sec) would have saturated the counters. In practice, this monitoring system met with difficulties and was abandoned.

Details of the experimental design are given in the next chapter; the general arrangement is shown in Fig 4 2.1.

Chapter 4 Experimental Arrangements

4.1 The Beam

The beam layout is shown in Fig. 4.1.1. Q1 and Q2 were 6" aperture quadrupole magnets. When full beam intensity was required, they brought the extracted proton beam to a focus at F_1. Because the spill time was about 1 msec. only, the beam intensity of $>10^7$ protons/pulse would have saturated the spark chambers, and to reduce intensity these quadrupoles were not used. It was possible to reduce beam intensity further by scattering the internal beam off the edge of the extraction coil, rather than extracting it. This reduced intensity at the target to about 10^3 protons/pulse.

C1 was a large C-magnet (aperture 48" x 16" x 6") which bent the beam through 14.85°. The field in this magnet was stabilised by controlling the magnet current, using a Nuclear Magnetic Resonance probe to monitor the field. The field of 9.75 Kgauss was stable to $\pm$ 0.5 gauss.

Q3, Q4, Q5 and Q6 were a quartet of 4" aperture quadrupole magnets, which brought the beam to a horizontal focus at F2, the target position. These magnets were current stabilised.

COL was a 24" long steel collimator. It had an aperture 1 cm. wide and 0.5 cm. high. Both this, and the beam exit channel through the synchrotron shield wall, were surrounded by lead bricks.

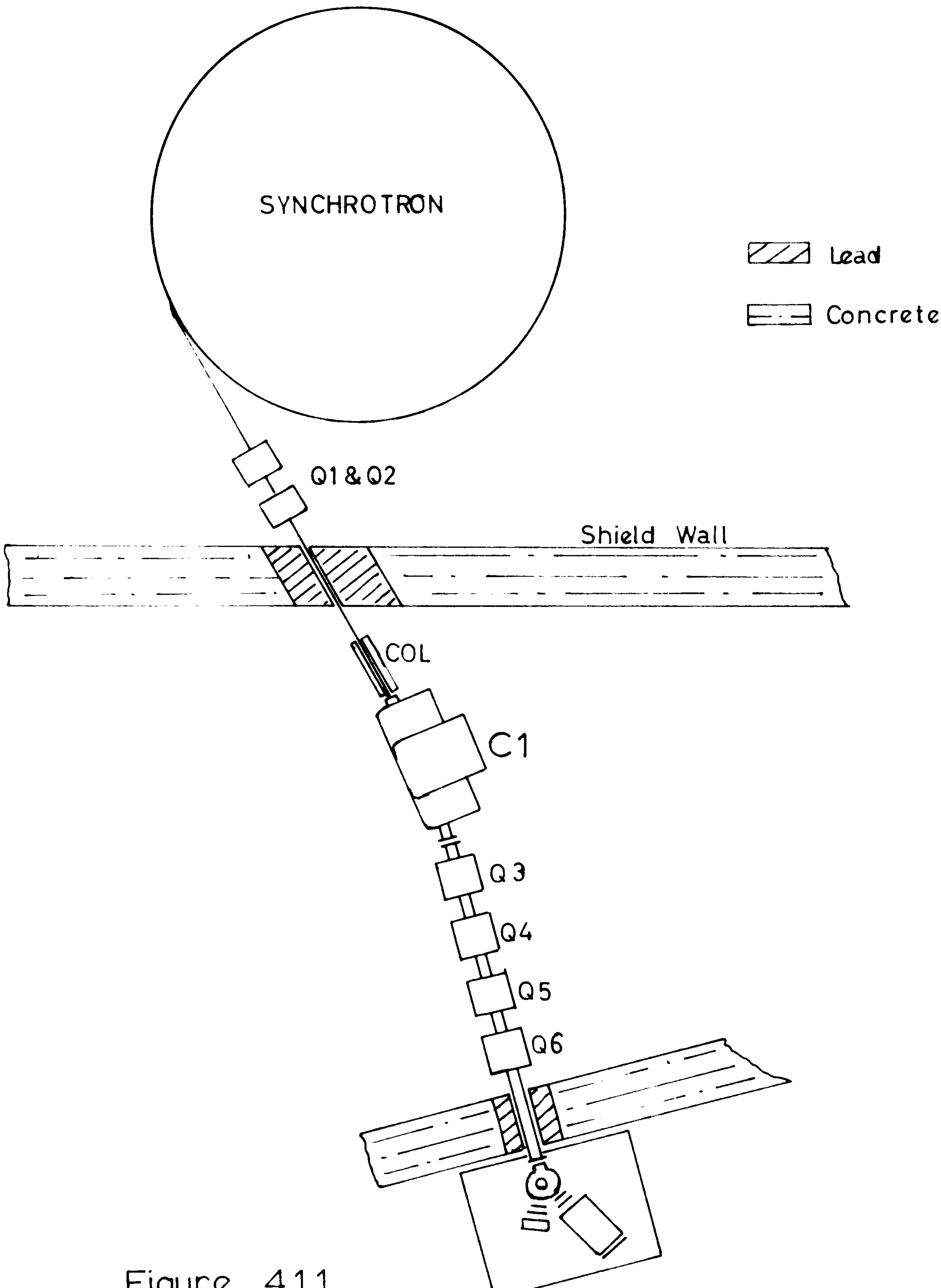

Figure 4.1.1

The Beam Line (not to scale).

Between the collimator and the target the beam travelled through 4" vacuum piping, in two sections: a curved 6ft. section inside the C magnet aperture, and a 12 ft. section through the quadrupoles. The vacuum was a rather coarse 1-2 mm. of mercury, sufficient to reduce multiple scattering in the air from ~ 4 to ~ 0.15 milliradians.

The 3 ft. thick wall of lead bricks surrounding the vacuum piping immediately before the target was constructed in an attempt to reduce the number of non-beam particles (especially neutrons) travelling with the beam.

Initial beam transport calculations were made using the AERE-NIRNS computer programme TRAMP. The beam elements were accurately sited according to the "Tramp" calculations, and tuned to their optimum current settings by trial and error, starting from the TRAMP predictions. Polaroid Land film (high speed Type 3000) was used to observe the beam profile at various points along its path. An exposure of 10^8-10^9 protons cm^{-2} gave a clear image on the film.

A counter scan of the beam at the target position was then made, using two counters with 1/8" x 1/2" and 1/4" x 1/4" scintillator fingers (former dimension facing beam) and an ionisation chamber immediately in front of the counters to give a measure of absolute beam intensity. The table on which the apparatus was mounted was then aligned accurately with respect to the beam line (to $\pm$ 1 mm.).

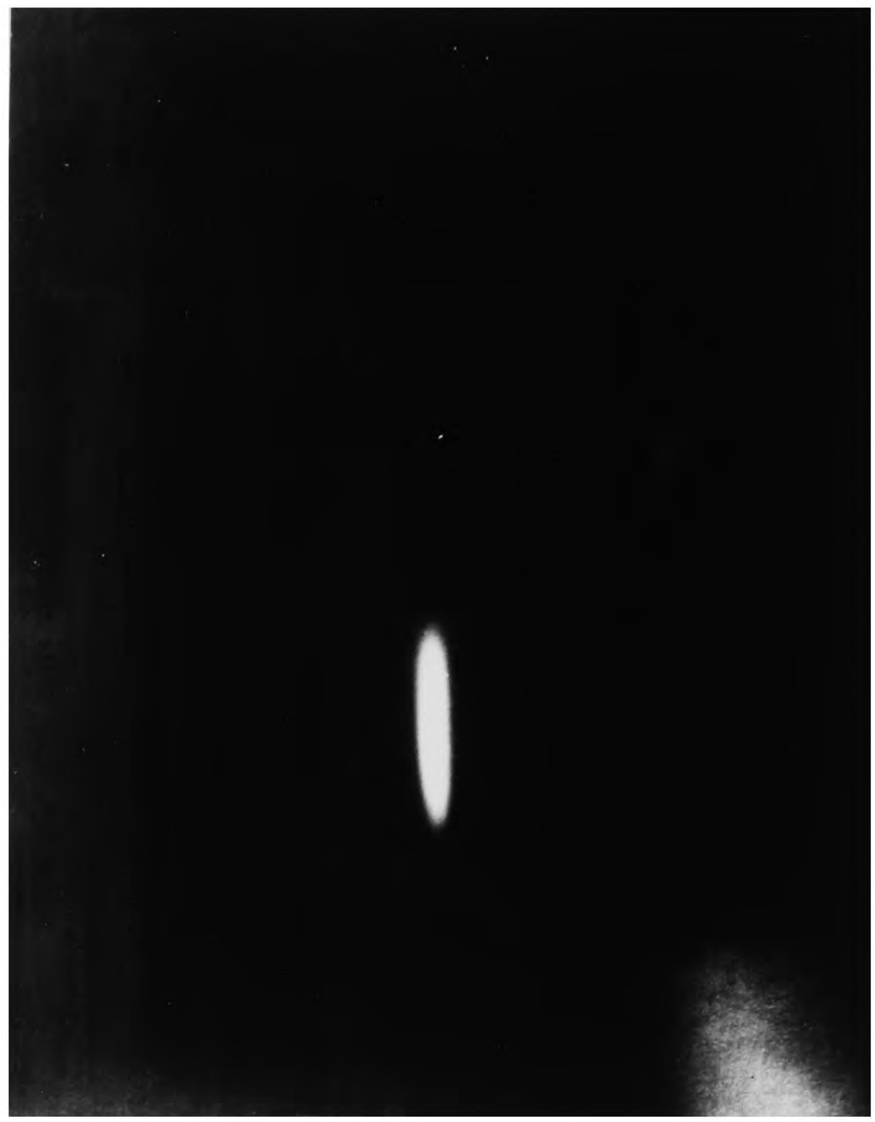

Figure 4.1.2

Beam Profile

During the course of the experiment the beam focus and apparatus alignment were frequently checked by exposing Polaroid Film in holders before and after the target vessel. These holders were marked to define the beam axis of the apparatus. Fig. 4.1.2 shows such an exposure at the entrance to the target vessel: the beam profile is clearly visible. At the target the beam was about 1.5 cms high and 3 mms wide.

No attempt was made to measure the incident beam energy. From the parameters of the synchrotron the beam momentum at extraction was calculated to be 1.705 ± 0.015 GeV/c. When allowance has been made for the material en route, this gives 990 ± 10 MeV for the kinetic energy of the protons at the target.

4.2 The Experimental Equipment

The overall layout of the experiment is shown in Fig. 4.2.1. The liquid hydrogen target, counters and the spark chambers with their lens and mirrors were mounted on an alumiñium platform bolted to a rigid steel stand, mounted on castors for ease in positioning. When it was in position, screw jacks took over from the castors and the platform levelled and aligned with respect to the beam line. A survey showed this alignment to be accurate to better than $\pm$ 1 mm, but the target was not included in this survey since it was bolted to the platform and assumed to be accurately placed. Later, it was found to have been out of its true position (see Chapter 5).

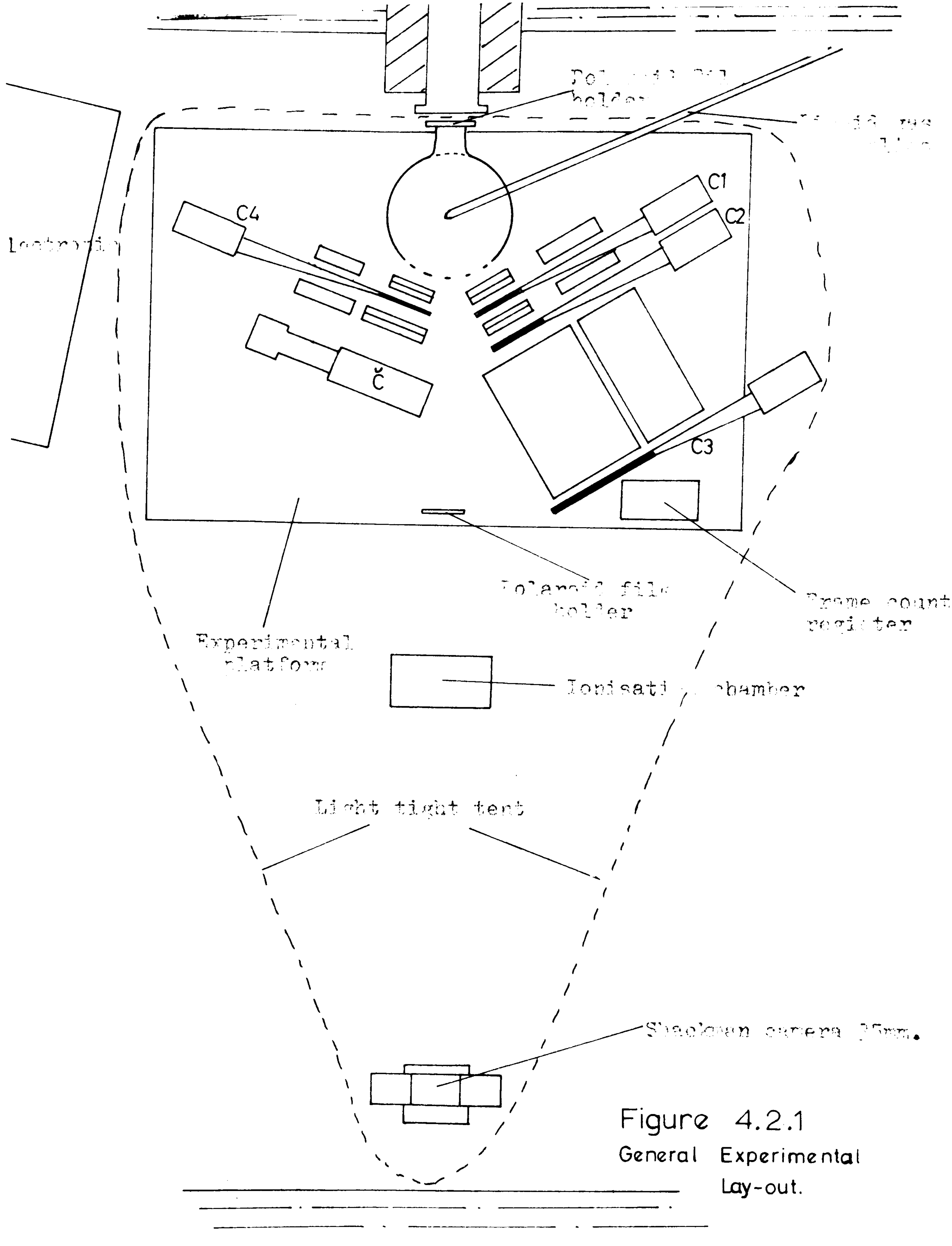

Figure 4.2.1
General Experimental Lay-out.

4.2.1 The Liquid Hydrogen Target

This was of entirely conventional construction. Made essentially of brass, the target system comprised four separable sections: the outer vessel, the liquid nitrogen shield, the liquid hydrogen reservoir and the target appendage (Fig. 4.2.2).

The beam entrance window in the outer vessel was 1.25" diameter and covered with 0.001" thick "Melinex"; the exit window, much larger because of the angular spectrum to be covered, was 8" x 4", with 0.01" "Melinex". "Araldite" epoxy resin sealed the "Melinex" to the brass. The system vacuum, with liquid nitrogen and hydrogen in, was about 3.10^{-7} torr. Two pumps were used to maintain this vacuum: a rotary backing pump and a 2" oil diffusion pump.

To guard against target rupture and the danger of subsequent explosion, a spring loaded flap valve, venting directly to the atmosphere via 4" flexible hosing, was fitted to the outer vessel.

The liquid nitrogen shield was suspended from the top of the outer vessel by ½" diameter german silver tubes, used as boil-off and filling tubes. German silver was used because of its low thermal conductivity. The copper radiation shield attached to the bottom of the liquid nitrogen shield had windows cut into it, matching those in the outer vessel. These windows were covered by 0.001" thick aluminium foil, so that the target appendage was completely surrounded by conductor at liquid nitrogen temperature, minimising heat radiation to the appendage.

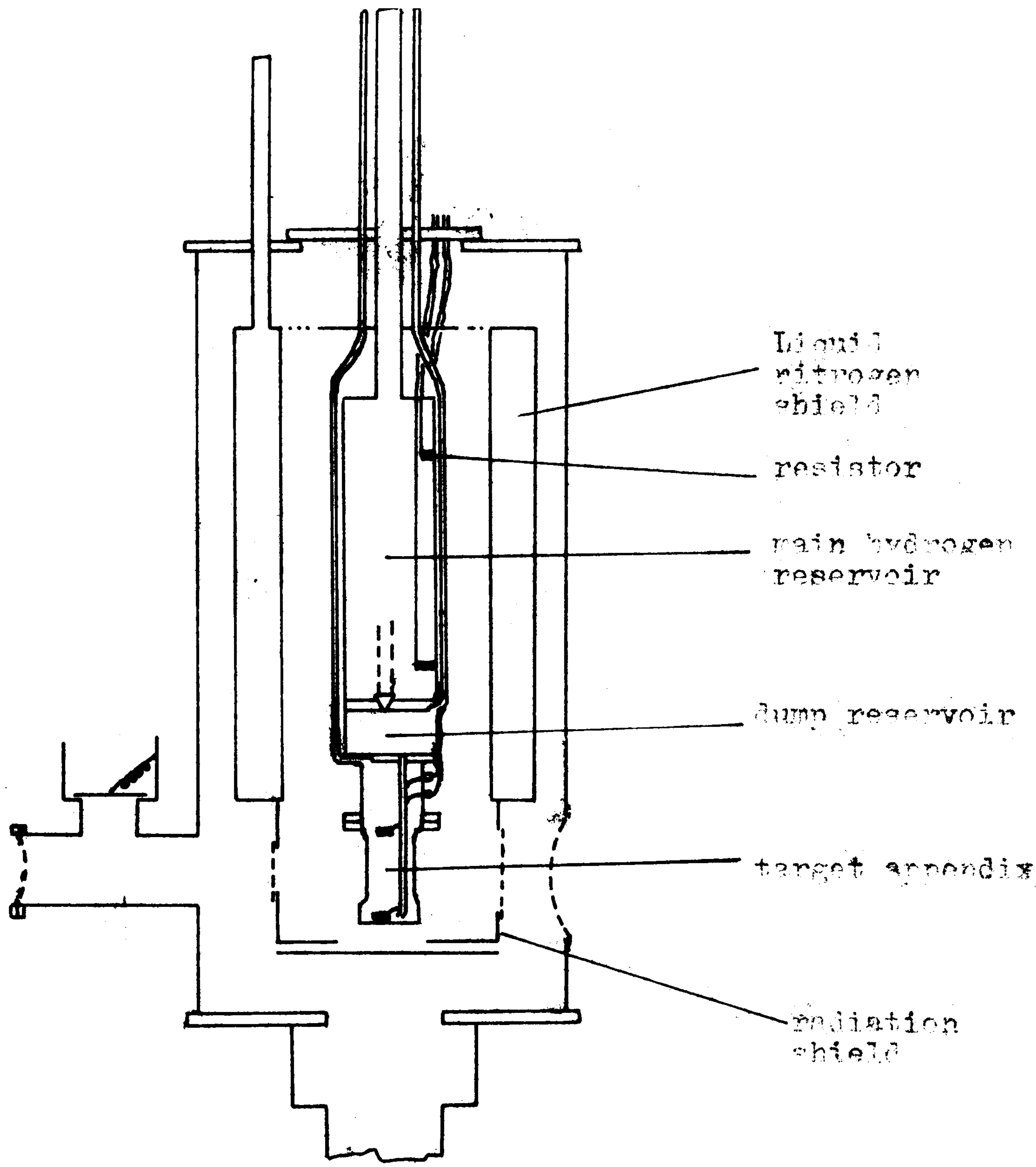

Figure 4.2.2

Cross section of liquid hydrogen target (not to scale)

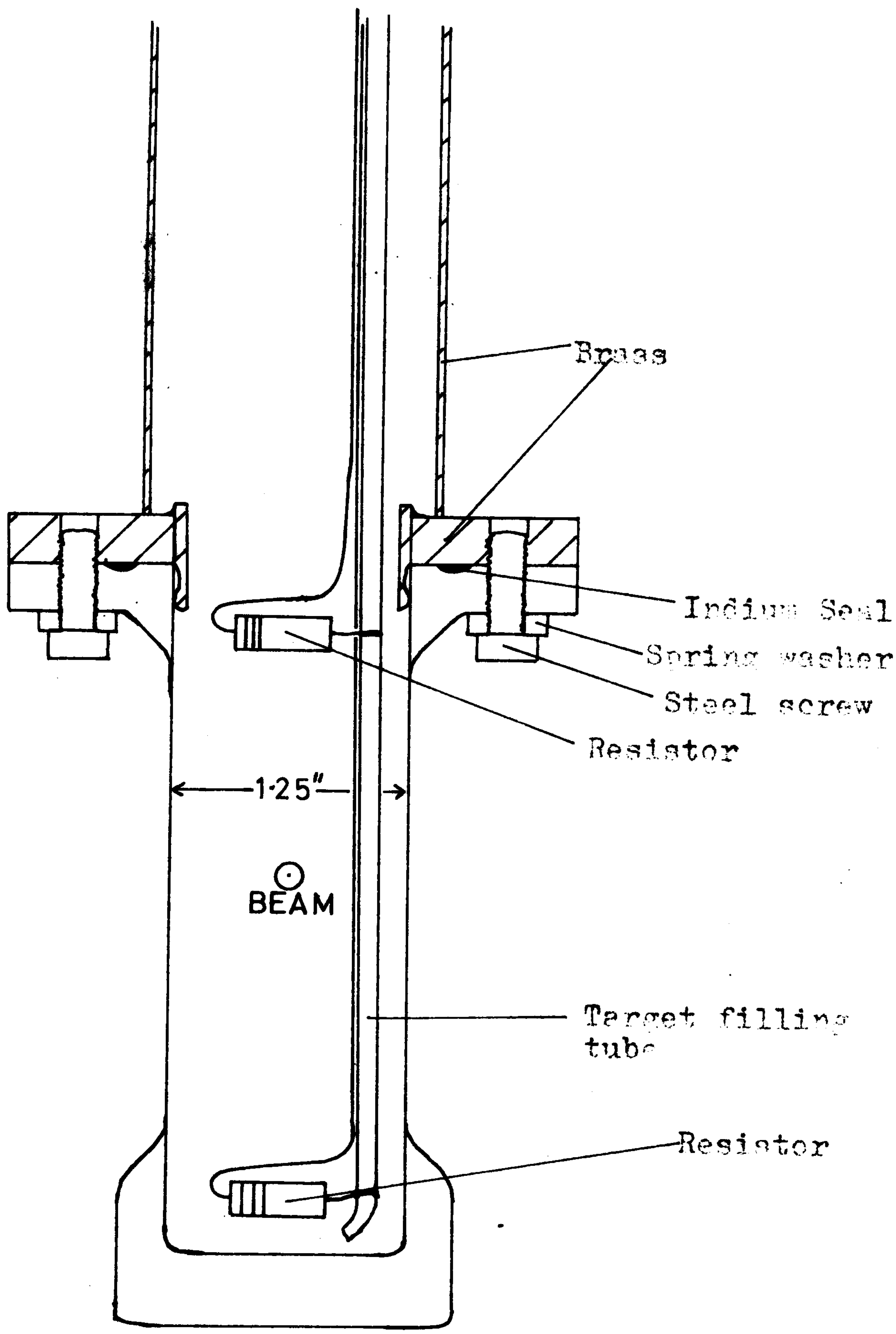

Figure 4.2.3
The Target Appendage. The walls were 0.005" thick.

The liquid hydrogen reservoir had a large upper chamber, capacity 1.2 litres, connected via an externally controlled (from the top of the target) needle valve to the target 'dump' reservoir. This filled the appendage via a small-bore stainless steel tube, and both it and the appendage had separate german silver boil-off tubes. The appendage could be emptied into the 'dump' reservoir by closing off its boil-off tube and allowing the pressure in it to rise, forcing liquid to return up the connecting tube.

The cylindrical target appendage, 1.25" in diameter and about 10 cms. tall, was machined from a block of solid 'Delrin', a hard nylon of high tensile strength. It is shown in Fig.4.2.3, which also illustrates the vacuum tight nylon-brass joint. The target walls were 0.005" thick, equivalent to about 5 milli-grammes material. Others were made with walls 0.003" thick, and of hard nylon, but were not used.

A system of resistors was used to provide an indication of the liquid levels in the various vessels. Their approximate positions are shown in Fig. 4.2.2. Carbon resistors, nominally 68 ohms, 1/4 watt were used. These had a resistance of about 120 ohms in liquid nitrogen and 150 ohms in liquid hydrogen, but much less in vapour because the slower heat dissipation allowed the resistor to heat up. Each resistor formed part of one arm of a Wheatstone bridge network. For the liquid hydrogen levels, the networks were balanced when the resistor was immersed in liquid, and any out-of-balance current was shown on a micro-ammeter.

This system proved unreliable for the target appendage. However, a quick check of the counting rates with full electronic logic proved a reliable method of assessing the state of the target, which was useful, since at one point during the experiment an intermittent blockage of the appendage boil-off tube made much of the data useless because of the ambiguous target status. After this had cleared itself a more frequent check on counting rates was instituted.

The liquid hydrogen reservoir had to be replenished by hand every 12 hours or so, but the liquid nitrogen refilling system was automatic. When the bottom resistor in the nitrogen shield was about 1/4" above the liquid level, the out-of-balance voltage across its bridge network activated a small moving coil relay. This activated a larger relay which switched on a 3-way solenoid valve. Normally this allowed a dewar of liquid nitrogen to vent to the atmosphere; when switched on, however, it connected the dewar to an overpressure of about 1 psi. of nitrogen gas, forcing the liquid from the dewar into the shield via an asbestos lagged transfer tube. The top resistor balanced its network when in vapour: on becoming submerged the above procedure was repeated with the solenoid valve being switched off, and transfer stopped.

Before the experiment, considerable trouble was experienced with the glass-to-metal seals through which electrical contact to the liquid hydrogen level resistors was made. These invariably cracked when cycled between room and liquid hydrogen temperatures. They were replaced by ceramic seals and no further trouble was experienced.

4.2.2 Scintillation Counters, Cerenkov Counter and Electronic Logic

The scintillation and Cerenkov counters, and the spark chambers with their mirrors and lens, were mounted on two subframes bolted to the top of the experimental platform (Fig. 4.2.4). This system allowed easy assembly with accurate positioning.

The size of the counters was dictated by the need to make the event rate reasonable at about 1 per pulse, and the geometrical biasses nearly constant in the kinematical region of interest. NE102A plastic scintillator was used: 1/8" thick in counters 1 and 2 (to reduce multiple scattering), 1/4" thick in counters 3 and 4. These scintillators were mounted in 1/4" thick perspex frames connected via perspex light guides to the Mullard 56 AVP 2" photomultiplier tubes. The light guides, about 10" long, relied on total internal reflection, and to reduce light losses aluminium foil was wrapped round scintillator and light guide and the assembly made light tight with black P.V.C. tape. With about 2 KV across the tubes and a dynode chain current of about 0.8 mA, 990 MeV protons gave a dynode pulse height spectrum centred about 1.6 volts. All the photomultipliers were supplied with E.H.T., via a distribution board, from a single "Oltronix" 3KV unit. This was very stable.

The 12" x 7.5" x 5 cms. thick threshold Cerenkov counter was filled with fluorochemical FC75 ($C_8F_{16}O$) of

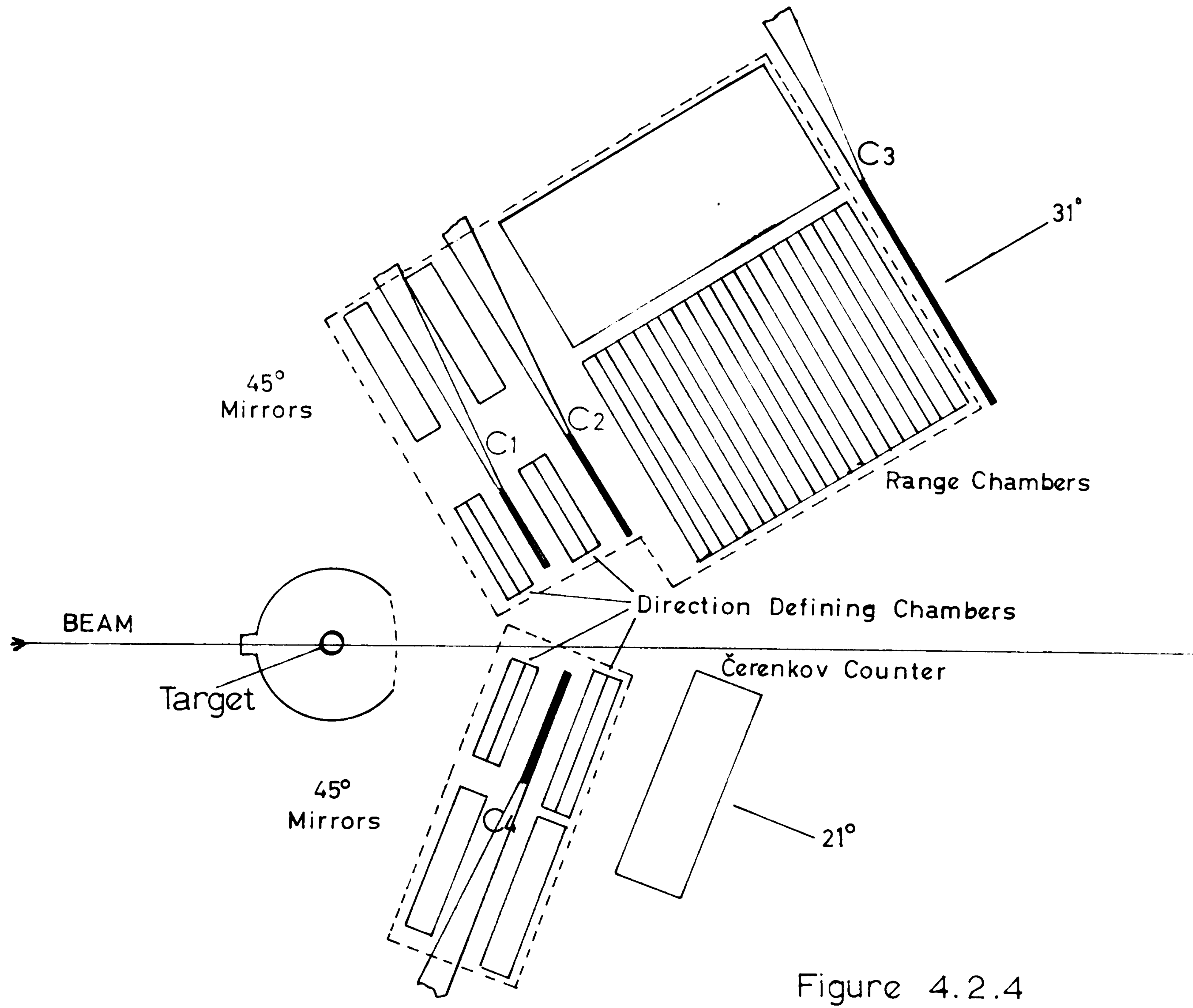
C3
31°
45°
Mirrors
C2
C1
Range Chambers
Direction Defining Chambers
BEAM
Target
Čerenkov Counter
45°
Mirrors
C4
21°

Figure 4.2.4

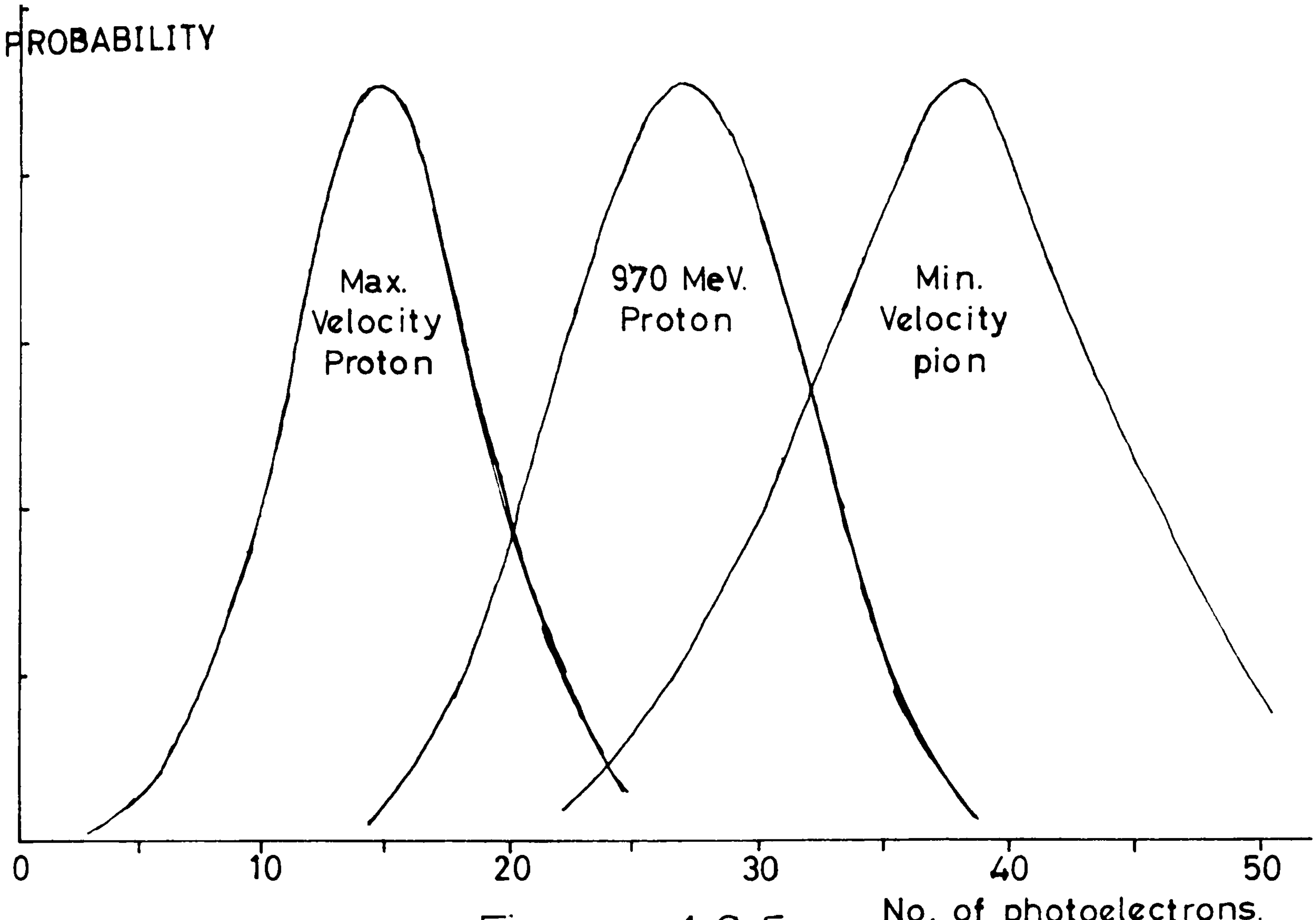

Figure 4.2.5

Theoretical pulse height spectrum in Cerenkov cntr.

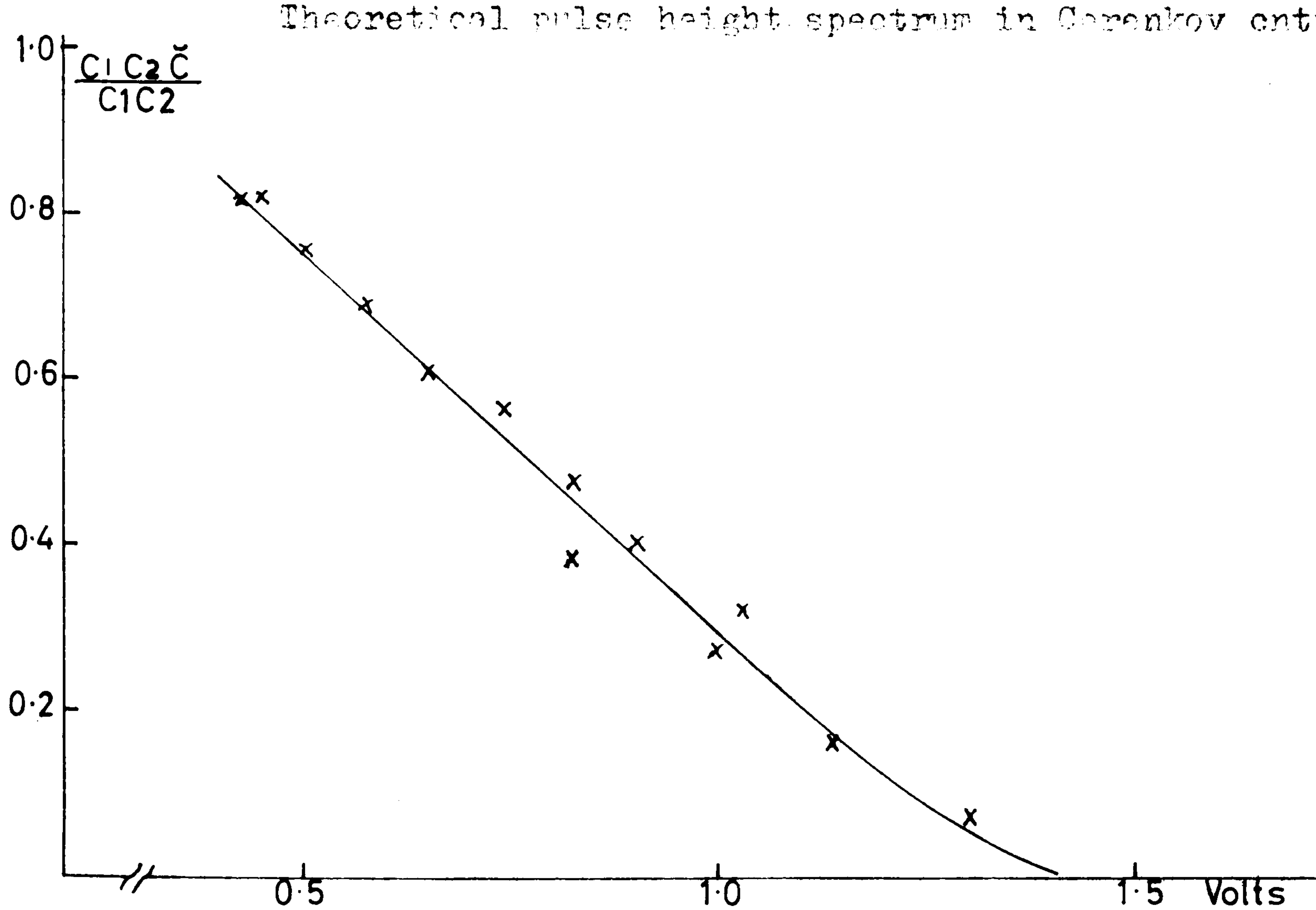

Figure 4.2.6

Integral Bias curve for Cerenkov Counter.

refractive index 1.275, corresponding to a minimum β of 0.785 - equivalent to 575 MeV for a proton or 83 MeV for a pion. The body of the counter was made of perspex, the interior being pa inted with a diffuse suspension of magnesium oxide in clear lacquer to provide the internal reflecting surface. Four 56 AVP photomultipliers,mounted in pairs on two of the sides, looked directly into the counter and the system was again made light tight with aluminium foil and P.V.C. tape. There was no evidence that light collection efficiency varied significantly from one position to another in the counter.

The output pulses from the four photomultipliers were added, and the added pulse went via a discriminator into the anti-coincidence channels of two of the coincidence units. This arrangement enabled pions to be distinguished from protons, as can be seen by reference to Fig. 4.2.5 which shows the theoretical estimates of the pulse height spectrum for each of the three cases:

a) maximum velocity protons from isobar decay

b) 970 MeV protons

c) minimum velocity pions from isobar decay

By setting the discriminator bias at the halfway point in the integral bias curve for beam (990 MeV) protons (Fig. 4.2.6 shows a typical bias curve) practically all pions gave discriminator output pulses, whereas few protons from genuine events could do so.

The output pulses of counters 1 and 2 were also put into discriminators with bias levels set by looking at 990 MeV protons. The integral bias curve for protons of this energy showed a peak at an energy loss of about 0.72 MeV, well below the 1.4 MeV mean loss for a 200 MeV proton (maximum legitimate energy in recoil stack) but greater than the energy loss of 50 MeV (or more) pions. Thus most of the pions were eliminated by this pulse height requirement: later discussion of the observed background will show that much of it was attributable to slow pions in the recoil stack of chambers.

Initially, a larger scintillation counter was mounted behind the Cerenkov counter, but as it did not affect counting rates, and as visual inspection of test photographs showed that all tracks on the isobar side went through the Cerenkov, it was removed.

A block diagram of the electronic logic is shown in Fig. 4.2.7. The spark chambers, spark gap and EFP60-QV12 triggering circuit will be described in the next section.

Where possible, standard A.E.R.E. 2000 series equipment was used, with 100 ohm co-axial connections throughout. To keep delays short, all equipment except the scalers and the E.H.T. power supplies (which were in the control room some 25 ft. away) was mounted in racks as near the target as possible (typically, 6 ft. away).

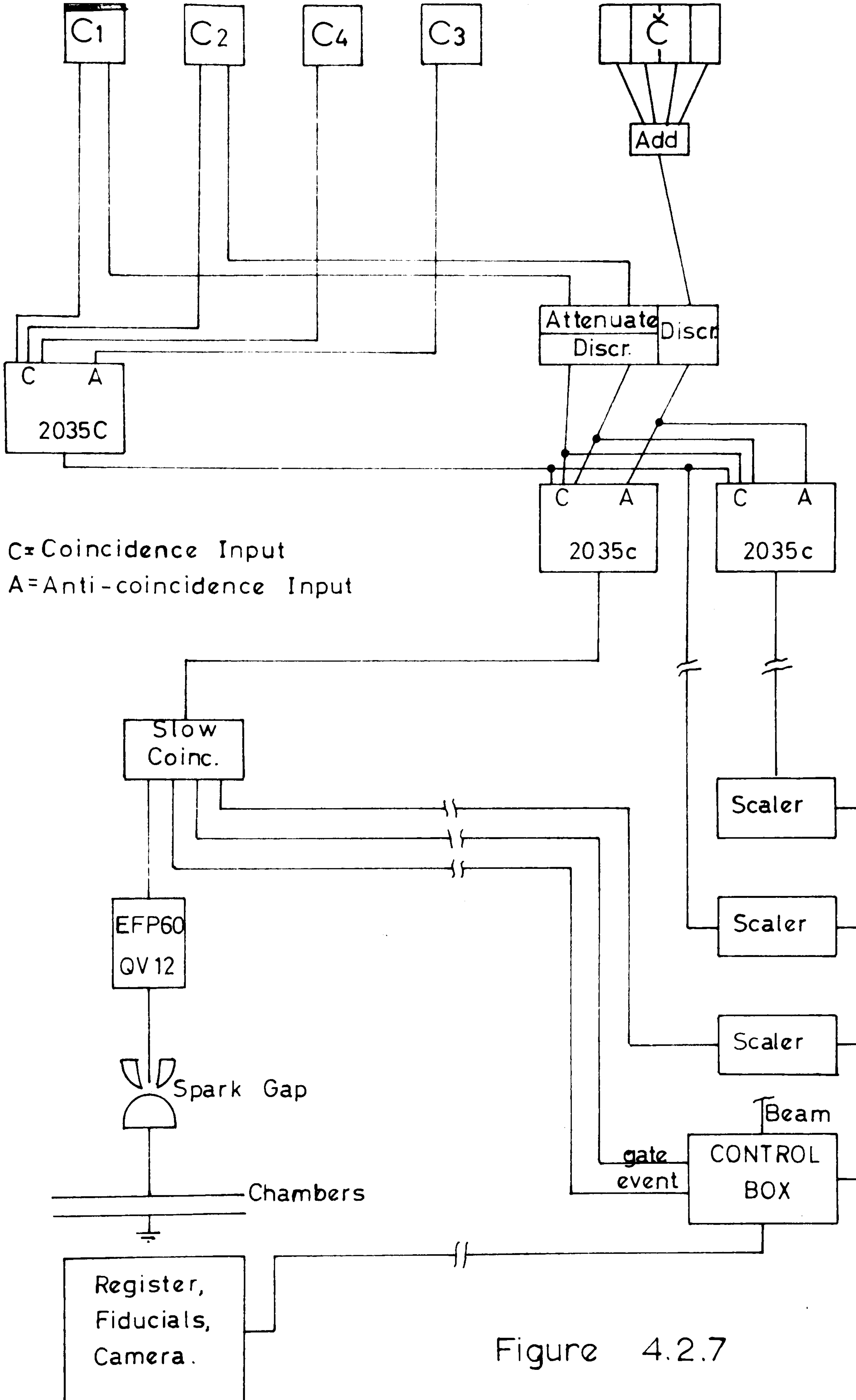

Figure 4.2.7

Block Diagram of Electronics.

The coincidence units used in the final data taking runs were AERE 2035C units. With 3ft. clipping lines on the coincidence channels and 6ft. on anti-coincidence channels, their resolving time was of the order of 10 nsecs., adequate to cope with the beam intensities used and the time jitter in the 56 AVP tubes. (Initially coincidence units of our own design had been used, but they proved unreliable at the high singles rates in the counters, and had to be replaced. A large proportion of the total running time was lost because of the failure of these units.) The slow coincidence circuit (a remnant of the previous coincidence circuitry) was used as a pulse generating and gating circuit. It was gated off by the control box after an event, and was kept gated off until the next machine beam pulse (3 msec. before beam).

Events satisfied the "slow" coincidence requirements $C_1\ C_1'\ C_2\ C_2'\ \bar{C}_3\ C_4\ \bar{C}$ and were counted on two scalers, one driven by the slow coincidence circuit which triggered the spark chambers, and one by the 2035C unit in parallel with the 2035C driving the slow coincidence circuit. This provided a check on the operation of the slow coincidence circuit. In addition, the "fast" channel ($C_1\ C_2\ C_4$) went into a scaler: consistency in the "fast"/"slow" ratio gave an indication that all was well with the system. 10 mc/s scalers were used.

Besides gating the slow coincidence circuit, the control box counted events which triggered the spark chambers, drove the camera and fiducial lights, and operated the event count register on the experimental platform. This latter was included in a photograph of the chambers, and was illuminated by fiducial lights.

The timing of the control box is shown in Fig. 4.2.8. The sequence of operations was:

1) 3 msecs. before the beam, the machine beam gate pulse triggered a univibrator which opened the event gate for 14 msecs.

2) if an event pulse was received, another univibrator closed the gate again, for 25 msecs. (during which time the first univibrator would have closed it, anyway). The event pulse also triggered a univibrator whose output was amplified, to switch a relay controlling the fiducial lights. This univibrator reverted to the stable mode after 1.0 sec., triggering another univibrator which produced the 0.4 sec. pulse for the camera drive and advanced the event registers by one.

3) With this sequence completed, all univibrators were back to normal and the gate closed, awaiting the next beam pulse.

The univibrators initially tended to pick-up R.F. radiation when the spark chambers were fired. Redesign to

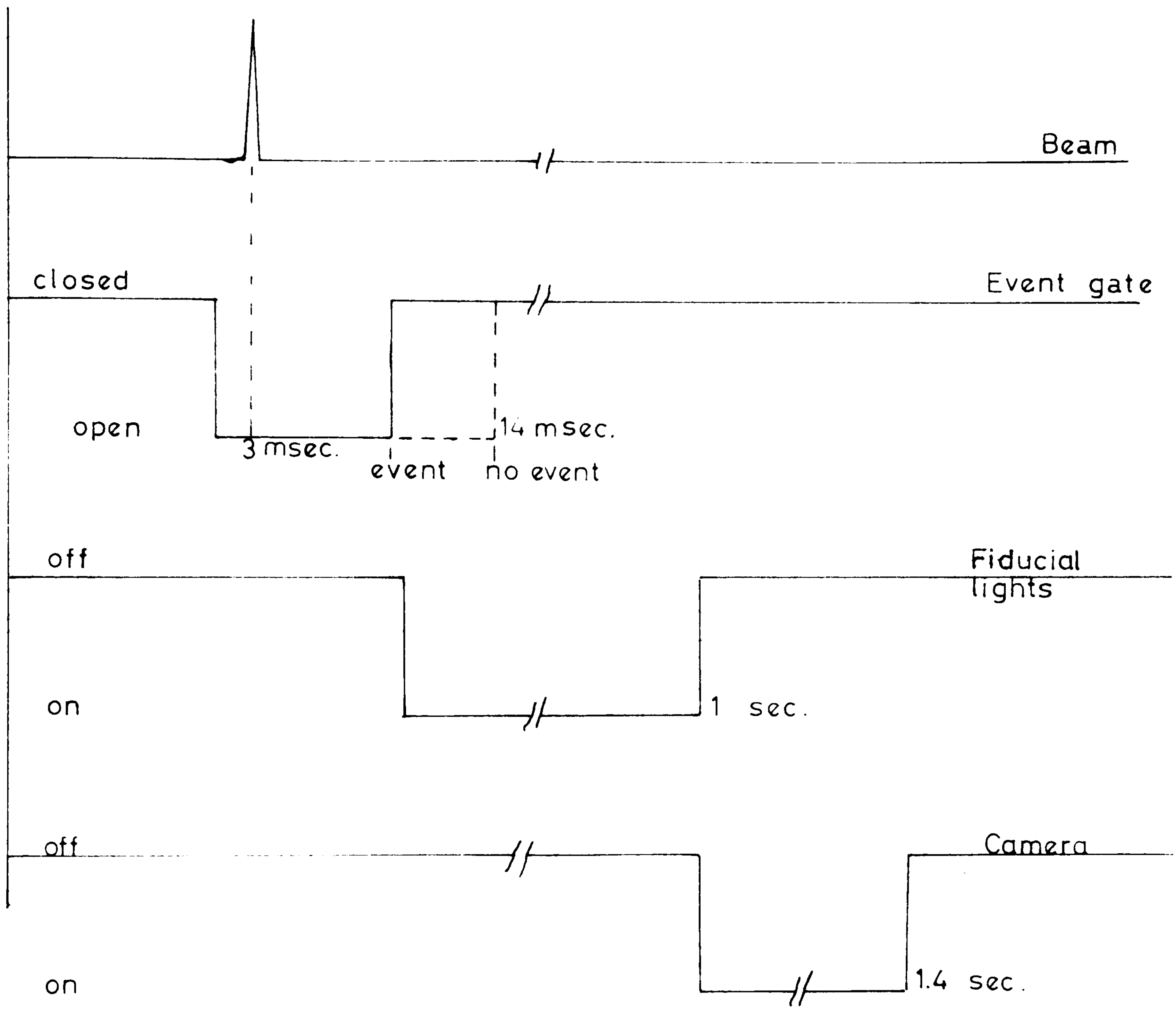

CONTROL BOX TIMING

Figure 4.2.8

reduce sensitivity cured this fault. The scalers also suffered from pick-up, and could not be cured, in spite of extensive shielding with copper, although several types of scaler were tried. Direct counting while data taking was in progress was therefore impossible, and the original scheme of beam monitoring using C_1 C_2 coincidences had to be abandoned, and an ionisation chamber substituted. This was unsatisfactory for two reasons: it was unaffected by the event gate, and so counted total beam, and not beam per event, and it also developed a severe zero reading error which became worse as data taking proceeded. Thus estimates of total beam/event are rather unaccurate.

4.2.3 Spark Chambers and Associated Equipment

Two methods of constructing the spark chambers were used, the chambers to detect the 'isobar' proton being of later design. An exploded view of each type of chamber is given in Fig. 4.2.9. In both cases the frames were masked with 0.005" "Melinex" to stop edge breakdown, caused by a spark tracking along the inside edge of the glass or perspex (where the field discontinuities are greatest). Glass was used for the recoil chambers because it was thought to make for easier construction within the close tolerances demanded. Later experience showed perspex to be superior, and as it also has a lower dielectric constant (2.5 as against ~ 5) glass was abandoned.

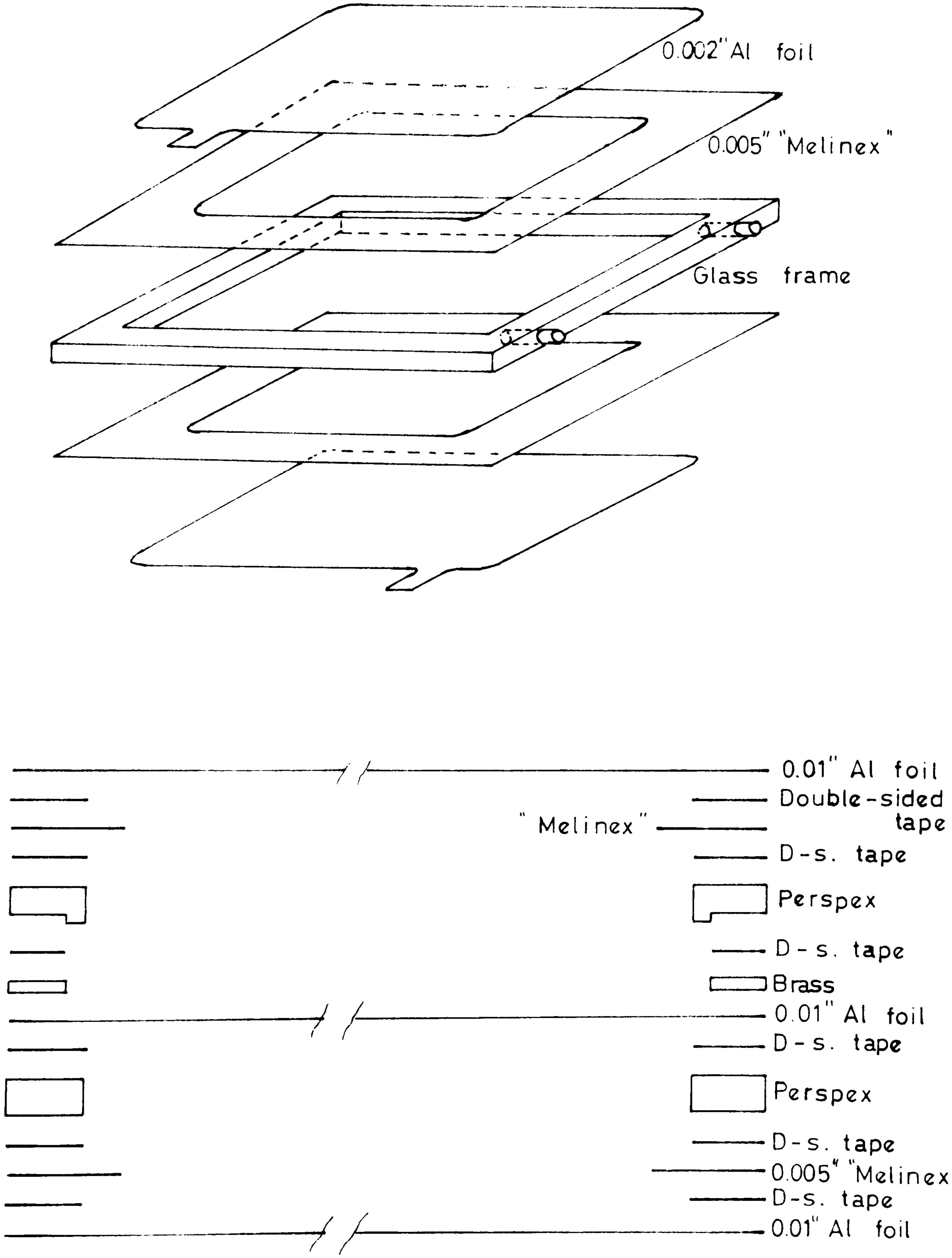

SPARK CHAMBERS

Figure 4.2.9

The plate separation in all chambers was 1/4", chosen because this dimension seemed a good compromise between the conflicting requirements of large separation for high efficiency and small separation to ensure a low H.T. pulse to induce avalanche breakdown, and to reduce the clearing field required to sweep away unwanted ions. (See e.g. ..A. Wenzel (1) for a modern review of the spark chamber field, and copious reference to the literature.)

The first four chambers on each side were mounted in pairs, in Tufnol clamps, with an H.T. plate between two earthed plates. These were used to define the direction of the outgoing protons with an angular resolution of $\pm \frac{1}{2}^{\circ}$ for tracks nearly perpendicular to the plates i.e. for all tracks of interest.

The range chamber was made up of 22 individual chambers, $6\frac{1}{2}$" x $4\frac{1}{2}$" active area, of the glass frame type. Between these chambers were graduated thicknesses of aluminium absorber, chosen so that the mean difference in kinetic energy between protons stopping in adjacent chambers was 7 MeV (Table 4...). Thus a proton traversing the first chamber only had a kinetic energy between 53 MeV and 60 MeV, there being a considerable amount of material before the recoil chambers, while a proton stopping in the final absorber had a kinetic energy between 193 MeV and 200 MeV. Both ranges and range straggling figures were taken from the tables of Sternheimer (2). Range straggling varied from 1.3% to 1.1%

Range (no. of chambers traversed)	Total Absorber gm/cm^2	Upper Limit on Energy (MeV) of normally incident	
		Proton	Pion
0	3.250	53	23.2
1	4.049	60	26.5
2	4.926	67	29.7
3	5.878	74	33.0
4	6.899	81	36.2
5	7.990	88	39.4
6	9.149	95	42.7
7	10.369	102	46.2
8	11.657	109	49.7
9	12.993	116	53.1
10	14.397	123	56.6
11	15.857	130	60.2
12	17.373	137	63.8
13	18.944	144	67.4
14	20.567	151	70.9
15	22.248	158	74.6
16	23.977	165	78.3
17	25.754	172	82.1
18	27.579	179	85.8
19	29.451	186	89.6
20	31.372	193	93.5
21	33.334	200	97.5

Table 4.2.1 Range Chamber Absorber Parameters

- much less than the 7 MeV uncertainty due to absorber thickness. This 7 MeV uncertainty also swamped the correction to range because the protons were generally not travelling perpendicular to the absorber ($\lesssim$ 2%).

Argon, with alcohol as a quenching agent, was slowly fed through the chambers, at atmospheric pressure. Neon was considered but not used because of its high cost and lower light intensity per spark. The chief advantage of neon is that it allows multiple sparks per gap without impaired efficiency, and a lower H.T. pulse for breakdown. Multiple tracks were not a feature of this experiment, and the chamber was essentially 100% efficient with argon.

The spark chamber pulsing system is shown in Fig.4.2.10. The avalanche output pulse from the slow coincidence circuit was amplified in two stages, by an EFP 60 valve and then a CV12 210 valve, giving an output pulse - 12 Kv., with a rise time of about 10 nsecs. This was fed onto the 1 mm diameter cylindrical tungsten trigger pin of the spark gap. This trigger pin was concentric with the earthed pole piece of the spark gap, which had been drilled out to admit it. The pole pieces of the gap were hemispherical, made from copper-nickel alloy, and mounted in a perspex cylinder containing nitrogen at 75 p.s.i. At this pressure, and with careful adjustment of the gap geometry, the delay in the spark gap could be made less than 60 nsecs.

The spark gap was run with 20 kV between pole pieces.

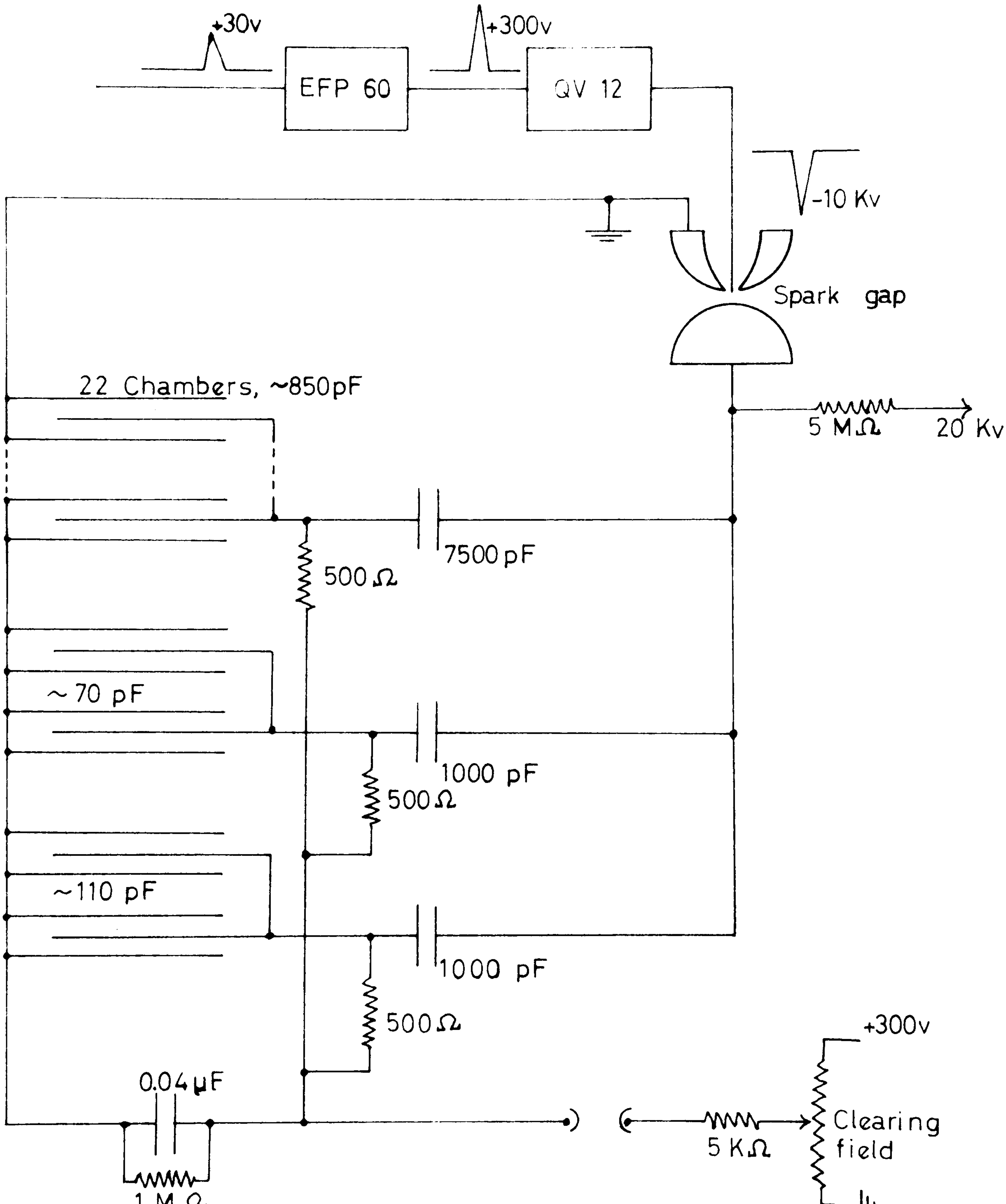

Spark Chamber Pulsing System

Figure 4.2.10

Since the storage capacity before each set of chambers was very much greater than that of the chambers (~ 40 pF each) essentially -20 Kv with a rise time of ~ 50 nsecs. was applied to the H.T. plates on gap breakdown.

An adjustable clearing field was available, but was kept at + 200 v. With an overall delay in the system of ~ 200 nsecs., about half in the QV 12 and spark gap, this clearing field was perfectly adequate. The resolving time of the chambers was not measured.

Because of the low (<0.1 mA) current capability of the 20 KV power supply, the recovery time of the system was of the order of 1 sec. Thus the maximum possible event rate from spark chamber considerations alone was 1 per pulse.

4.2.4 Data Recording

The spark chambers were photographed with a 35 mm, Shackman step-by-step automatic camera fitted with a 150 mm. Zeiss lens. Plane, front surface aluminized 1/4" glass mirrors were used to enable both vertical and horizontal views of each chamber to be included in the same frame. The lens above the chambers, machined from normalised perspex as two segments of a 15 ft. focal length plano-convex spherical lens, brought parallel rays of light from the chambers to a focus at the camera.

Fiducial grids, comprising lines engraved on 1/8" perspex sheet, were mounted on each viewing side of the chambers. They were illuminated for about 1 sec. before the camera wound on by small bulbs set into the perspex. The intensity of the lighting to each grid was variable, so that uniform illumination could be achieved. The events count register, which also appeared on the film, was similarly illuminated.

Kodak 35 mm. PAN X film was used, with the camera aperture f/11. This gave a depth of field of about 12", more than enough to cover the spark chambers. Distortion on the film was not measured directly, but in the course of scanning: this will be considered in the next chapter.

Apart from test strips developed in the course of the experiment, using Kodak D19b developer, the film was developed commercially by Brent Laboratories.

Mechanically, the camera proved most unreliable and as a result of clutch failure many frames were superimposed on the film, making them unscannable. Nearly 25% of the good data was lost in this way.

4.3 Experimental Procedure

Before the start of each session on the machine, all equipment was checked. The scattered-out beam (intensity $\sim 10^3$ per pulse) was most conveniently used for this, since its low intensity allowed one to be in the experimental hall while the machine was running.

First, however, the beam line components were checked by exposing Polaroid film at several places along the beam line. The full extracted beam was required for this.

When the photomultiplier E.H.T. levels had been checked, using a Co^{60} source, the counters were mounted behind the target and timed with respect to each other. At the same time the E.H.T. curves were checked, and the bias levels on the 2035C coincidence units set to lie on the plateau between singles breakthrough and complete cut-off in each channel.

Counting rate vs. discriminator bias curves were taken for counters 1, 2 and the Cerenkov, and the discriminator bias set at the half-way point. (An example of one of these curves is shown in Fig. 4.3.1 .)

Meanwhile, argon was being passed through the spark chambers. These were checked visually for correct operation and then, with the counters remounted in their correct positions, a short test strip of film was run off and developed. This enabled camera focus and fiducial intensity to be checked as well as the chambers.

Data taking commenced after a test of counting rates. Data was taken in "runs", each run number being marked on the board by the events register, and appeared on the film. Each run corresponded to about one 100 ft. reel of film. After each run a short test strip was developed, the target status checked, and the counting rates C_1 C_2 C_4 $\bar{C}_3$ and C_1 C_1'

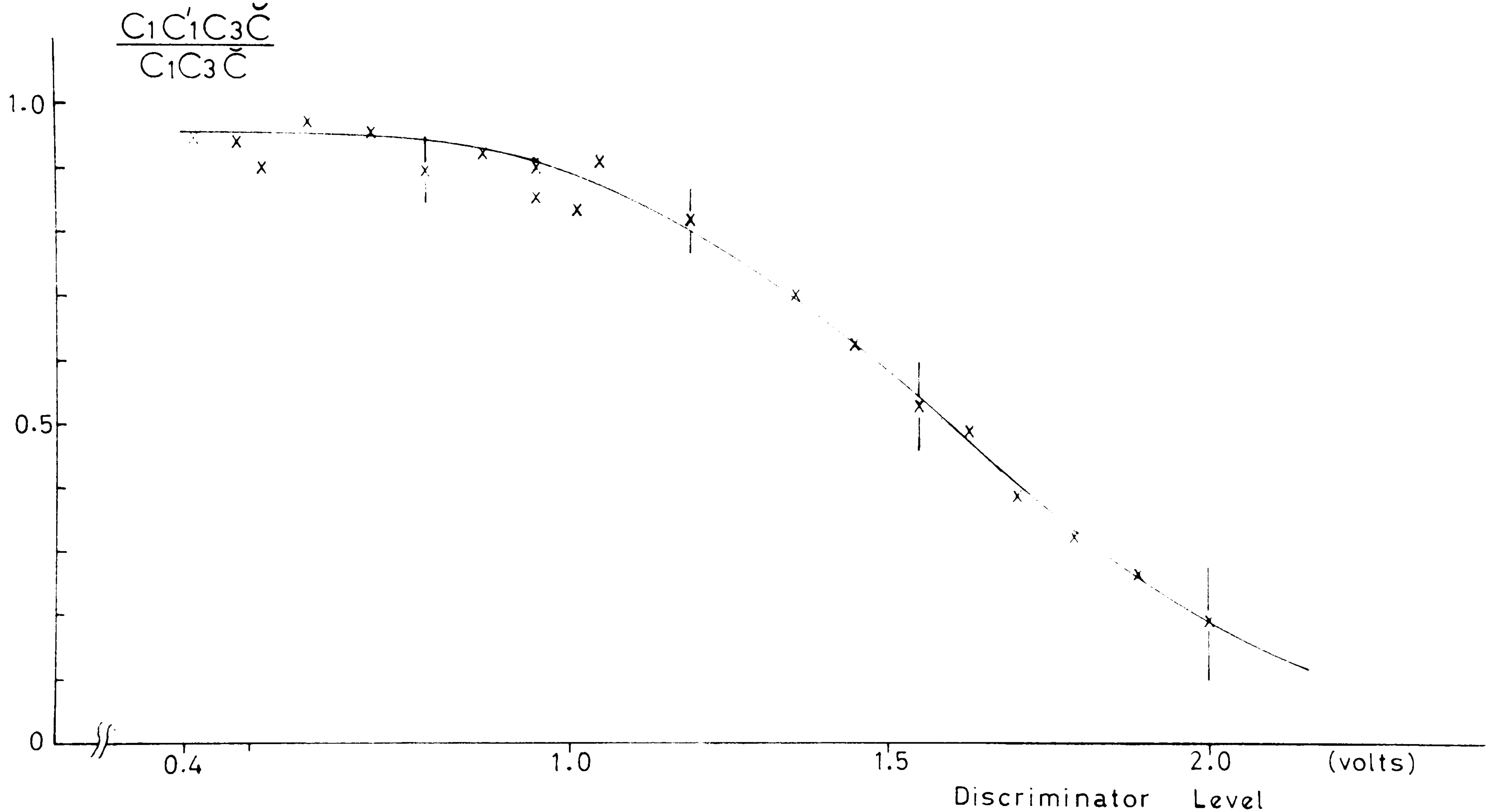

Figure 4.3.1

Integral Bias Curve for C_1

$C_2\ C'_2\ \bar{C}_3\ C_4\ \bar{C}$ were measured. As required for the next run, the target was filled or emptied. Beam time was divided between target full and target empty runs to get equal amounts of beam per good event, the optimum arrangement from the point of view of background subtraction. In practice, this division of beam was not achieved, partly because of the impossibility of estimating beam/event and partly because of the impossibility of estimating the number of good events from looking at test strips.

The beam line, and the target reservoir levels, were checked less frequently, and needed very little attention.

(1) W.A. Wenzel, Annual Reviews Nuclear Science 14, 205 (1964)

(2) R.M. Sternheimer, Phys. Rev. 115, 137 (1959)
ibid. 117, 485 (1960)
124, 2051 (1961)

Chapter 5

When data taking at the synchrotron was completed the information required was either on film or in the experiment log-book. The developed film had to be scanned and events of interest measured for subsequent geometrical and kinematical reconstruction by an electronic computer which then extracted the various distributions of physical interest. The final stage in the analysis was the correction of these distributions for detection efficiency, scanning biasses and background events. From these corrected distributions the related cross-sections were obtained.

5.1 The Scanning and Measuring Machine

The film taken in this experiment was scanned and measured by physicists at Oxford using a measuring machine designed and built at Oxford. This has been described in detail elsewhere (1) so only a brief description will be given here.

The film was projected onto a horizontal table using a commercial 250 watt projector fitted with a condenser lens and a 4" focal length Kodak enlarging lens. The magnification in projection was about 24x and the projected image, as calculated from the 1 cm. spacings of the fiducial grids, was 0.686 ± 0.013 times life size.

The general scheme of the measuring table is shown in Fig. 5.1.1. It comprised a horizontal 27" diameter flat circular table which could be rotated about a vertical axis,

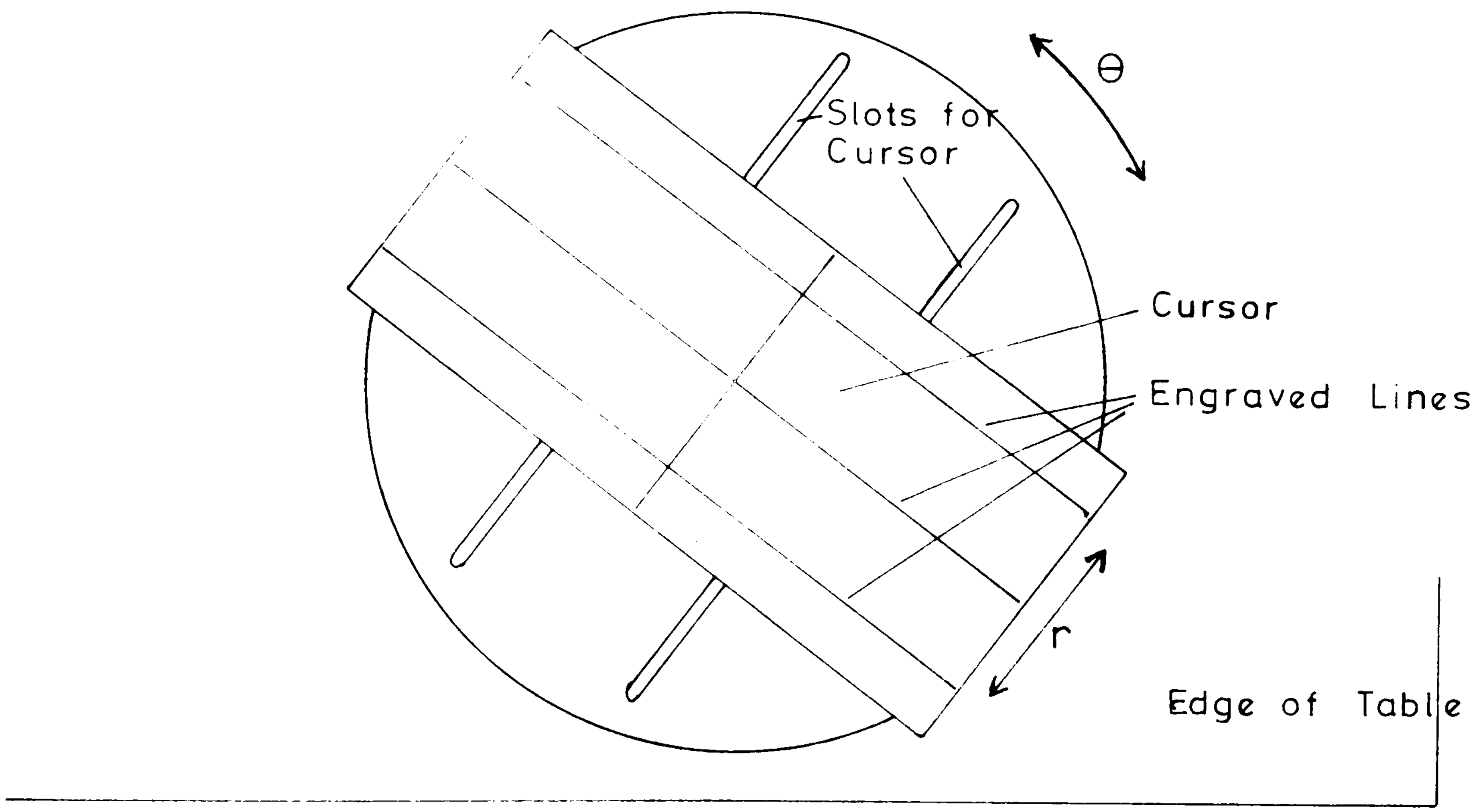

Figure 5.1.1

Scanning and Measuring Table.

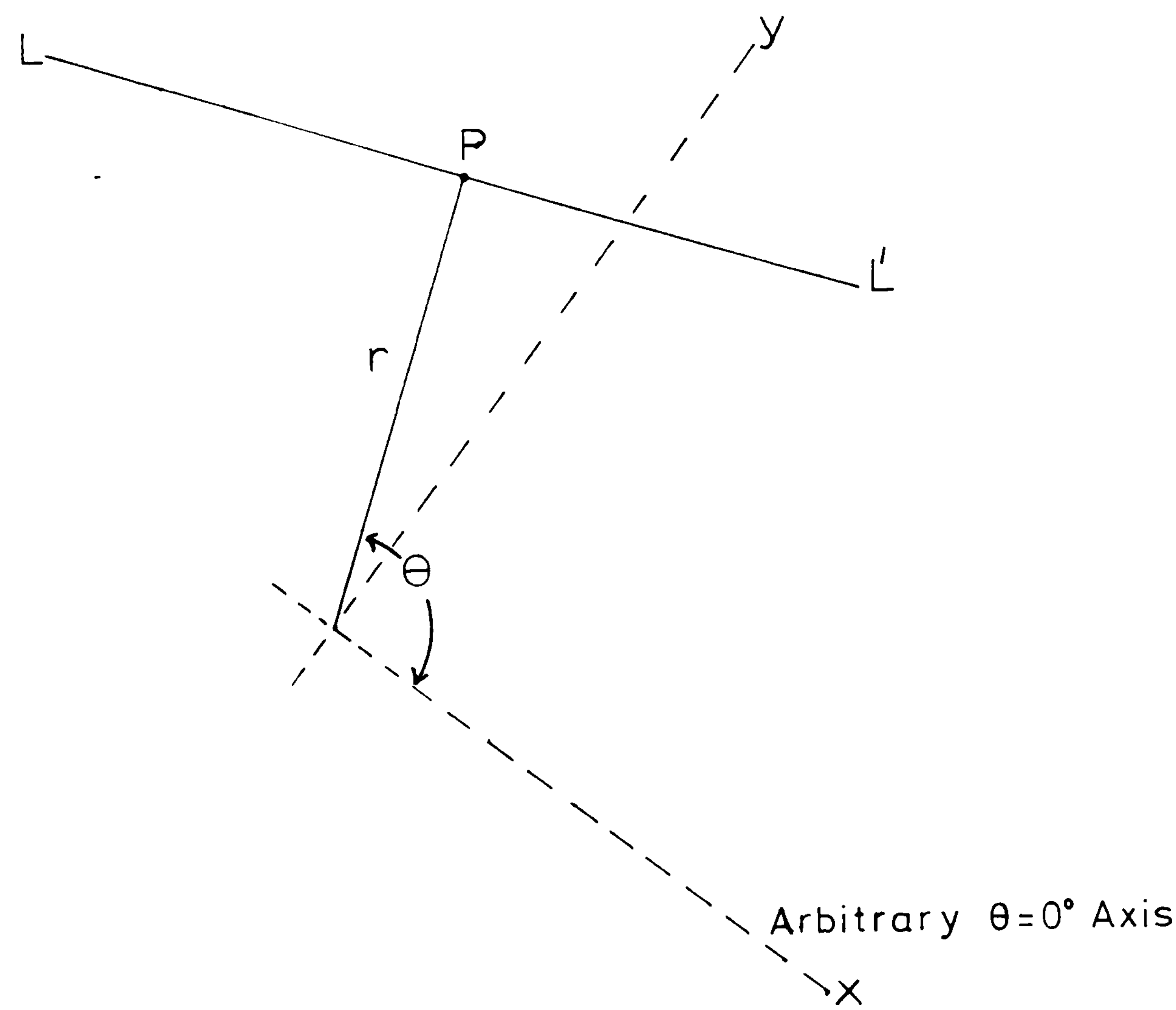

P is the point $(r\cos\theta, r\sin\theta)$

LPL' is the line $y = -x/\tan\theta + r/\sin\theta$

Figure 5.1.2

with a 24" x 12" cursor mounted so that it could slide along a diameter of the rotating table. The table rotated in two large accurately aligned bearings, and the cursor slid on linear bearings along two hardened steel shafts fixed onto the table. The upper surfaces of both table and cursor, onto which the film was projected, were of white plastic. Four reference lines ~~xxxx~~ used in measuring were engraved on the upper surface of the cursor to eliminate parallax errors in measuring.

The table and the cursor were connected to two mechanical (coded disc) binary digitizers, manufactured by Hilger and Watts Ltd., which read up to $2^{13}-1$. A rotation of 360° was divided into 2^{13} parts and the full travel of the cursor was divided into 2088 parts. Tests showed each scale to be linear throughout its range.

The system would thus measure the polar co-ordinates (r, θ) of a point, with θ measured from some arbitrary axis and r corrected for the reading of the cursor digitizer when the cursor centre coincided with the centre of rotation of the system. Equally this system could measure the perpendicular distance of a line from the centre and its gradient (Fig. 5.1.2), thus specifying the position of a line in a single measurement. Since angular measurements were relative the arbitrary $\theta=0$ axis was of no significance, but the position of this axis was measured each morning, along with the reading of the cursor digitizer at the centre of the table, as a check on the machine.

The digitizer readings were decoded and punched onto paper tape in pure binary form. The circuitry to do this was designed and built in Oxford.

A typewriter with micro-switches connected to the keys allowed the machine operator to put additional information on the tape.

Distortion in the projection system was examined by projecting an accurately ruled rectangular grid onto the table and measuring the variation in grid spacings across the table. The magnification was 1.4% greater at the outer edges than in the centre; entirely acceptable since measurement was confined to a small region near the centre of the table.

5.2 Scanning and Measuring the Film

The print of a frame showing a possible good event is shown in Fig. 5.2.1. Clearly visible are the two tracks and their stereo views, together with the fiducial grids, ruled in 1 cm. squares above the direction chambers, and, bottom right, the frame count register and run number.

Such an event was selected in scanning by demanding that

(a) there was only one track in each set of chambers,

(b) the track in the range chambers stopped inside the stack, and

(c) both tracks originated from the target.

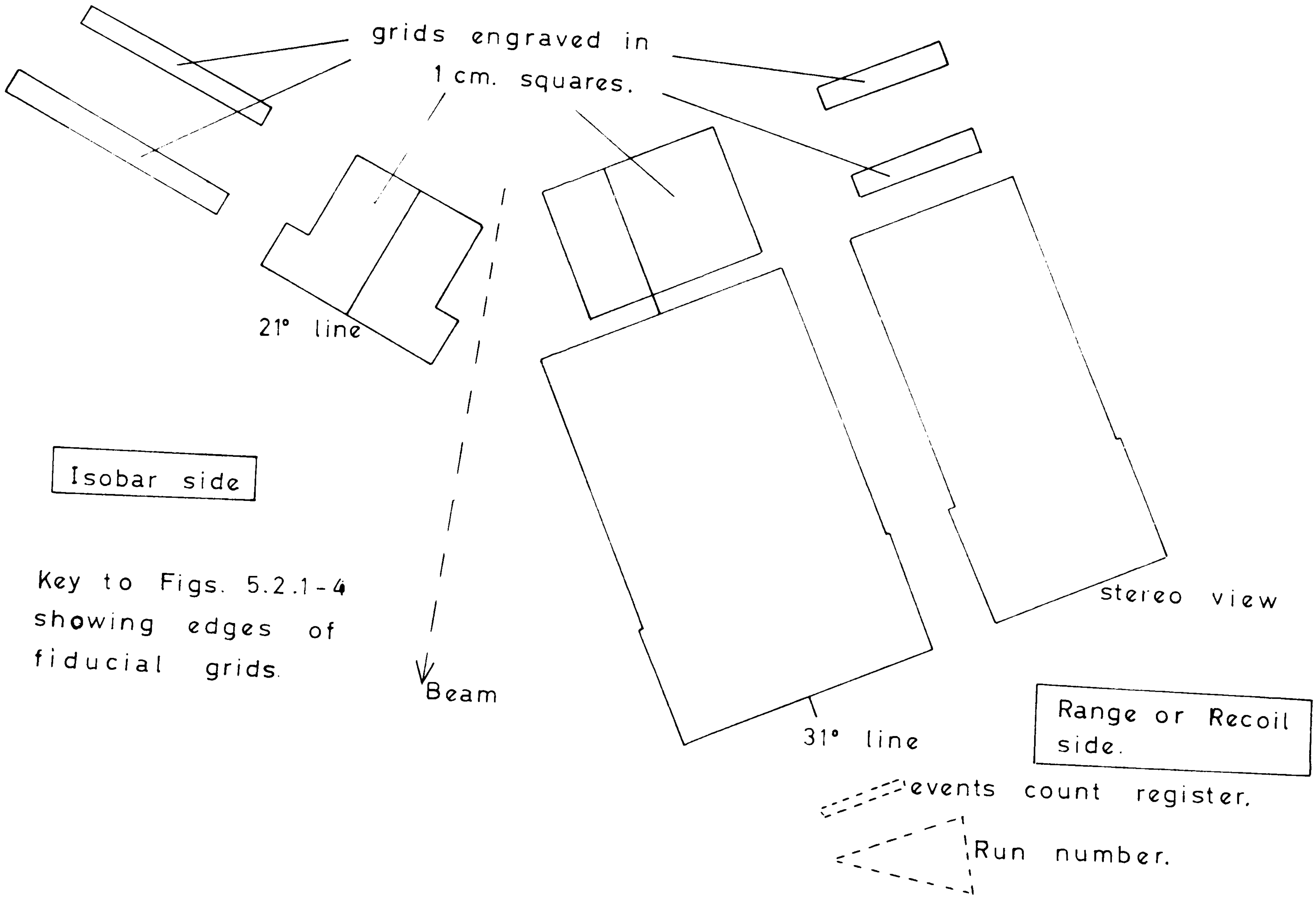

Key to Figs. 5.2.1-4
showing edges of
fiducial grids.

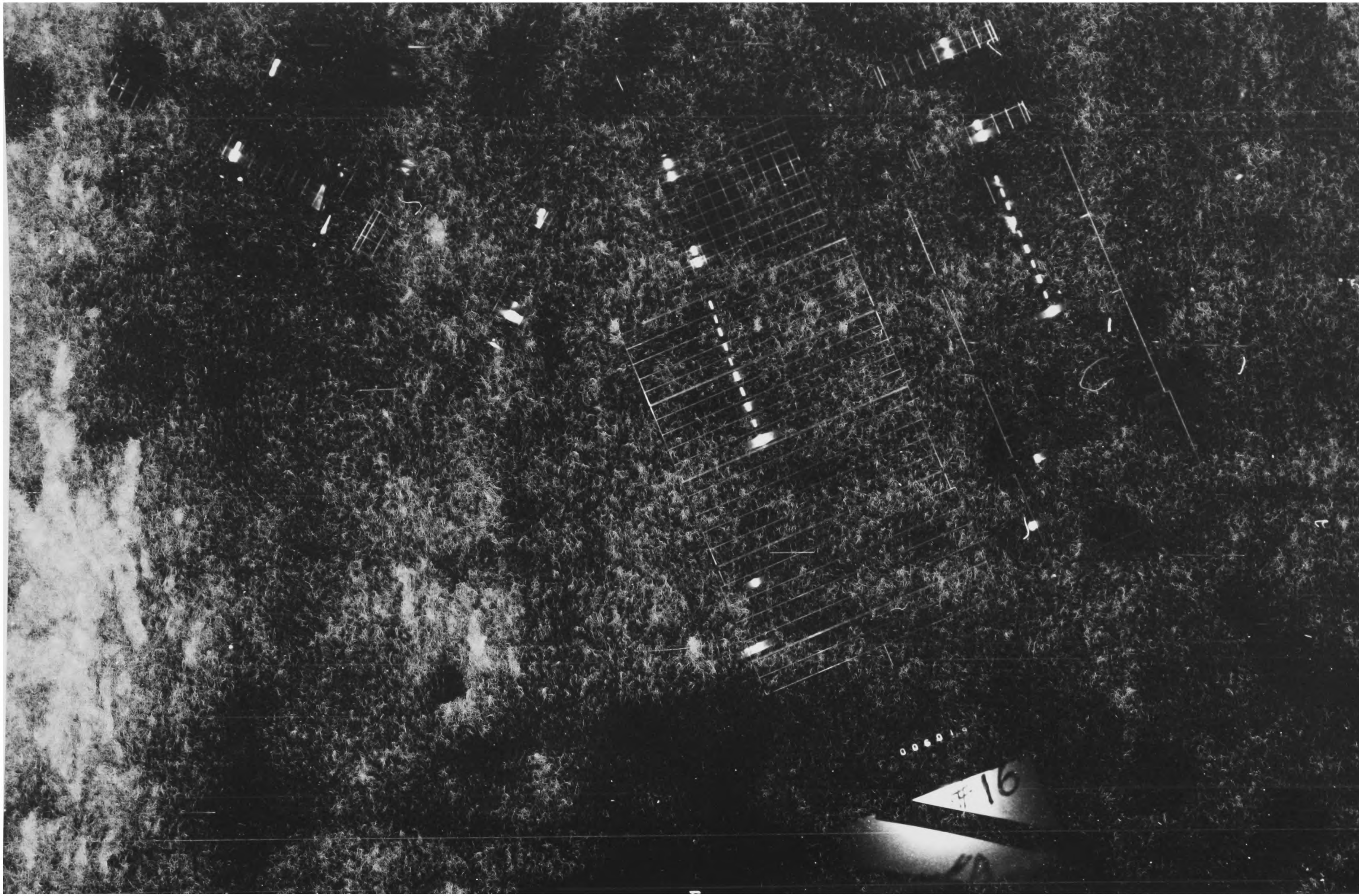

Figure 5.2.1

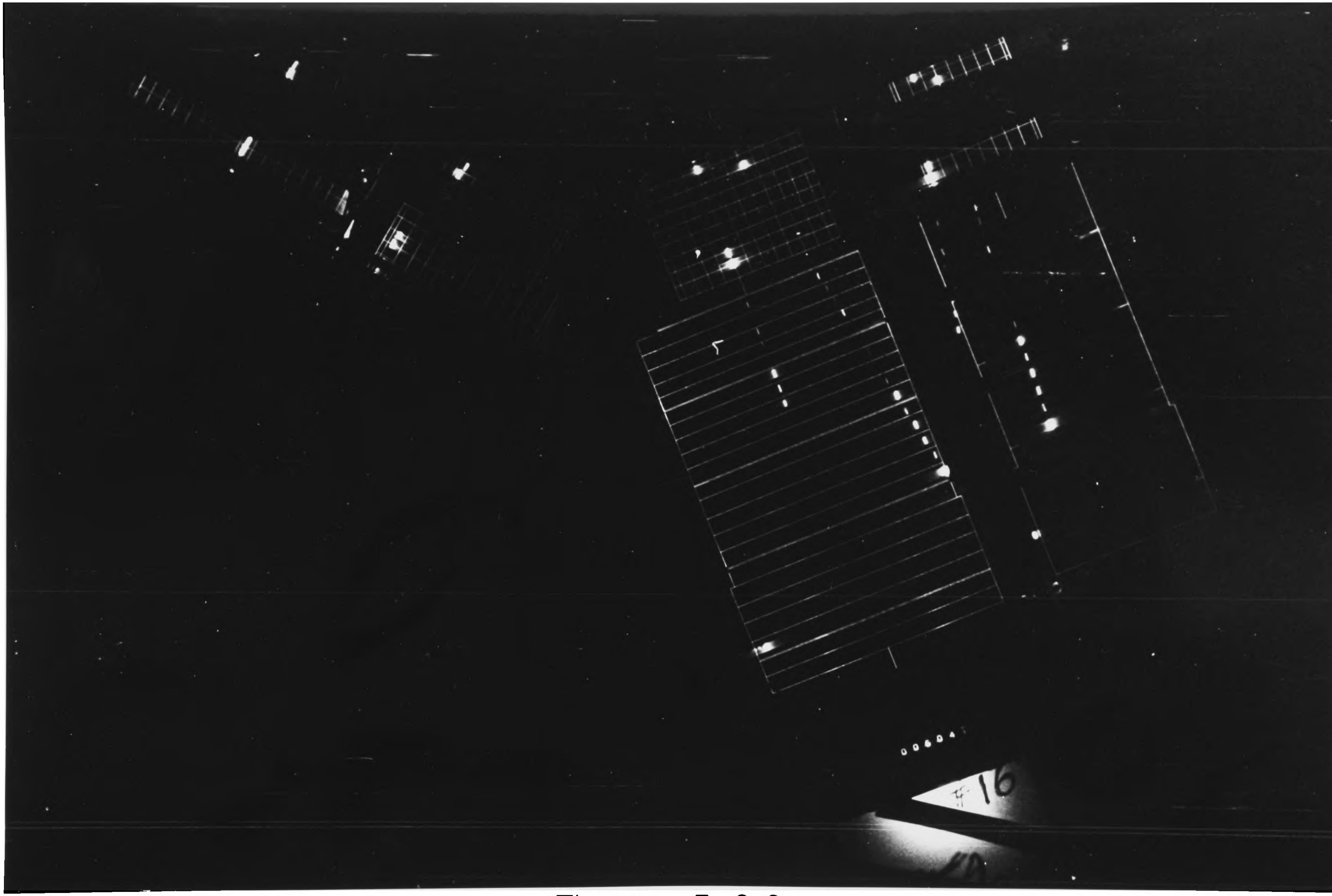

Figure 5.2.2

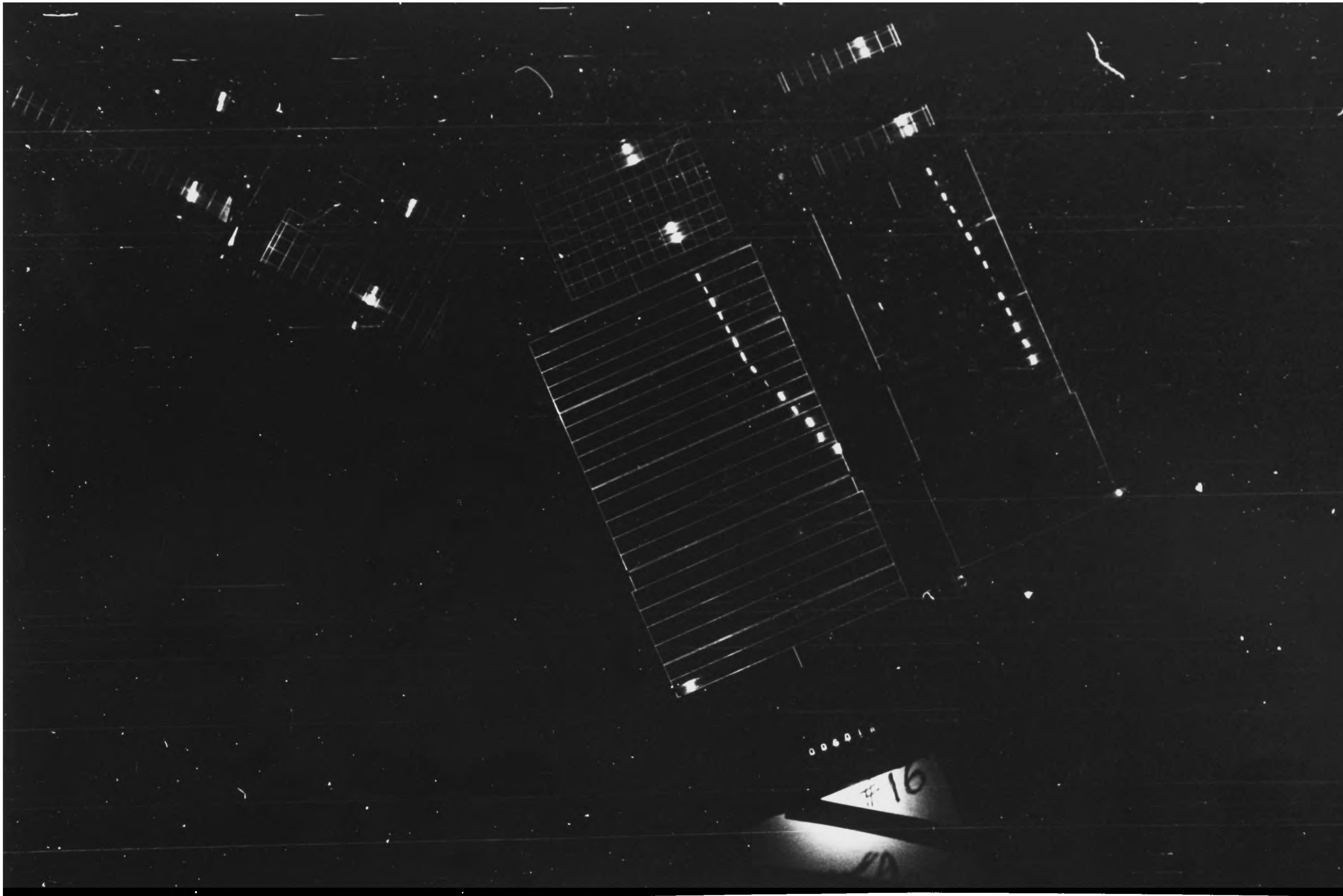

Figure 5.2.3

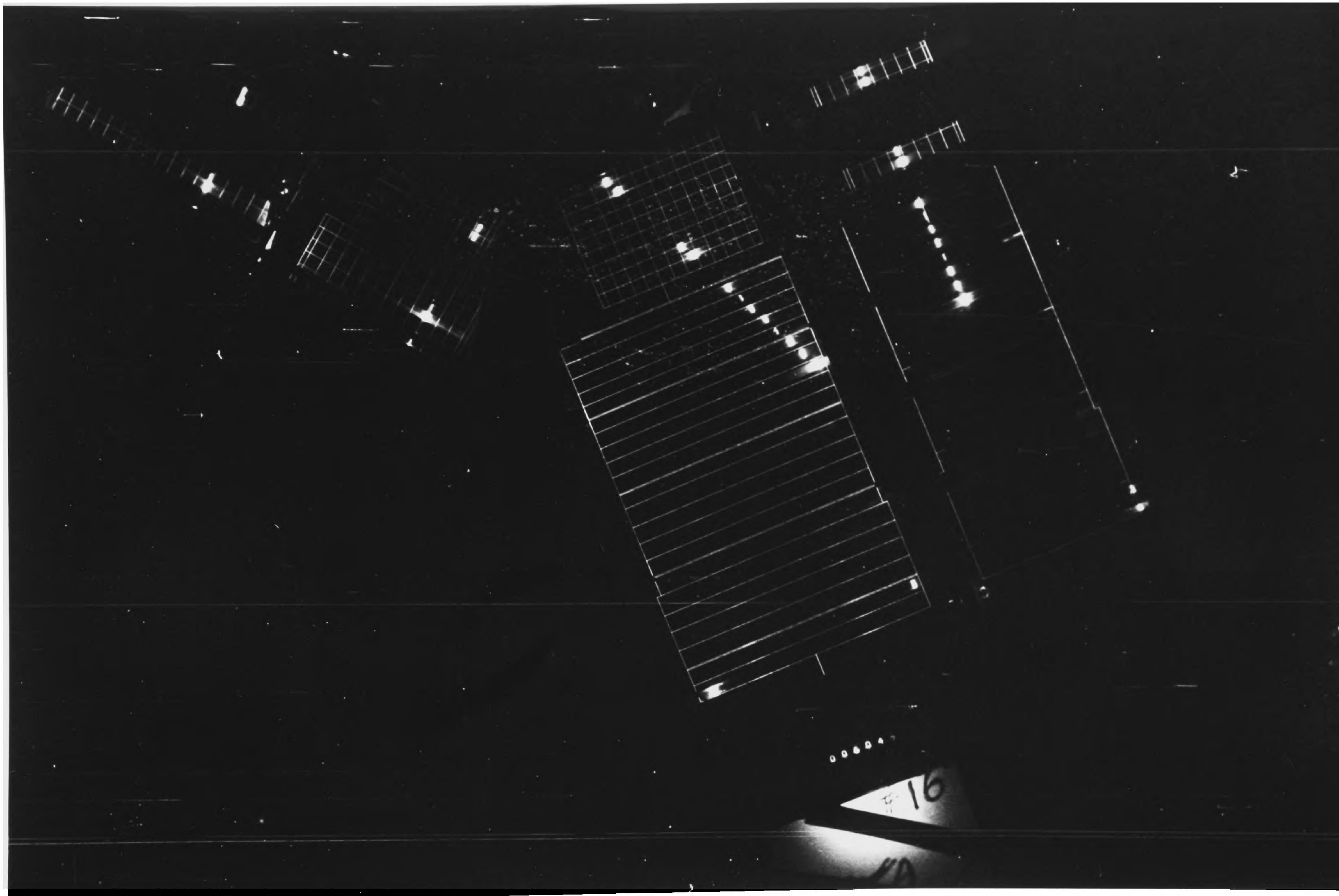

Figure 5.2.4

A frame satisfying these requirements was measured by recording on paper tape via the typewriter the number of range chambers traversed and then measuring the positions of the

(i) 31° fiducial line ('range' side),

(ii) direct view of track in 'range' direction chambers,

(iii) stereo view of track in 'range' direction chambers,

(iv) 21° fiducial line ('isobar' side),

(v) direct view of track in 'isobar' chambers,

(vi) stereo view of track in 'isobar' chambers,

recording them on paper tape.

Measuring the tracks entailed making a best fit by eye with the straight line on the cursor to the line defined by the four sparks in the direction defining chambers. The width of the sparks and the relatively short length of track in the two pairs of angle measuring chambers on each side meant that there was an error of about $\pm$ 10 units ($\sim\frac{1}{2}^{\circ}$) in measuring angles and about $\pm$ 2 units in r (figures obtained by measuring the same track 100 times, and repeating this at different times for 10 different tracks). It would perhaps have been more accurate but would have involved more computing if the position of each spark had been measured and a line found by least squares fitting.

A much more serious cause of inaccuracy was distortion on the film, caused by imperfect experimental optics. The magnification was less at the edges of the film than at the centre so that, for example, the angle between the 21° line and the 31° line was 50.5° on the film. Angles were corrected relative to the 21° or 31° lines when it came to computing the event (i.e. all measured angular differences were multiplied by 52/50.5). The error on a track measurement from this source alone would be ~ 0.2° (i.e. ~ 1%), less than the error in setting on the track.

All frames were categorised. To each category there corresponded a number which was recorded on the paper tape. Apart from possible good events other categories catered for frames

(i) with two tracks in one or both sets of chambers (Fig. 5.2.2) at least one of which would satisfy the requirements of a possible good event,

(ii) with a scatter in the recoil stack so that the particle left the chamber (Fig. 5.2.3),

(iii) in which the interaction point lay outside the target (usually in the exit window in the target outer vessel) (Fig. 5.2.4),

(iv) in which there were no discernible tracks or in which there was any other rubbish such as tracks which could have originated from a collision in the lead wall in front of the target,

(v) which overlapped (caused by the camera failing to wind on correctly).

None of these frames could be measured.

Double tracks in a chamber resulted from the combination of the long sensitive time of the chambers (not measured but ~ 500 nsecs), the short mean time between particles (~ 10 nsecs) and the delay in firing the chambers (~200 nsecs). The probability of any pp interaction in the target alone was $\sim 3.10^{-3}$ so in 200 nsecs there would be ~ 0.05 interactions. If it is assumed that about one half of these have at least one product detectable by the spark chamber system ~ 1/40 of all frames would show two tracks in one or other of the dhambers. The actual figure was higher, at 1/12, doubtless due to the "bunching" of the beam decreasing the effective mean time between protons. These frames need to be considered when evaluating cross-sections since they are a sample of all possibly good events.

Every ten events or so during scanning the frame number was typed onto the paper tape so that the computer could check its frame by frame counting.

5.3 Computer Analysis

I. Geometric Reconstruction

The computer used in the initial analysis was the Ferranti Mercury at Oxford. This was programmed to read in the output tape from the scanning machine frame by frame, counting the total number of frames and histogramming in each category as it went along. When it had read in a possible good event it reconstructed the track measurements as lines in a plane and found the point of intersection of

(a) the 21° and 31° fiducial lines,

(b) the direct view tracks in each set of chambers, and

(c) the stereo view tracks in each set of chambers,

correcting the angles as previously mentioned.

If the target were in the correct position (a) would, within measuring errors, be its centre while the displacement of (b) from (a) would give the horizontal co-ordinates of the interaction points The vertical position of the interaction point is related to (c) by an additive constant obtainable from the separation of the stereo and direct view centre lines on the film.

A run with this geometry programme alone established the distribution of interaction points relative to (a). This showed that interactions occurring in the target could be readily separated from those occurring in the radiation shield or beam exit window (most of which would have been rejected on scanning) and allowed limits to be set on the position of the reconstructed interaction point. These limits were then incorporated into the full analysis programme and a possible good event had to have its interaction point within these limits if any kinematical reconstruction was to be made.

The horizontal distribution of interaction points along and perpendicular to the beam direction is shown in <u>Figs. 5.3.1. and 5.3.2</u>. The distribution for the target

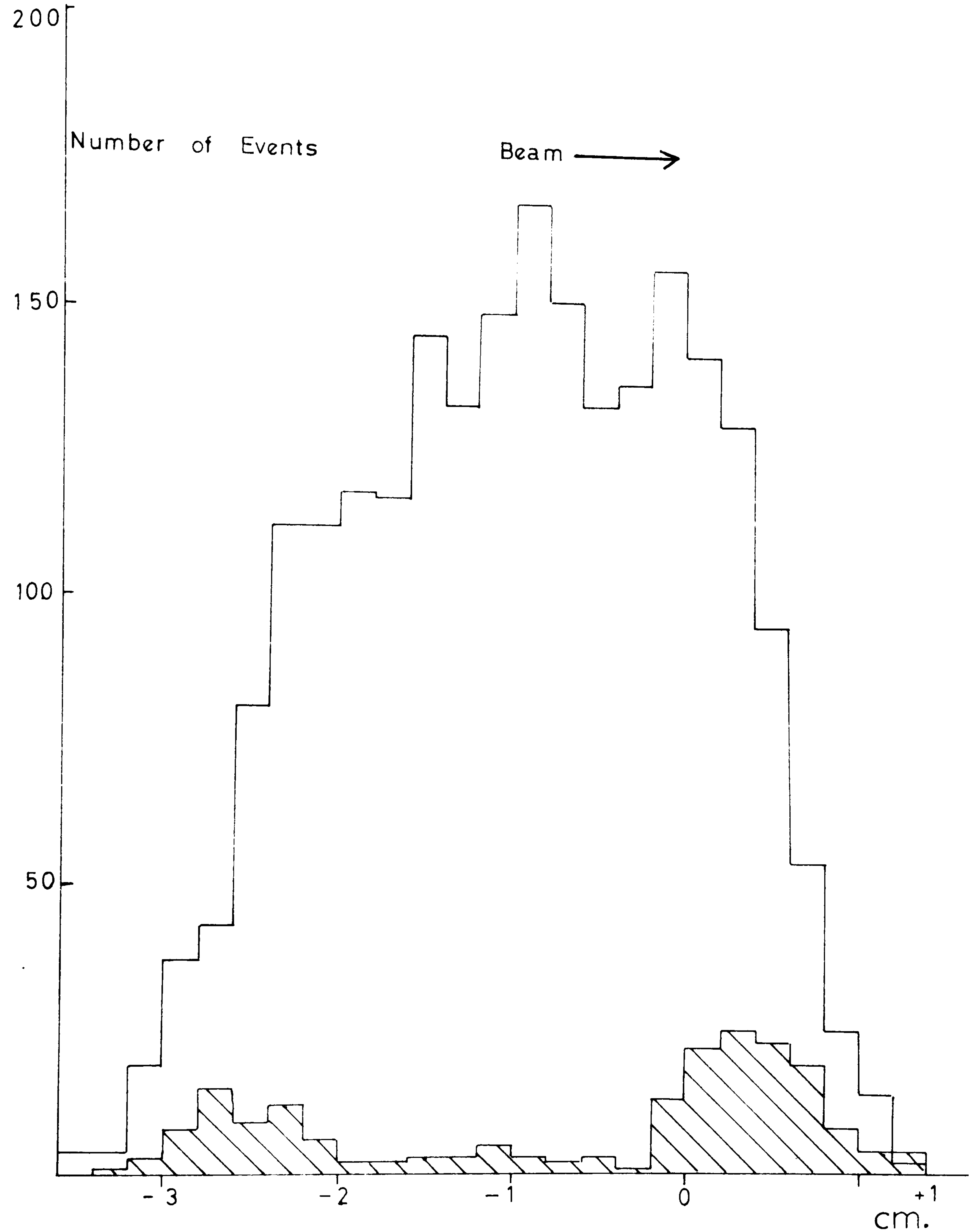

Figure 5.3.1

Horizontal distribution of interaction points in target, along beam line, relative to supposed target centre. Target empty events shown shaded.

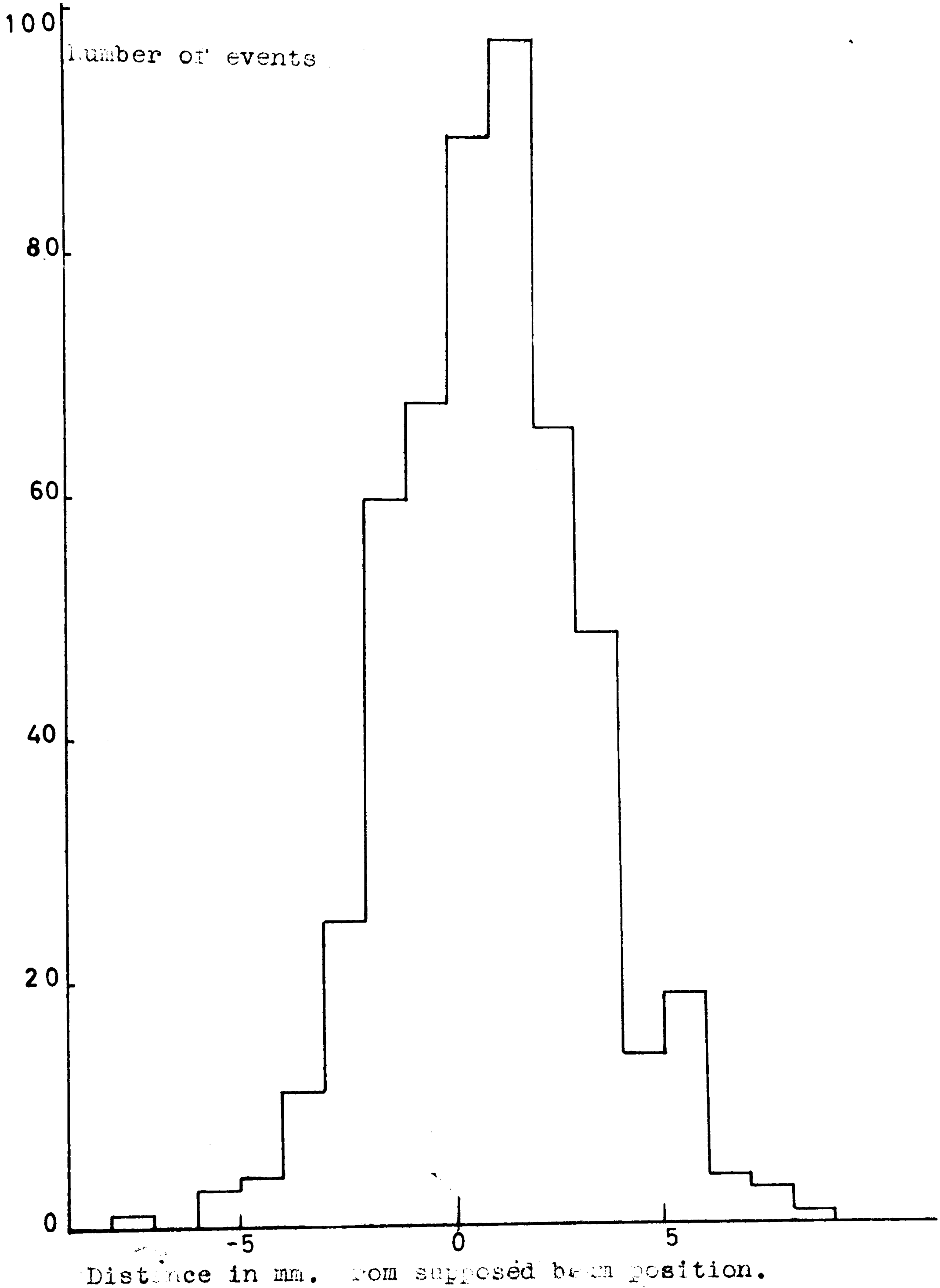

Figure 5.3.2

Horizontal distribution perpendicular to the beam of interaction points in the target. The beam direction is out of the paper.

empty events shows two peaks corresponding to the target walls. The separation between the two peaks is consistent, within the 2% uncertainty in measuring the overall magnification, with 3.175 cm or 1.25", the target width. The target centre seems to be displaced 1.1 cm nearer the synchrotron and the beam seems to be 0.1 cm to one side of the nominal beam line. This point will be returned to when geometric efficiencies are discussed.

II Kinematical Reconstruction

In the kinematical reconstruction the kinetic energy of the proton stopping in the range chambers was taken to be that of a normally incident proton stopping half-way through the relevant piece of aluminium absorber. Unless the proton interacted along its path this results in a maximum error of $\pm$ 3.6 MeV. Δ^2, the square of the four momentum transfer, is given by 2mT, where T is the kinetic energy.

The reconstruction was made on the assumption that the event was genuinely $pp \rightarrow pp\pi^o$. The programme calculated

(a) the $p\pi^o$ invariant mass ω (for the proton not in the range chambers) and

(b) the laboratory co-ordinates (θ, ϕ) of the proton from the $p\pi^o$ combination relative to the $p\pi^o$ direction and the reaction plane. This ϕ differed from the normal azimuthal angle used in the literature, which is measured from the normal to the reaction plane. Because of the selection biases inherent in the apparatus only events with $1175\text{ MeV} \leq \omega < 1285\text{ MeV}$ were retained for further consideration. This comprised a bout 75% of all possible good events.

The angle θ in (b) above is limited by kinematics to lie within the cone $0 \leq \theta \leq \theta_m$ (see Fig. 3.2) where θ_m, the maximum cone angle, is a function of ω and Δ^2. It was found that the ratio θ/θ_m was greater than unity for about 10% of the events. This could be due to

(i) measuring inaccuracy plus the uncertainty in the proton kinetic energy, or

(ii) background events, possibly $pp \rightarrow pn\pi^+$.

The distribution in θ/θ_m for target full events is shown in Fig. 5.3.3. The target empty distribution had relatively more events with $\theta > \theta_m$. It can be seen from the distribution that the majority of events with $\theta/\theta_m > 1$ have $\theta/\theta_m < 1.3$: it is plausible that most of these events had been badly measured or that the energy or angle of the stopping proton was inaccurate (due to an interaction or to multiple scattering in the target). The distribution of interaction points for these events was, within statistics, the same as that for all events.

After the kinematical reconstruction events were histogrammed in 10 MeV bins in ω and 7 MeV bins in T. The resultant distributions are summarised in Figs. 5.3.4, 5.3.5, 5.3.6, 5.3.7. Calling events with $\theta > \theta_m + 2^\circ$ background

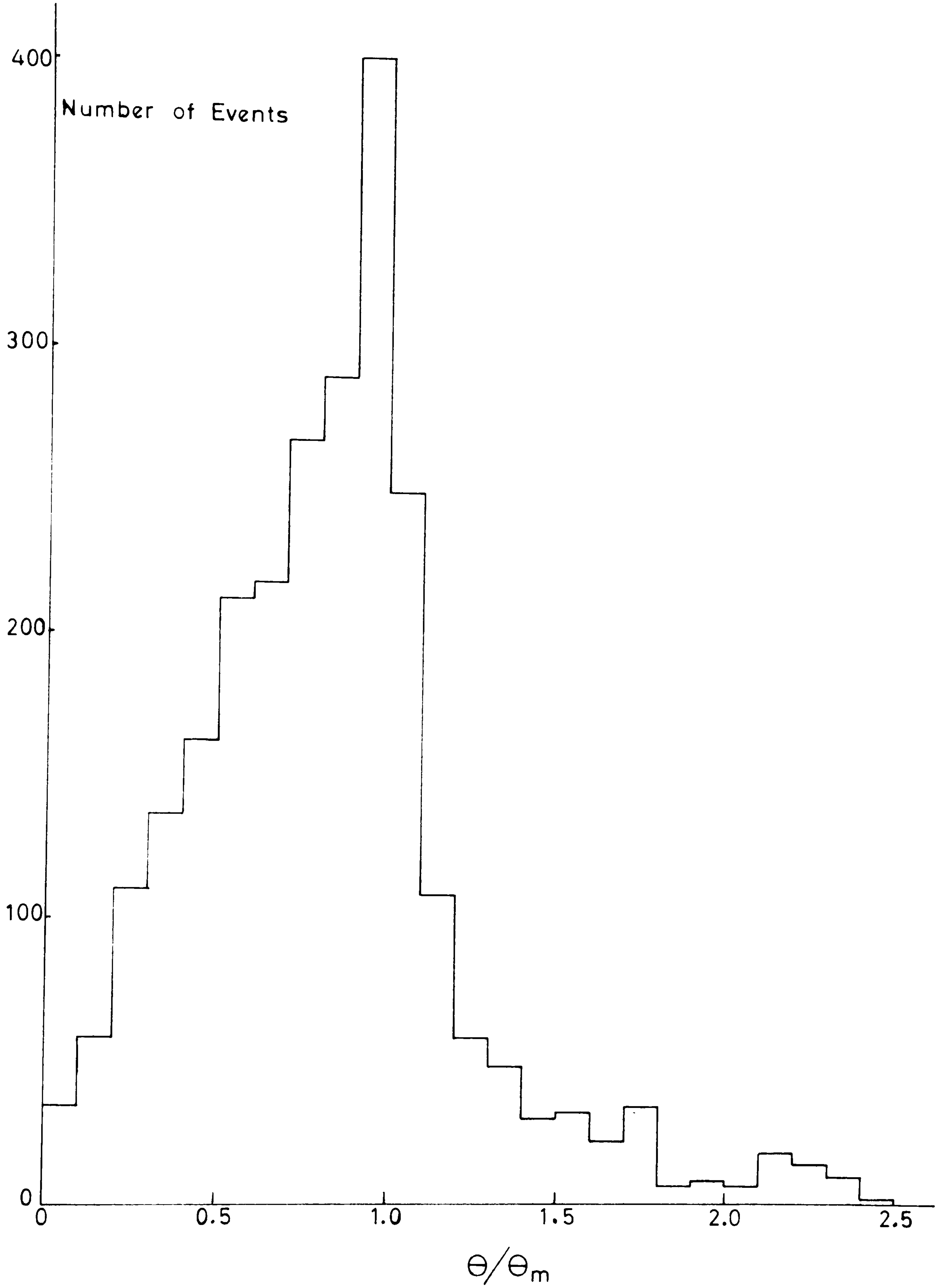

Figure 5.3.3

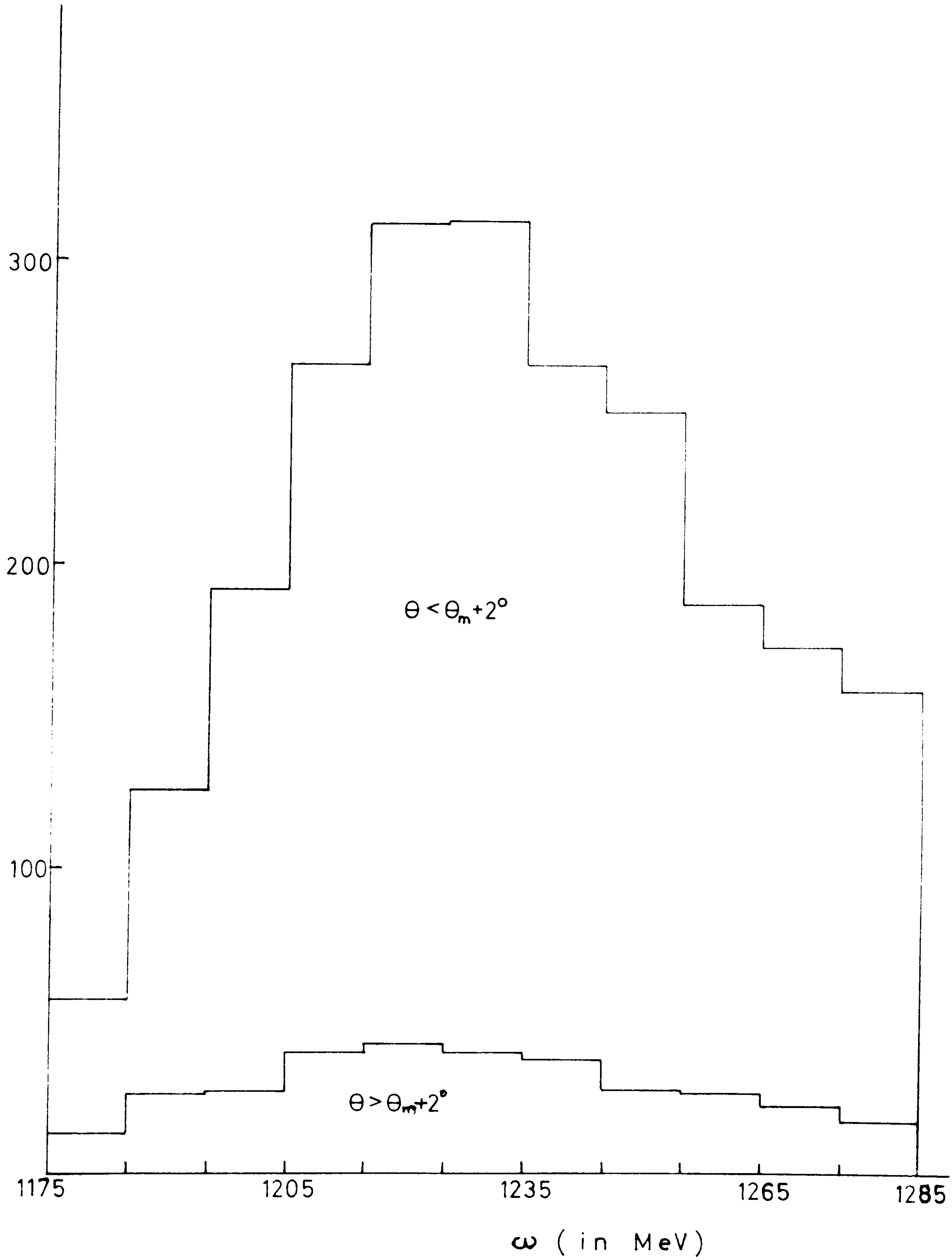

Figure 5.3.4

Uncorrected Distributions – Target Full

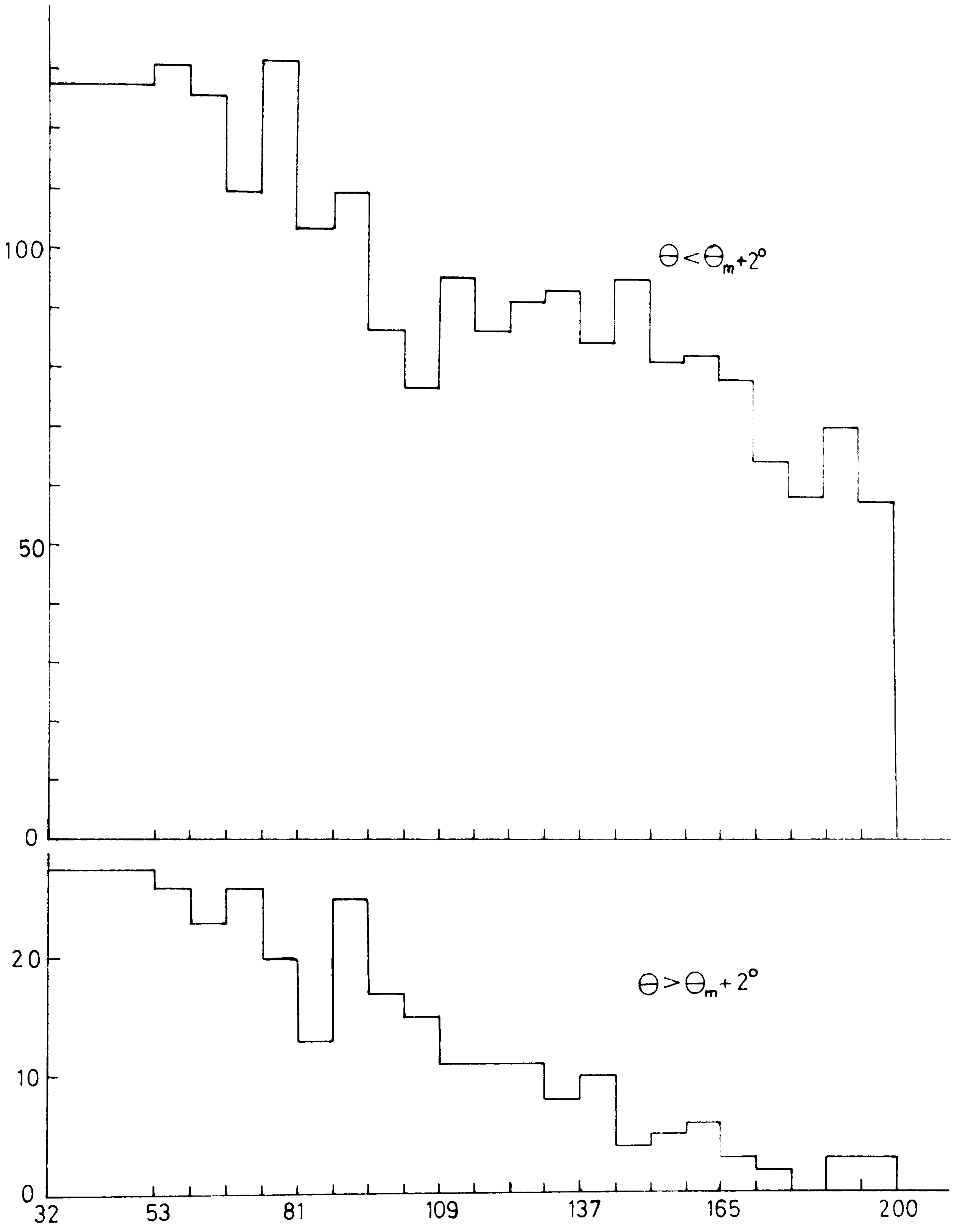

Uncorrected Distributions — Target Full

Figure 5.3.5

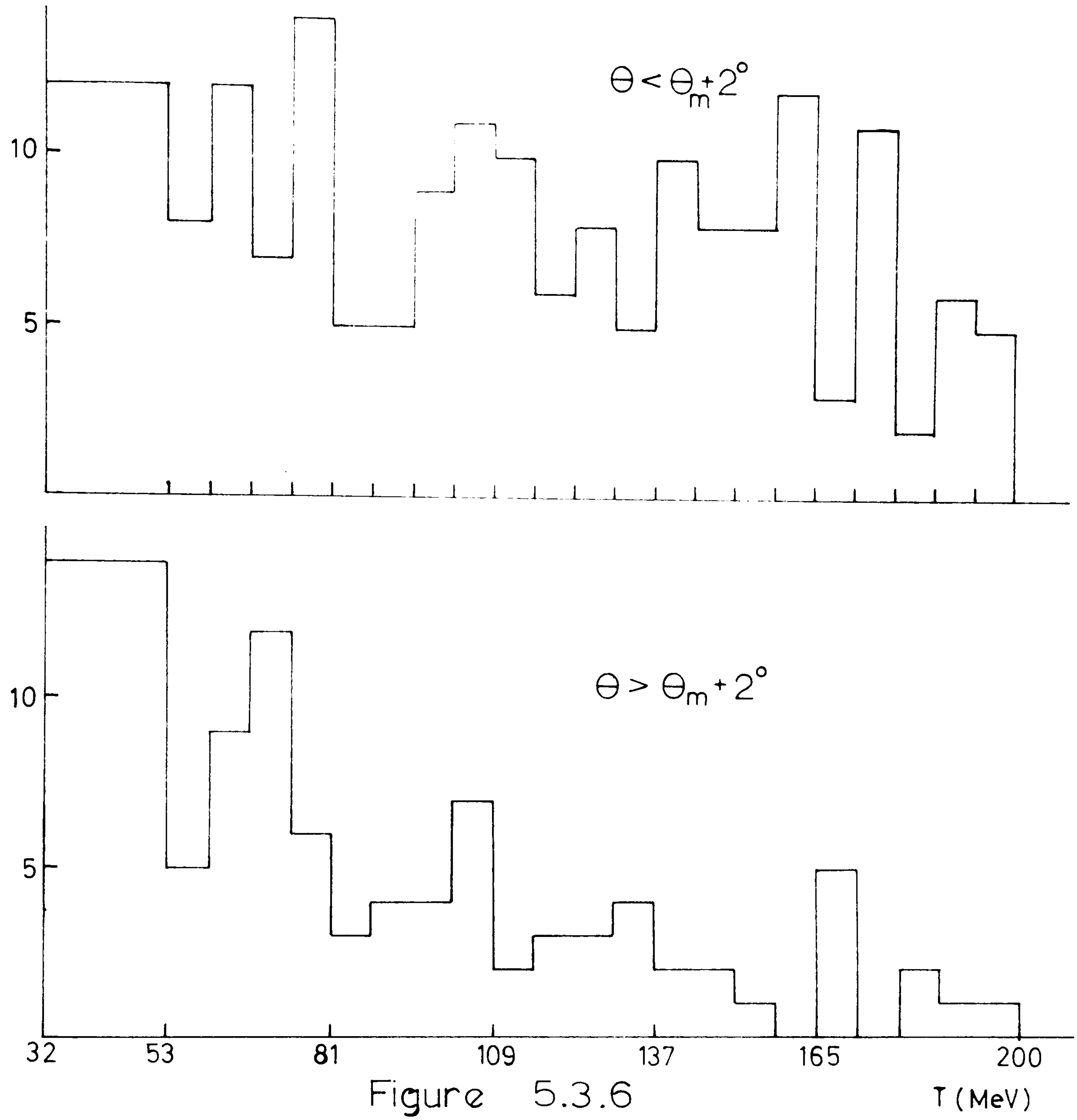

Figure 5.3.6

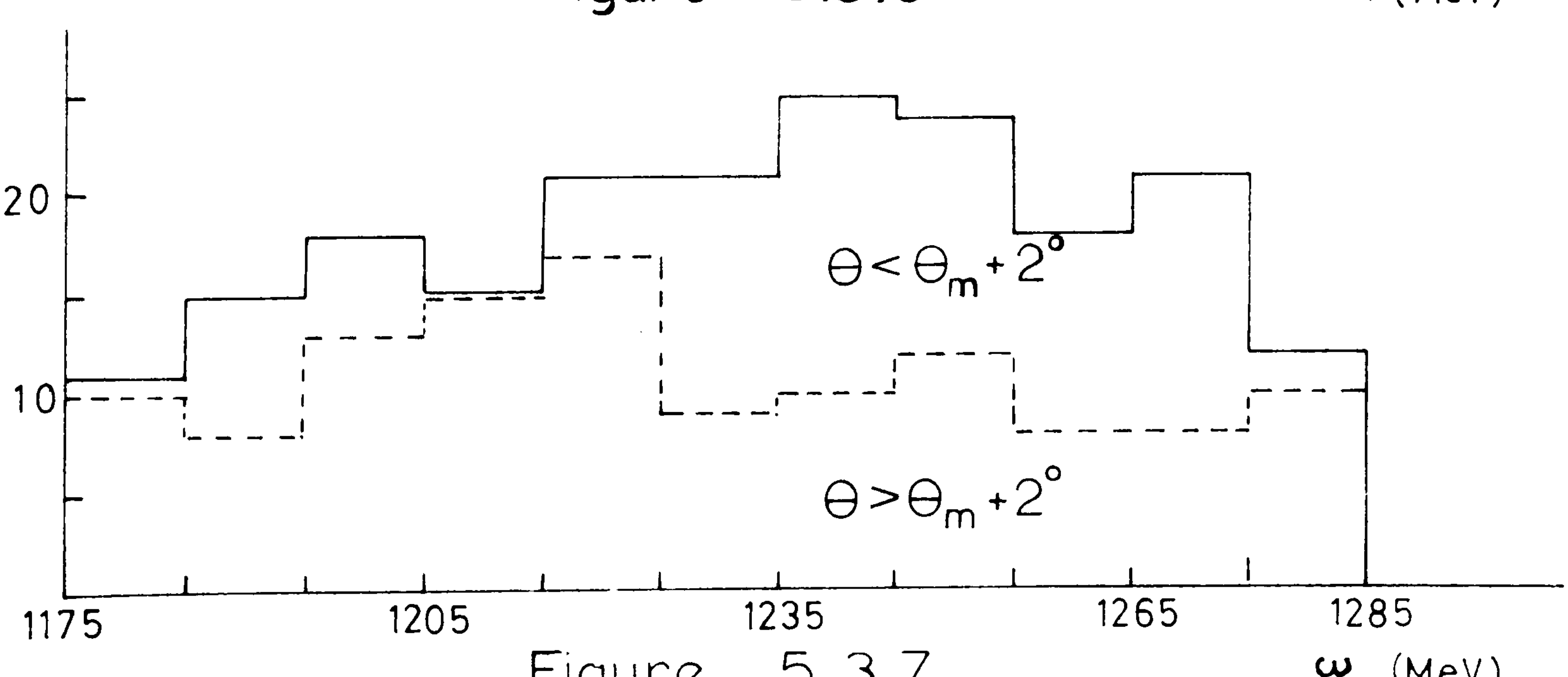

Figure 5.3.7

Uncorrected Distributions — Target Empty events (the other source of background, the target walls, is removed by the target empty subtraction) it is noticeable that the lower ω values are enhanced in the background events and the distribution in T for background events falls off much more sharply than for good events. Both these effects are statistically significant, the actual ratios being

	$\theta < \theta_m + 2$	$\theta \geqslant \theta_m + 2$
$\dfrac{\omega < 1225 \text{ MeV}}{\omega \geqslant 1225 \text{ MeV}}$	0.71 ± 0.04	0.86 ± 0.11
$\dfrac{T < 95 \text{ MeV}}{T \geqslant 95 \text{ MeV}}$	0.91 ± 0.04	1.97 ± 0.12

A rescan of a sample of 74 background events showed that approximately

35% had perfectly good tracks in both chambers,

30% had a poor track in the isobar chambers, often with one or two sparks displaced, and

35% showed a track in the range chambers with a large scatter at some point.

The 35% with perfectly good tracks could be made up of (a) badly measured events, (b) interaction in the target walls, where the Fermi momentum of the target proton would alter the kinematics from those of a free proton, and (c) events of the type $pp \rightarrow pn\pi^+$ where the π^+ entered the range chambers. To have done this it must have had an energy low enough for there to have been a reasonable probability of satisfying the discrimination requirements on C1 and C2 (see 4.2.2). This implies an energy ~ 100 MeV so the distribution in T should strongly favour the lower T values. An event with low π^+ energy has a large π^+p opening angle so that the π^+ would be at a large angle to the beam, favouring low values of ω when the event was interpreted as $pp \rightarrow pp\pi^0$. This is entirely in accordance with the observed ω, T distribution.

Events of the same type in which the π^+ entered and failed to give a signal in the Čerenkov counter can be ignored since the proton from such an event would have an energy greater than 200 MeV and would have been rejected by C3.

The relatively greater proportion of 'outside cone' events in the target empty data (37% as opposed to 14%) supports the supposition that many of these background events resulted from target wall interaction. These are removed by the "target full" - "target empty" subtraction.

Those 30% of background events with poor isobar tracks could be events in which the isobar track was not related to the track in the range chambers but came from a more recent interaction and had suppressed the true isobar track, suffering some damage itself in the process. Such a spurious track has more chance of being outside the computed cone if the cone angle is small and the cone axis is near the beam, exactly those conditions satisfied by events with small ω, T (see <u>Figs. 3.2 and 3.3</u>).

The isobar chambers had a marginally poorer performance than the range chambers, due to edge breakdowns, and this would help the "robbing" of tracks postulated above. It would also affect some genuine tracks by making them difficult to measure, and so would contribute to the background events.

Those events which showed a strong scatter in the aluminium of the range chambers would presumably consist of elastic and inelastic proton-aluminium collisions. The cross-section for such a collision at a proton energy of 100 MeV is ~ 600 mb, so the probability that a proton would interact somewhere in the stack of absorber plates was ~1/30, in agreement with the observed figure of ~ 1/40. For these events the value of T would be too low. This has the effect in most cases of making the computed value of ω too high; Fig. 3.1 shows that this will be most severe when $\omega \sim 1215$ MeV and $T > 100$ MeV.

It can therefore be concluded that about 50%, certainly no more, of the background events are truly background events caused by

a) target wall interactions,

b) $pp \rightarrow pn\pi^+$

c) "robbing" of tracks in the isobar chambers,

while the remainder were poorly measured and wrongly binned good events.

III Geometric Detection Efficiency

The detection efficiency on the "range" side for an event of a given kinematical configuration (ω, Δ^2) depended on the position of the interaction point in the target. The mean detection efficiency was obtained by integrating across the beam profile and along the beam path through the target. To do this the beam was assumed to be of zero width (this does not affect things much as it was ~ 3 mm wide) and 1.5 cm high. The position of the target relative to the counters and spark chambers was also needed.

Detection efficiency on the isobar side could only be calculated if the angular distribution of the "isobar" proton was known. Since the attempt to extract this angular distribution failed (see Chapter 6) a geometrical cut-off on events was used to obtain an unbiased sample.

The distribution of interaction points in the target (figs. 5.3.1 and 5.3.2) seemed to indicate that the target was 1.1 cm behind its correct position and that the beam was displaced 0.1 cm to one side of its correct line. This latter is within the errors on the "Polaroid" exposures made during the experiment and the survey of the apparatus, but the former is not, although the actual target position was not checked. Since the geometric reconstruction was made relative to the 21° and 31° fiducial lines distortions on the film could only have the effect of broadening the distributions and this, plus measuring accuracy, explains the 0.6 cm measured beam width as compared to the 0.3 cm obtained from 'Polaroid' exposures.

By this stage in the analysis the apparatus had been dismantled and returned to Oxford. However, the target assembly was mounted on the experimental platform and its position checked. The result - unreliable because of the time delay and movement - was a shift of 1.3 ± 0.3 cm back along the beam direction and a sideways shift ~ 0.2 cm. This is consistent with the 1.1 cm shift from the geometric reconstruction. To produce this shift the liquid hydrogen reservoir support tubes must have been bent while the assembly was being transported. This was certainly possible.

The best estimate, therefore, of the target centre position, taking into account measuring accuracy and survey accuracy, was 1.1 ± 0.2 cm behind the point of intersection of the 21° and 31° fiducial lines. The beam direction was 0.1 ± 0.1 cm to one side of its correct line but in what follows it was taken to be along the correct line as this does not affect things appreciably.

The relative mean detection efficiency was calculated as the average, over bins of 10 MeV in ω and 7 MeV in T, of the azimuthal angle about the beam direction for which the recoil proton would have been detected. In this, the major limiting factor was C2, then the spark chambers. The calculation also showed whether half $(\frac{\pi}{2} \leqslant \phi \leqslant \frac{3\pi}{2})$ the cone in which the 'isobar' proton should be was covered by C4 and the isobar chambers (ϕ is the angle defined on page 5. 8) for all possible angles between the reaction plane and the horizontal. Only events within this half of the cone were accepted in the later stages of the analysis.

The solid angles subtended at the target by the cone of half-angle $\theta_m + 2^\circ$, and by that region of C4 for which $\pi/2 \leq \phi \leq 3\pi/2$ (i.e. the solid angle available for background events) were also calculated, to be used later when allowing for background events.

IV Corrected Histograms

The output tape of the geometric and kinematic analysis programme containing information on 2626 target full and 324 target empty events was used as data for another programme, run on the Atlas computer at the Rutherford Laboratory, which produced corrected bin populations for both target full and target empty data.

To eliminate isobar proton detection biasses this programme selected events with $\pi/2 \leq \phi \leq 3\pi/2$ and in a ω, T bin with full coverage of half the isobar cone. These events were binned in the same 10 MeV bins in ω and 7 MeV bins in T as were used before. The events in each bin were subdivided according as $\theta <$ (or $\geq$) $\theta_m + 2^\circ$ and the number of events in each bin was normalised to an azimuthal detection angle of 0.400 radians. The background events were assumed to be uniformly distributed in solid angle across C4, and were subtracted after having been normalised to the 'in cone' solid angle. A bin which had n_i events with $\theta < \theta_m + 2^\circ$ and n_o outside $\theta_m + 2^\circ$ was given a corrected number of events n

$$n = \left\{ \left(n_i - n_o \frac{d\Omega_i}{d\Omega_o} \right) \right\} \frac{0.4}{\phi_i}$$

where ϕ_i was the detection azimuthal angle previously calculated and $d\Omega_i$ ($d\Omega_o$) were the 'in cone' ('out of cone') solid angles. The error on n was taken to be

$$\delta n^2 = \left\{ n_i + n_o \left(\frac{d\Omega_i}{d\Omega_o} \right)^2 \right\} \left(\frac{0.4}{\phi_i} \right)^2$$

i.e. the errors on n_i and n_o were assumed to be purely statistical.

The resulting histograms for target full and target empty, with mass bins combined to give three bins in ω (1185-1215, 1215-1245, 1245-1285 MeV), are shown in <u>Figs. 5.3.8, 5.3.9 and 5.3.10</u>. These bins were chosen to give roughly equal statistical accuracy in each bin, and to cover the ω regions below, on and above the N^{*+} resonance. In each case the uncorrected histogram of "in cone" events is given for comparison. The error flags on the corrected histograms indicate the statistical uncertainty, their large size being due to the poor statistics of 889 (76) "in cone" events and 130 (39) "outside cone" events, target full (empty). The systematic error referred to in the figures is that due to the geometric correction factor only.

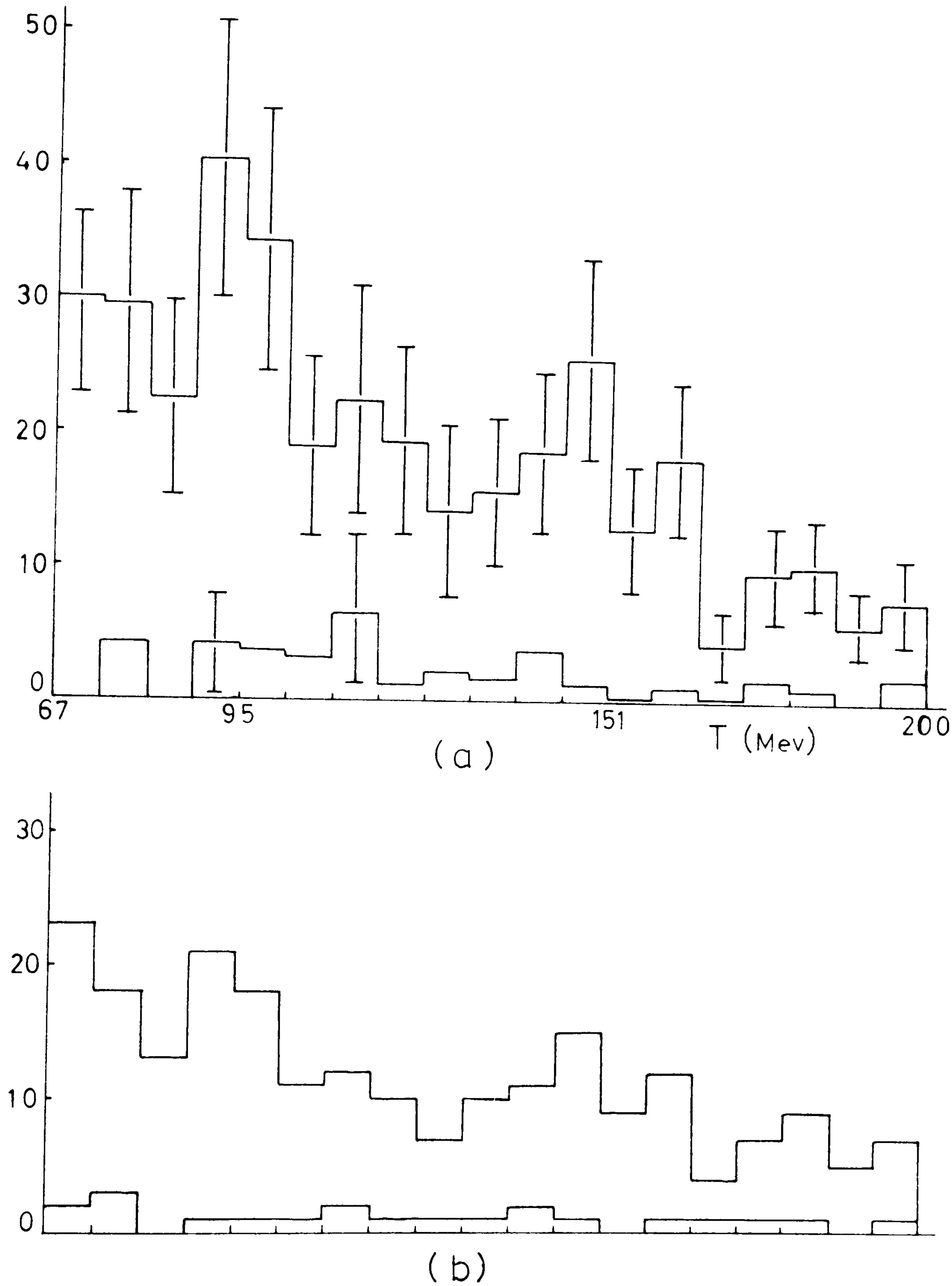

Figure 5.3.8

(a) corrected and (b) uncorrected histograms, target full and empty, $1185 \leq \omega < 1215$ MeV. Systematic error (not shown) +30%, -20%

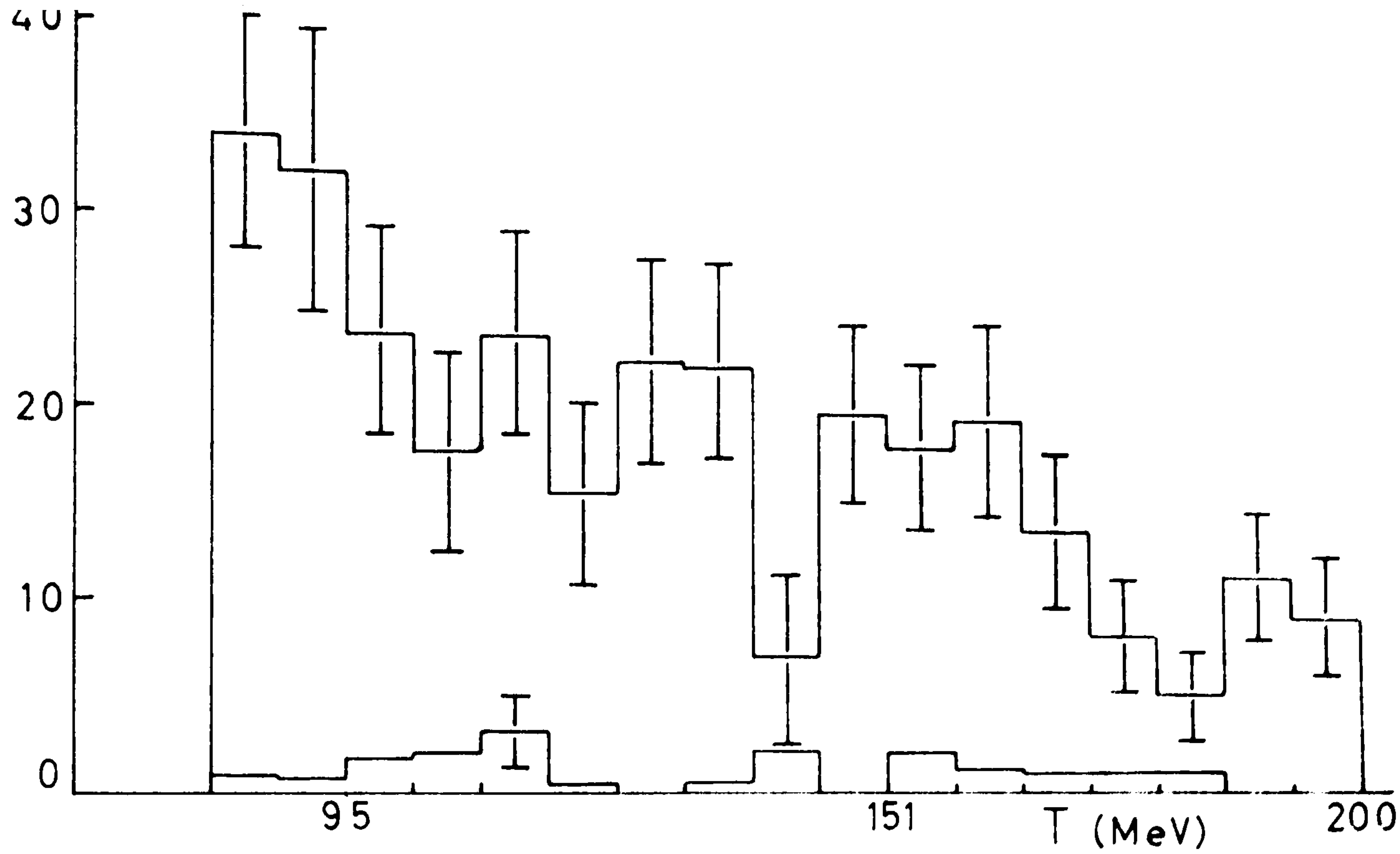

(a)

Systematic error < 2%

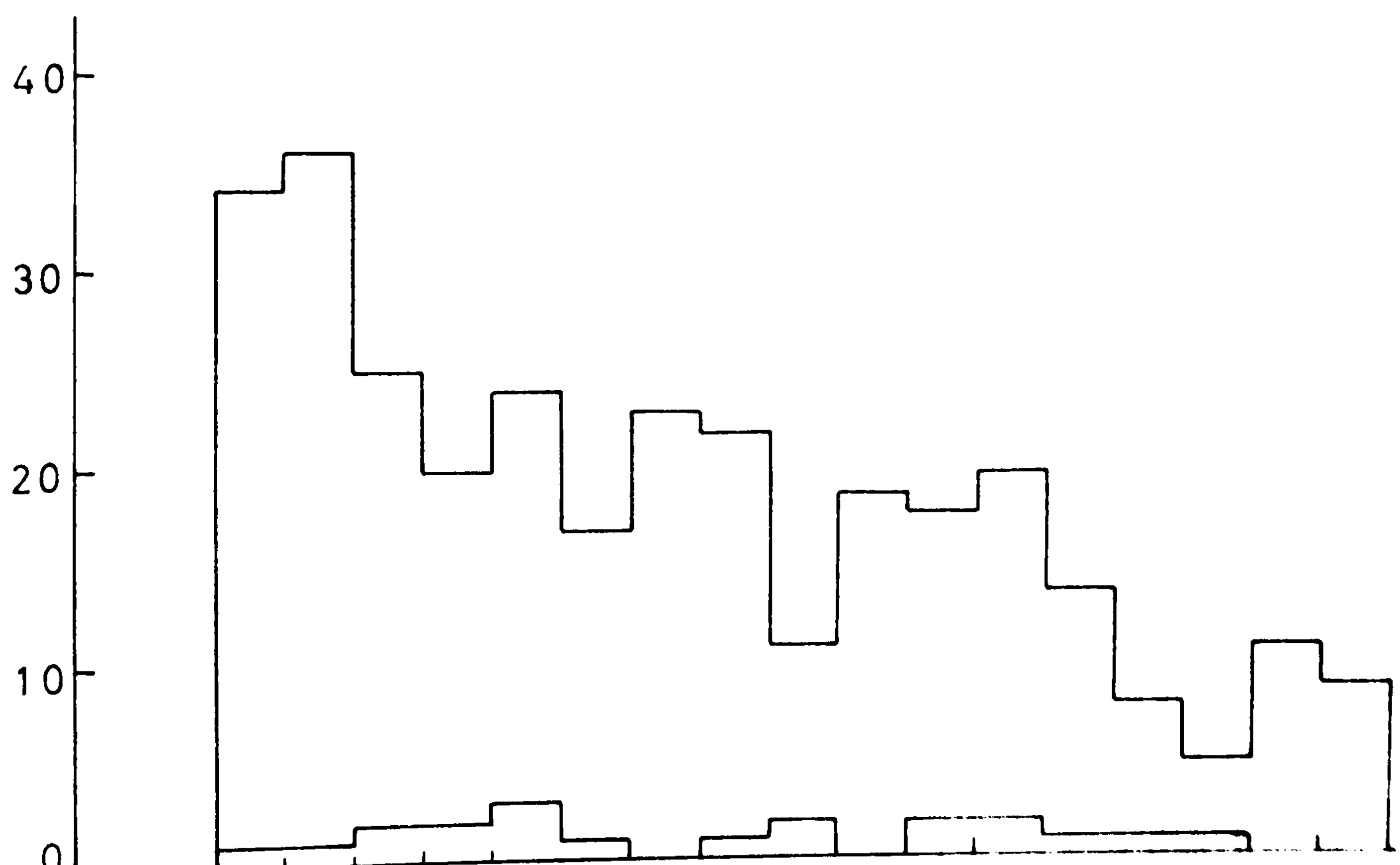

(b)

Figure 5.3.9

$1215 \leq \omega < 1245$ MeV

(as 5.3.8.)

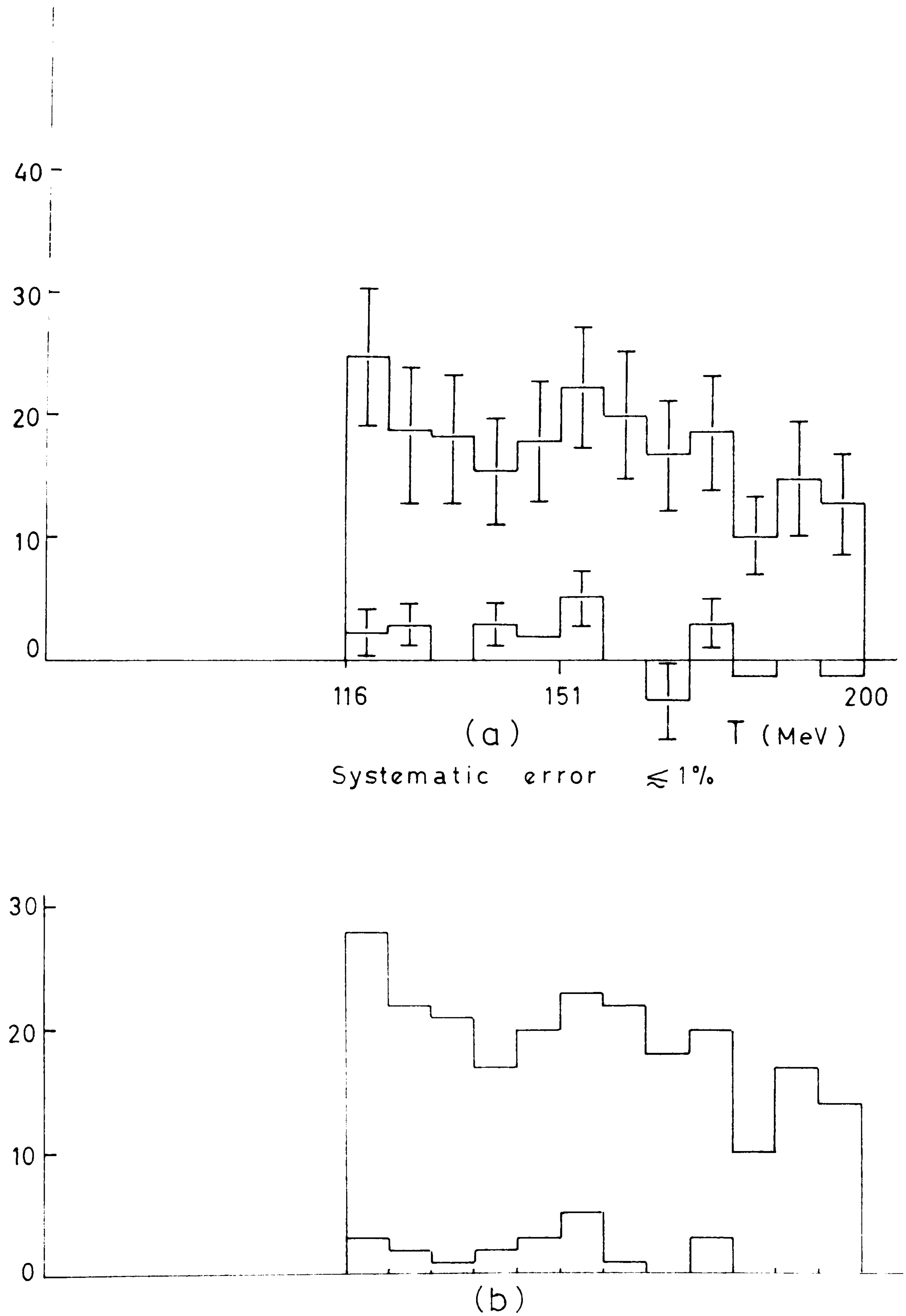

Figure 5.3.10

$1245 \leq \omega < 1285$ MeV

As the lower value of ω increases the lower limit of T for which there was 100% detection efficiency for the half-cone also increases from 67 MeV to 81 MeV to 116 MeV for the three ranges of ω.

The above method of selection and subtraction of background events needs some justification. The cone + 2° limit was set somewhat arbitrarily as being about two standard deviations in the measurement of θ (see below), so that ~ 95% of all well measured events with $\theta \simeq \theta_m$ would be within this limit. In the discussion of the source of those events with $\theta > \theta_m + 2^{\circ}$ it was concluded that ~ 50% were good events but incorrectly binned and ~ 50% were true background. Without doing large Monte Carlo calculations on the sources of background it is a fair assumption that these events were uniformly distributed in solid angle (for large θ/θ_m the distribution in θ/θ_m is gently decreasing, as would be expected if $\cos\theta/\cos\theta_m$ were approximately constant). However, those events with ω and T incorrectly assigned should be reassigned larger (but unknown) values and the bins of larger ω and T will therefore be systematically low by something of the order of 5%, but the uncertainty in this is equally large. The statistical error in these bins is ~ 50% so a 5% uncertainty is relatively unimportant.

Those background events resulting from interactions in the target walls will still be removed by the target

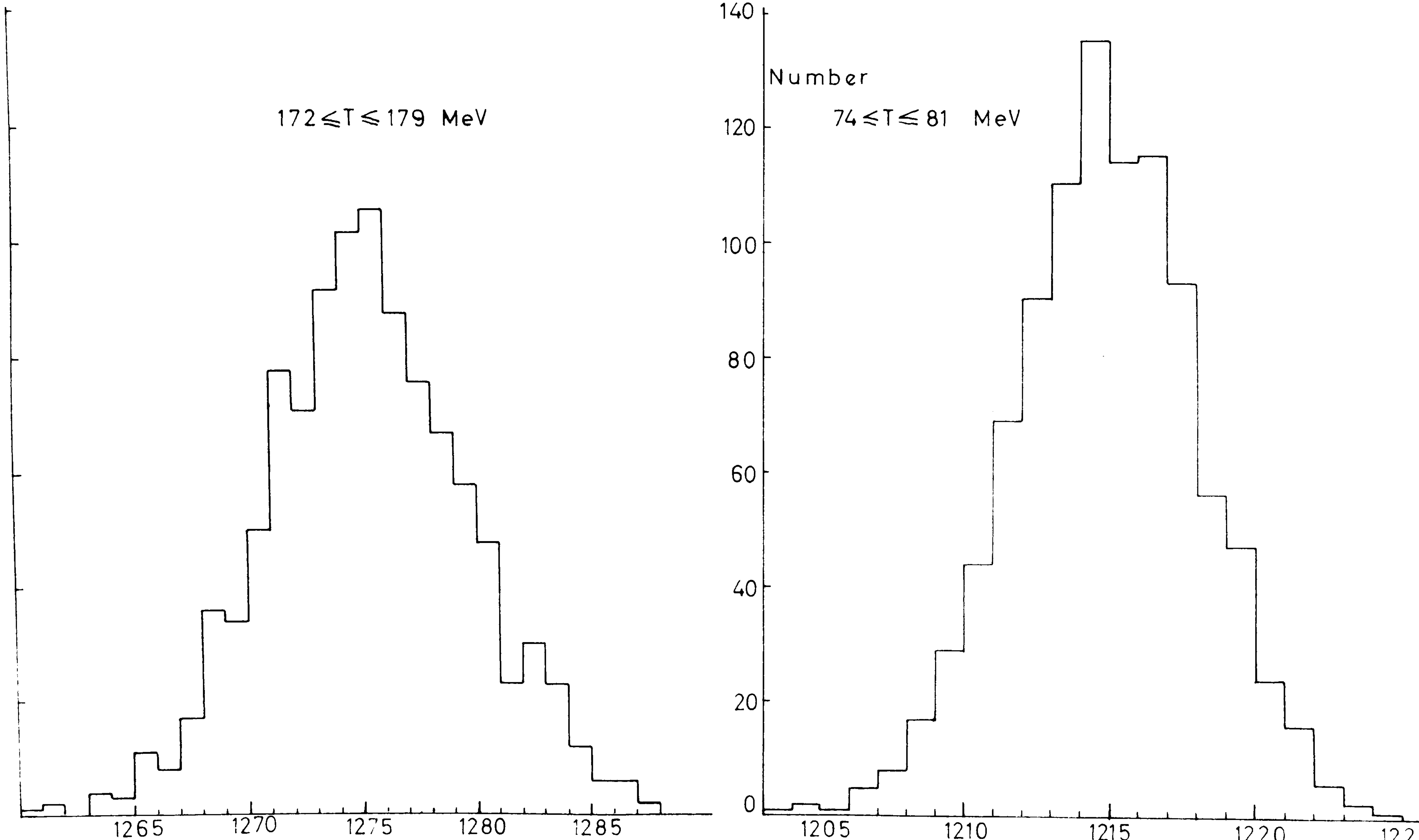

Figure 5.3.11
Monte-Carlo Distributions — ω Resolution.

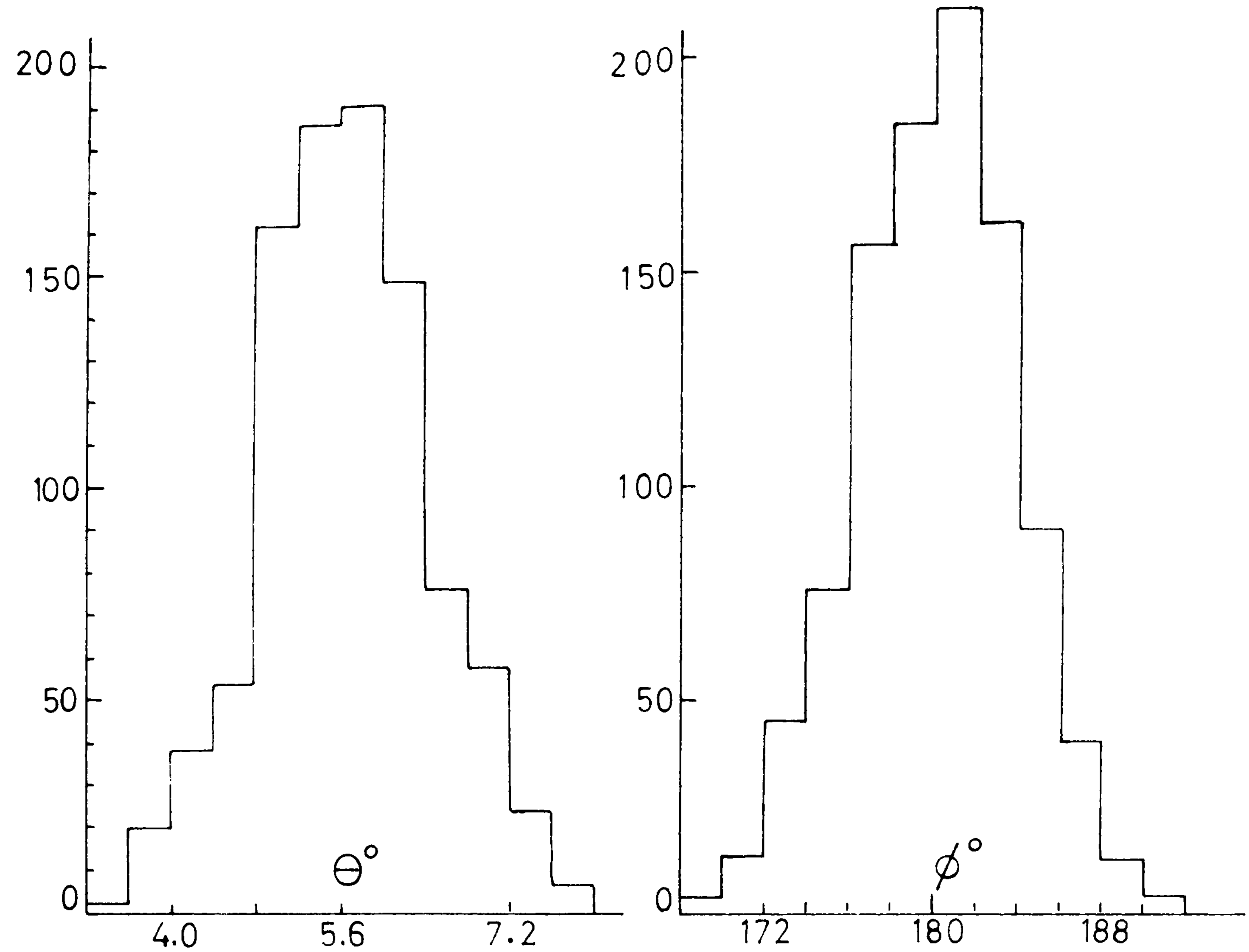

Figure 5.3.12 $74 \leqslant T \leqslant 81$ MeV
$\overline{\omega} = 1215$ MeV

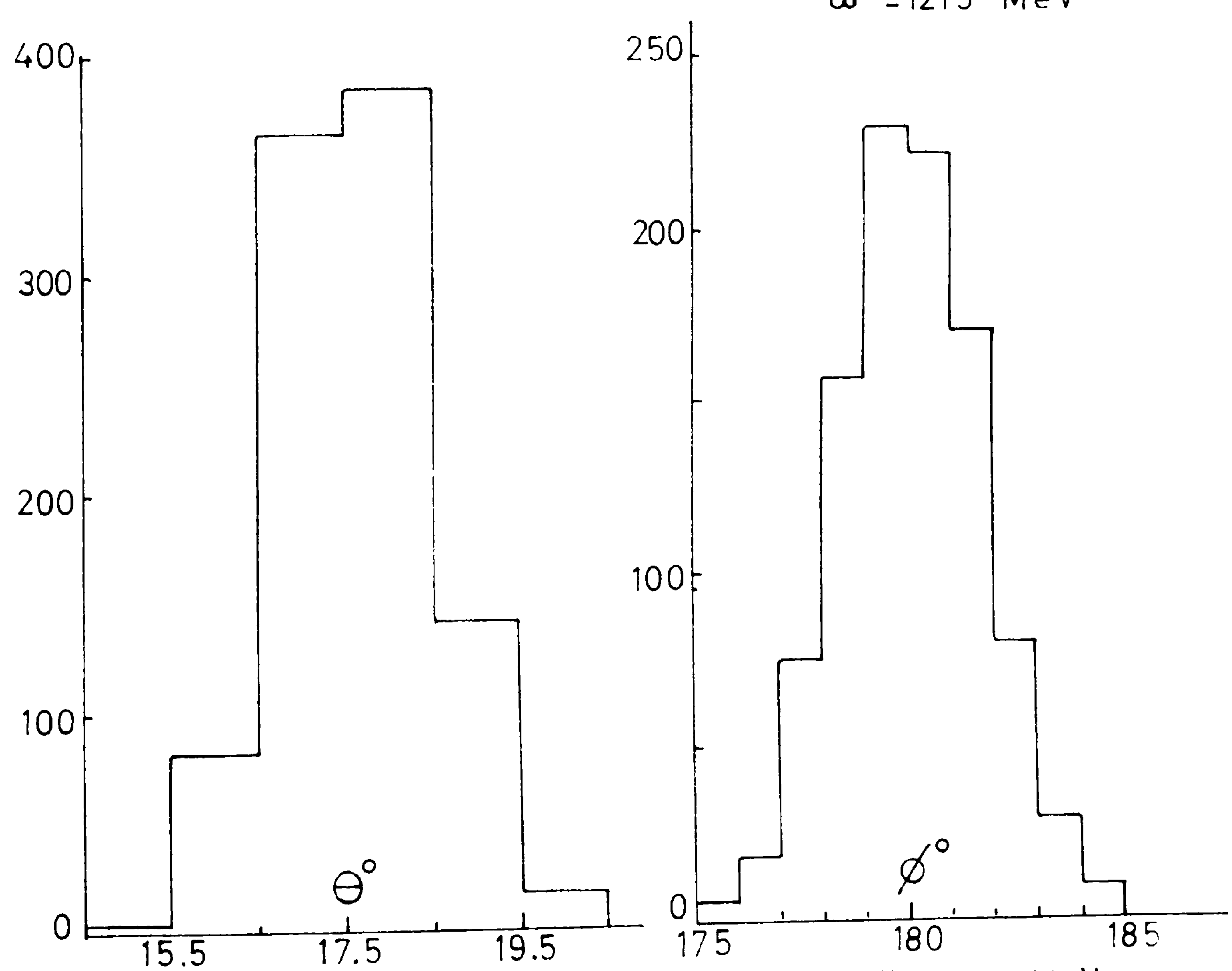

Figure 5.3.13 $172 \leqslant T \leqslant 179$ MeV
$\overline{\omega} = 1275$ MeV

Monte-Carlo Angular Resolutions.

empty subtraction (see p. 5.25) since the same solid angle factors were applied to the target full and target empty data when subtracting the outside cone events.

Monte Carlo calculations were made to establish the accuracy of the values of ω, θ, ϕ calculated by the kinematical reconstruction programme. In these calculations the incident beam energy was given a gaussian profile centred about 990 MeV with a standard deviation of 10 MeV, the angles measured on the scanning table were given a standard deviation of 0.5° and the recoil proton kinetic energy was allowed to vary through $\pm$ 4 MeV about the mean value used in the kinematic reconstruction programme. The results showed the determination of ω to have an uncertainty of about 4 MeV, independent of ω or T, and θ to have a standard deviation between 0.5° and 1.4°. ϕ was completely undetermined when $\theta \sim 0^{\circ}$ but for $\theta \sim 10^{\circ}$ the uncertainty was about $5-10^{\circ}$. (Figs. 5.3.11, 5.3.12, 5.3.13)

5.4 Cross-Sections

The partial cross-section for a particular bin in ω, T can be calculated from the number of events in the bin per unit incident proton. Events from the target walls, chance coincidences and other sources are eliminated by subtracting the target empty cross-section from the target full cross-section.

In this case, however, the bin populations in the corrected histograms of the previous section had to be corrected for scanning efficiencies and biasses. This can be done separately for target full and target empty histograms by calculating the following correction factor.

Let N_0 be the total number of frames taken, $\simeq$ total number of triggers,

N_1 the number of frames scanned and entering the computer,

N_2 the number of frames measured as possible good events, and entering the computer,

N_3 the number of frames made unmeasurable because of camera failure, but scanned and accounted for by the computer,

N_4 the number of frames showing possible good events but with two or more tracks in one or both sets of chambers,

N_5 the number of possible good events in which the proton scattered out of the range chambers, and

m the number of good events scanned and measured but lost because of format errors on the tape, bad punching or some other cause which prevented the computer from reading them.

The m events are an unbiased sample of N_2, the N_3 are an unbiased sample of all scanned events N_1, and the N_4 are an unbiased sample of all possible good events (i.e. of N_2) if their mechanism is as described on pp. 5.5, 5.6. The N_5, however, constitute a biased sample of N_2 since some of them will have had $T > 200$ MeV and their distribution in ω, T will have been strongly affected by the geometry of the chambers. N_5 was much smaller than N_2 or N_3 and events of this type were not corrected for since any such correction would be small and unreliable.

Had the N_3 events been classified m, N_2, N_4 would have been increased by a factor

$$\left(1 + \frac{N_3}{N_1 - N_3}\right)$$

(since m, N_2, N_4 are based on N_1-N_3 classified frames). Similarly m and N_4 contribute to N_2, increasing it by a factor

$$\left(1 + \frac{N_4 + m}{N_2}\right).$$

Thus the correction factor to the population of a given bin is

$$\left(1 + \frac{N_4 + m}{N_2}\right)\left(1 + \frac{N_3}{N_1 - N_3}\right)$$

$$= \frac{N_1}{N_1 - N_3}\left(1 + \frac{N_4 + m}{N_2}\right)$$

The total beam used, however, was for N_0 triggers so there is an additional factor N_0/N_1, making the correction factor

$$\frac{N_0}{N_1 - N_3}\left(1 + \frac{N_4 + m}{N_2}\right)$$

The values of the various N's were

	Target Full	Empty
N_0	8396	3122
N_1	7580	2890

N_2	3451	447
N_3	929	30
N_4	763	104
N_5	114	16
m	52	7
Correction factor	1.56 ± 0.03	1.36 ± 0.04

(The errors are statistical.)

These figures depend on the classification and measurement of events and to check on their accuracy some 1000 frames were rescanned and remeasured, then computed as before. In the second measurement 273 events passed the geometry requirements with 46 having $\theta > \theta_m + 2^\circ$ whereas in the first measurement the figures were 271 and 46. One event which had been inside the $\theta_m + 2$ limit on the first scan was outside on the second, two outside on the second were not classified as good events on the first (the tracks in the isobar chambers were poor) and three which had been outside on the first scan were inside on the second. From this the scanning errors can be deduced as approximately 3/273 or ~ 1% on the "inside cone" figures and 2/46 or ~ 5% on the "outside cone" figures.

The rescan did not alter the numbers corresponding to N_3, N_4 above (these refer to frame types which are readily recognised) so the uncertainty in classification of events only affects N_2, and by about 0.75%. This alters the correction factors by ~ 0.15% to 1.56 ± 0.04, 1.36 ± 0.05.

The figures for N_4 in the table above are based on a rescan, but not remeasure, of less than half the target full data but all the target empty data. The original scan had not classified this type of event unambiguously.

The total beam used was, in units of the full scale deflection of the ionisation chamber, 27.7 (target full) and 28.1 (target empty). One F.S.D. was ~ 2.10^7 protons but this figure was not known accurately and could be in error by $\pm 25\%$.

The ionisation chamber could not be gated off after an event so these total beam figures do not mean very much. The average beam per event must be obtained from counting rates taken without triggering the spark chambers. The average rates were 436 ± 8 triggers/F.S.D. (target full) and 200 ± 7/F.S.D. (target empty). These rates need to be corrected for dead time losses, mainly in the so-called "fast" $C_1\ C_2\ C_4\ \bar{C}_3$ channel which had a rate of ~ 10^3/F.S.D. When taking rates the beam was ~ 10^7 protons/burst or ~ 10^{10} protons sec^{-1}. The fast channel counting rate was therefore ~ 5.10^5 sec^{-1}, well within the capacity of the 10 Mc/s scalers. If the electronic dead time after each count is taken pessimistically to have been 30 nsecs an upper limit on the dead time/sec is $1.5.10^{-3}$ sec. A 0.15% correction to count rates can be ignored.

Taking 1 F.S.D. as equivalent to 2.10^7 protons the beam used was $(38.48\pm0.73)10^7$ protons (target full) and

$(31.24 \pm 1.10)10^7$ protons (target empty).

The number of events in a given bin is related to the partial cross-section for that bin by

$$n_F = A\, B_F\, \sigma_b\, (\rho + d)$$

$$n_E = A\, B_F\, \sigma_b\, (\rho' + d) \qquad (5.4.1)$$

where $n_F(n_E)$ is the corrected number of events for target full (empty),, A is a geometrical factor, B_F (B_E) is the total number of protons for target full (empty), $\rho(\rho')$ is the number of scattering centres (protons) per cm^2 in the liquid (gaseous) hydrogen, and d is the number of scattering centres per cm^2 in the target walls and other background sources. The partial cross-section, σ_b, is given by

$$\sigma_b = \iint_{bin} \frac{d^2\sigma}{d\omega^2 dT} d\omega^2 dT, \simeq \left(\frac{d^2\sigma}{d\omega^2 dT}\right)_{mean} 2\omega\Delta\omega\Delta T$$

with, in this case, $\Delta\omega = 10$ MeV and $\Delta T = 7$ MeV.

Eliminating the unknown quantity d,

$$\sigma_b = \frac{1}{(\rho - \rho')A} \left\{ \frac{n_F}{B_F} - \frac{n_E}{B_E} \right\} \qquad (5.4.2)$$

The beam went through 1.25" of hydrogen, the 3 mm. width of the beam altering this to a mean value of 1.23". The density of liquid hydrogen at its boiling point is 0.0704 gms/cc. while the gaseous hydrogen in the "empty" target had a density of about 0.001 gms/cc. since its temperature would be near but slightly above that of boiling liquid. Thus

$$\rho - \rho' = \frac{(0.0704-0.001).3.125}{1.6714.10^{-24}} \text{ cm}^{-2}$$

and $$A = \frac{0.4}{2\pi} \times \frac{1}{2}$$

since the histograms were normalised to an azimuthal angle about the beam of 0.4 radians and only events in half the possible cone on the isobar side were accepted. The factor $\frac{1}{2}$ assumes that there was no variation of the proton distribution with its azimuthal angle ϕ about the cone axis or, less strongly, that there was no $\cos\phi$ dependence. In fact the ϕ distribution for the events was nearly flat (Fig. 5.4.1). Also, previous experiments (see Refs. of chapter 2) on $pp \rightarrow pn\pi^+$ had shown a variation in ϕ between 0 and π, but would seem to indicate symmetry between $\phi = 0 \rightarrow \pi$, $\pi \rightarrow 2\pi$. No distributions for $pp \rightarrow pp\pi^o$ have been published. Since it proved impossible to extract angular distributions from this experiment this assumption of no asymmetry was the most reasonable.

The values of σ_b calculated are shown as a function of T over the region of T covered in Figs. 5.4.2 (a), (b) and (c). The possible systematic error of ~ 25% on B_E, B_F and the geometric correction uncertainties were not considered when calculating the errors shown.

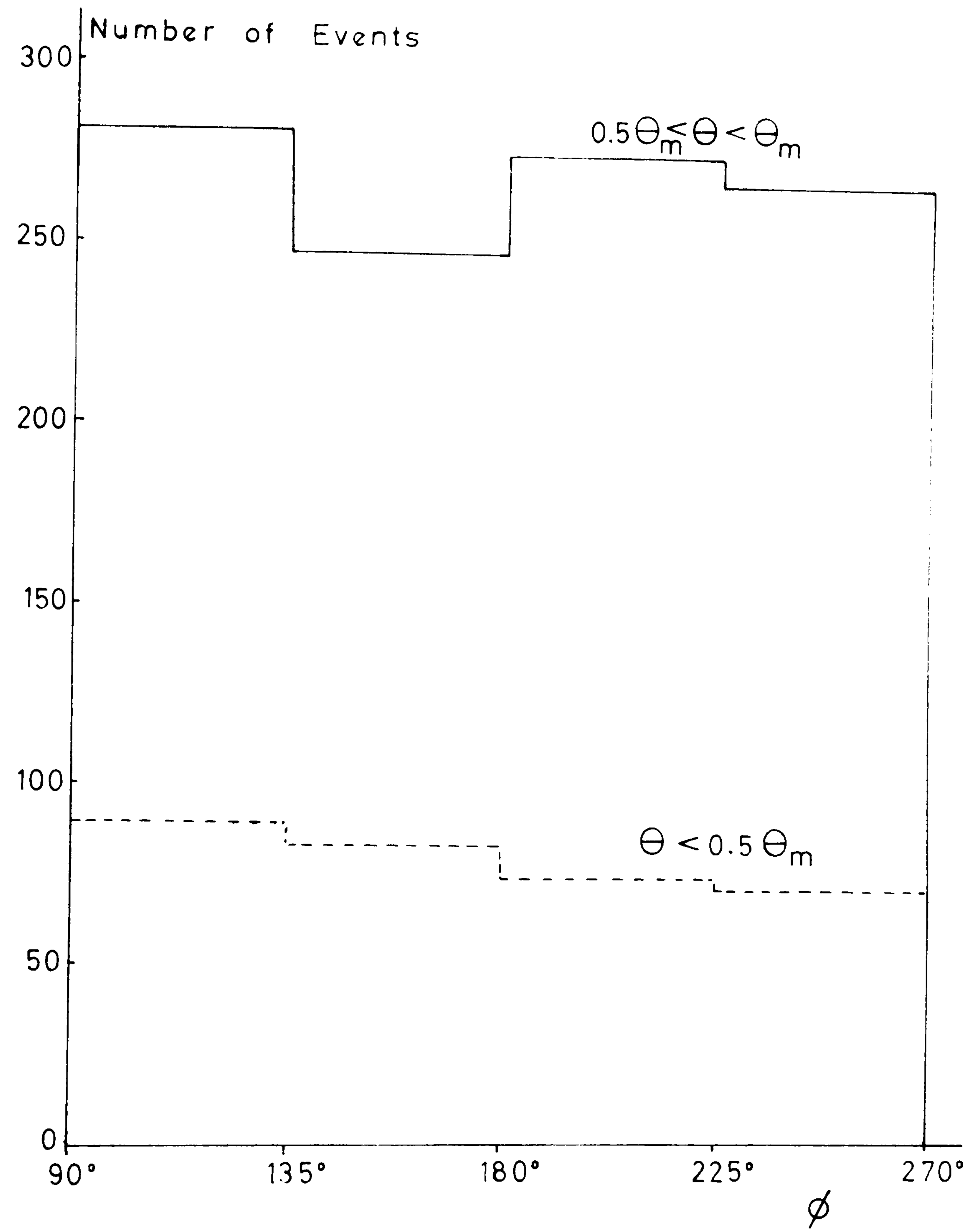

Figure 5.4.1

Distribution in ϕ — all target full events.

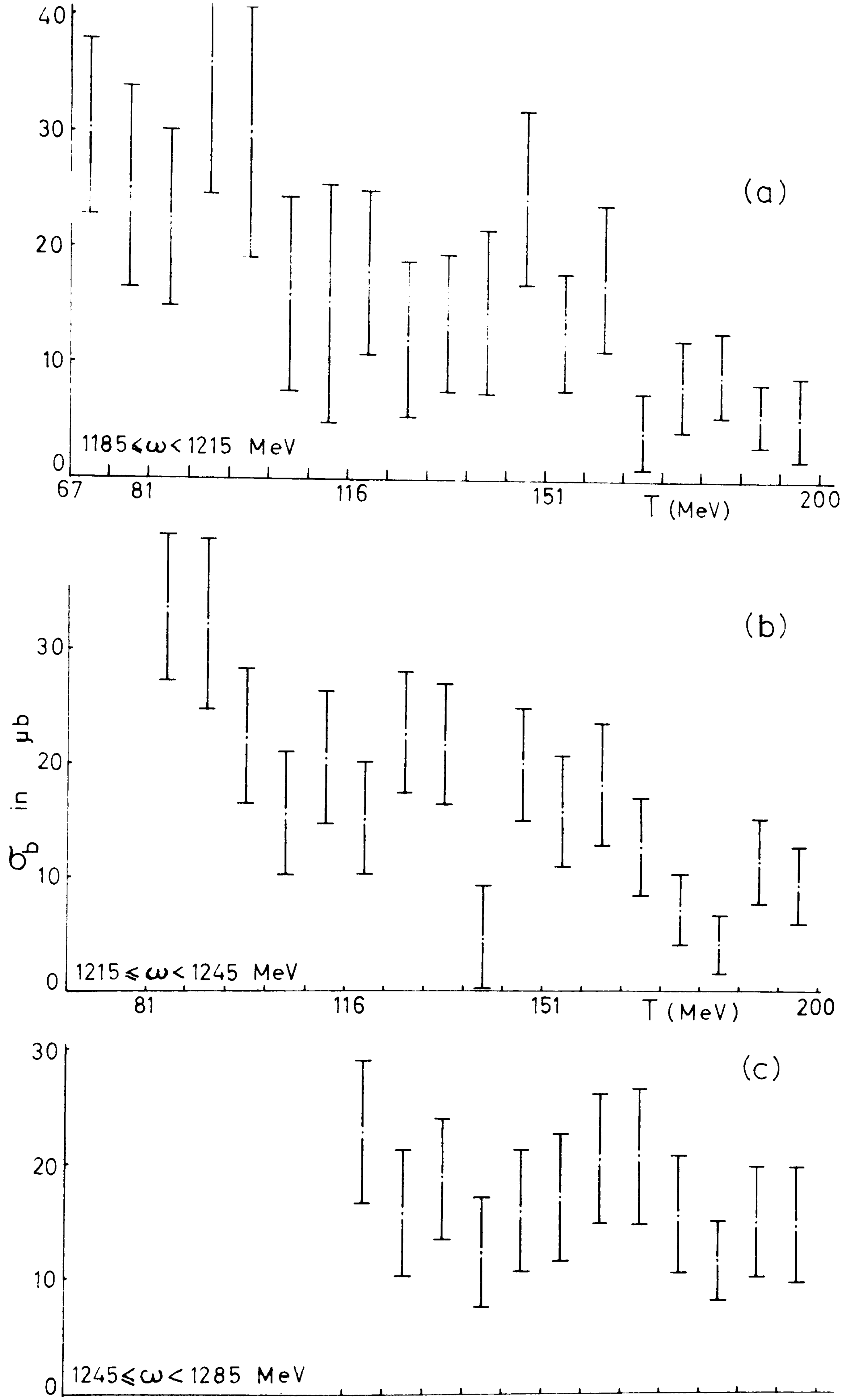
(a)
1185 ≤ ω < 1215 MeV
(b)
1215 ≤ ω < 1245 MeV
(c)
1245 ≤ ω < 1285 MeV
σ_b in μb
T (MeV)
67
81
116
151
200
0
10
20
30
40

Figure 5.4.2

5.5 Uncertainties in the Cross-sections

The principal sources of uncertainty in the measured cross-sections have already been mentioned when the particular stage of the analysis in which they arose was discussed. For completeness, they will be reviewed here.

(a) The poor overall statistics are clearly the largest source of uncertainty. More events could only have been recorded by longer running at the synchrotron, which was not possible. Had there been no trouble with the experiment's electronics or the synchrotron about three times as many events would have been recorded. In addition the cut-offs introduced to obtain an unbiased sample reduced the number of events further, from 2626 to 1019 (target full) and 324 to 115 (target empty), purifying the sample at the cost of statistical accuracy.

(b) The calibration of the ionisation chamber was not known to better than about 25%. This affects the overall normalisation. The chamber was borrowed when the intended beam monitoring system failed and there was insufficient time (the synchrotron failed!) to calibrate it in a low intensity beam against a counter telescope. The method adopted to estimate the number of protons per good event is subject to statistical uncertainties in the average counting rates and in the total number of triggers.

(c) The ionisation chamber was the source of another inaccuracy. Travelling with the beam was a 'halo' of protons scattered out of the beam in the collimator or in the magnets, and not focussed. These protons would miss the target but hit the 12" diameter ionisation chamber. The lead wall immediately in front of the target was intended to remove this 'halo'. How successful it was is not known. The counter scan of the beam profile showed there were few particles in the 'halo' near the target.

In addition the 0.35 $gm.cm^{-2}$ in the beam in the target region would cause about 10^{-3} of the incident protons to interact. Perhaps half of these would miss the ionisation chamber. This would tend to reduce the chamber reading, the 'halo' would tend to increase it so an upper limit on their net effect on the normalisation is 0.1%. This is comparable with the time drift of the ionisation chamber scale due to cosmic rays and stray radiation.

(d) The so-called background events have been discussed at length with the conclusion that they have been dealt with satisfactorily but that there could be a systematic error of ~ -5% in the high ω, T bins.

(e) A few badly measured good events could have been rejected in the geometrical reconstruction. The limits set in the reconstruction programme were generous to allow for this, and from the shape of Fig. 5.3.1 it is clear that no more than four or five events could be expected to have been incorrectly rejected. This is ~ 0.15% of the total, and can be ignored.

Classification and statistical errors contribute to the uncertainty in the scanning correction factor. This was about 3% for target full events and 4% for target empty.

(f) The target position relative to the spark chambers and counters was in doubt by ± 0.2 cm. This affects the relative geometric detection efficiencies, particularly those for events with low ω and T $\simeq$ 120-150 MeV, for which the proton in the range stack goes very near the outer edge of C2 and has a high probability of missing C2. Those bins with low ω values have an uncertainty of between $\pm 40\%$ ($\omega \sim 1185$ MeV) and $\pm 1\%$ ($\omega \sim 1225$ MeV) from this source. Typical values of the relative detection efficiencies are given below:

		Target Position		
ω (MeV)	T (MeV)	1.5 cm.	1.1 cm.	0.8cms
1185 - 1195	74- 81	0.0834	0.1333	0.1708
	116-123	0.0484	0.0980	0.1355
	158-165	0.1399	0.1901	0.2278
1205 - 1215	74- 81	0.3380	0.3667	0.3766
	116-123	0.2441	0.2946	0.3314
	158-165	0.3195	0.3604	0.3755

Events in the lowest ω bin, $1175 \leq \omega < 1185$ MeV were not used because of their low number (11) and this large uncertainty. Bins with $\omega \geq 1225$ MeV are not affected by more than 1% by this uncertainty. It should be noted here that the apparatus was designed for $\omega > 1223$ MeV so the trouble in extending it to lower masses should not be unexpected.

Any error of the order of 0.1 cm. or so in the relative positions of C1, C2 and the spark chambers would result in a comparable uncertainty. This is particularly true of C2, the limiting factor for low ω, low T events. If C2 were displaced 0.1 cm. along its length this would have roughly the same effect as a target movement of 0.2 cm. Since the counters were being moved in an out of position, for checks on delays and discrimination levels, such a displacement is quite credible.

(g) The beam direction was known to be correct to within 0.1 cm, and its width was 0.3 cm. The target is thought to have been centrally situated with respect to the beam, so the maximum error from this source would be 1%.

(h) The experimental resolution of ± 4 MeV in ω, determined by Monte Carlo calculations, would have the effect of smearing out the true distributions, but with a bin width of 10 MeV this should not be too serious. Similarly the inaccuracy in T would result in a slight (1%) movement of events to lower T value, which should be compensated by the 1% range straggling.

(i) There was no evidence that the spark chambers were less than ~ 100% efficient although the resolving time of the isobar chambers must have been near the delay in firing the chambers.

Uncertainties other than those in the absolute normalisation add up to typically a few percent for all but the lower mass bins, where the error is ~ 15%. This is less than the statistical uncertainty from the number of events and the event rate per proton, which is that shown in Figs. 5.4.2 (a), (b) and (c).

(1) J.C.W. Madden D.Phil. Thesis, Oxford University 1964 (unpublished)

Chapter 6 Interpretation of Results

6.1 Distributions in Proton Kinetic Energy

(a) One pion exchange model

The predictions of the OPE model, particularly as developed by Ferrari and Selleri (1), (5), were evaluated for $pp \rightarrow pp\pi^0$ in the kinematical region of interest. Three different approaches were used to evaluate $d^2\sigma/d\omega^2 d\Delta^2$, each taking all four possible diagrams into account.

I "Pole" approximation

This calculation used the "pole" approximation expressions given by Ferrari and Selleri (1), with the contributions of all four diagrams added i.e. the interference terms were neglected. This is not a good approximation, as other calculations (2) have shown, but this can be disguised by the cut-off function used. In evaluating Ferrari and Selleri's expressions $\sigma_{\pi^0 p}(\omega)$ was calculated from McKinley's (3) parametric form of the pion-nucleon phase shifts (chosen because of its easy adaptability to computing).

For comparison with published calculations

$$d\sigma/dT = 2m \int \frac{d^2}{d\omega^2 d\Delta^2} \, d\omega^2$$

was evaluated and, with a cut-off function

$$\frac{1}{1 + \frac{\Delta^2 + \mu^2}{a\mu^2}} \qquad (6.1.1)$$

(as used by Ferrari and Selleri) a good fit to bubble chamber data (4) on the same reaction was obtained with $\alpha = 60$: the curves are shown in Figure 6.1.1. The result of the more elaborate calculation of $d\sigma/dT$ by Ferrari and Selleri (5) is also shown in Fig. 6.1.1. The simple "pole" approximation calculation would appear to fit the data at least as well.

Evaluating $d\sigma/dT$ and $d^2\sigma/d\omega^2 d\Delta^2$ involved considerable numerical integration. For this 6-point Gaussian integration was used and the results checked, in a few cases, against 6 x 6 point Gaussian integration. The differences were never more than a percent or so, so 6-point integration was used in evaluating all integrals. The actual computation was performed on the "Atlas" computer at Harwell.

II "Non-pole" approximation

In addition to using the "pole" expressions of (1) the "non-pole" expressions were evaluated with the physical cross-section $\sigma_{\pi^0 p}(\omega)$ (again calculated from McKinley's phase shifts) used instead of the off-shell $\sigma(\omega, \Delta^2)$, and again the interference terms were neglected. Because the on-shell pion momentum, which appears linearly in the "pole" approximation, is replaced by the much larger off-shell momentum a different cut-off function has to be used. The same form, (6.1.1), was used and with $\alpha=14$ the resultant values of $d\sigma/dT$ (Fig.6.1.1) are very close to those of

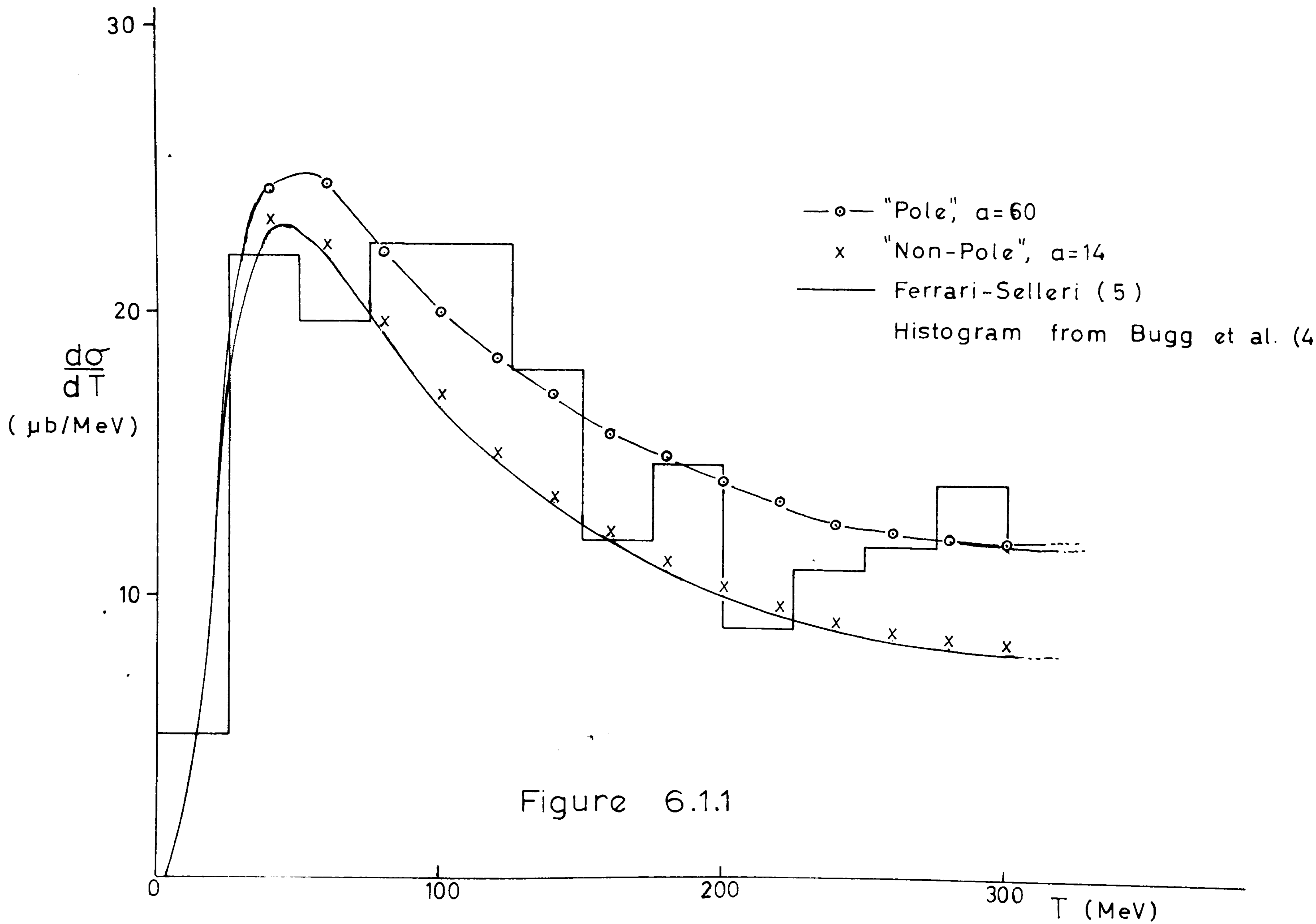
30
20
10
0
100
200
300
T (MeV)
dσ/dT (μb/MeV)
"Pole", a=60
"Non-Pole", a=14
Ferrari-Selleri (5)
Histogram from Bugg et al. (4)

Figure 6.1.1

Ferrari and Selleri while the curve with a=20 fits the data better.

III <u>I,J=3/2 amplitude only</u>

In their latest published calculations (5) Ferrari and Selleri used only the I,J=3/2 amplitude $f_{1+}(\omega)$ for which they had calculated the off-shell correction (6). They included interference between diagrams 1 and 2, 3 and 4 (Fig. 2.3.2), the omission of other interference terms having been justified by Da Prato (2).

With only f_{1+} taken into account the differential cross-section $d\sigma_{\pi^o p}(\omega)/d\Omega$ used in I and II is replaced by $|f_{1+}|^2 (1+3\cos^2\theta)$ and $\sigma_{\pi^o p}(\omega)$ by $8\pi\,|f_{1+}|^2$ (times the Clebsch-Gordan isotopic spin coefficient of 4/9 for $\pi^o p$ elastic scattering). The effect of the f_{1+} correction factor is to multiply the "pole" approximation expression by a factor (6)

$$\left(p_1/q\right)^2\left(1+\frac{\Delta^2+\mu^2}{4m^2}\right)\left\{\frac{(1+3\alpha_o)}{(1+\alpha_o)^3}\right\}^2 \qquad (6.1.2)$$

where $\alpha_o = (\Delta^2+\mu^2)/2m(\omega_r-m)$,

ω_r = resonant mass (N^{*+} mass),

$p_1(q)$ = off-(on-) shell pion momentum.

A cut-off function incorporating the vertex form factors has still to be determined. Ferrari and Selleri used

$$\frac{0.72}{1+\dfrac{\Delta^2+\mu^2}{4.73\mu^2}} + 0.28 \qquad (6.1.3)$$

to obtain a fit to data at several energies (see chapter 2, p. 2.15 ff). (6.1.3) decreases much more rapidly than (6.1.1) as Δ^2 increases. This behaviour is necessary because of the $(p_1/q)^2$ term, which increases with Δ^2. The result of their calculation of $d\sigma/dT$ is that shown in Fig. 6.1.1.

Use of only the I,J=3/2 amplitude $f_{1+}(\omega)$ is justified for $\omega \sim$ 1238 MeV, where it is dominant. In the present experiment the incident proton energy of 990 MeV limited the maximum value of ω to 1382 MeV so the use of only f_{1+} is a reasonable approximation throughout the range of the calculation. Recent unpublished calculations by Selleri (7) have shown that the S-wave I,J=1/2 amplitude increases strongly off-shell, but for $\omega \sim$ 1238 MeV and $\Delta^2 \lesssim 20\mu^2$ is $\lesssim 0.25\ f_{1+}$ and can be neglected, with resultant simplification of the calculation. Its inclusion would alter the calculated values of $d^2\sigma/d\omega^2 d\,\Delta^2$, even in the 1238 MeV region where the cross-terms $\sim f_{0+}^{1/2}\ f_{1+}^{3/2}$ would be significant, so the cut-off function (6.1.3) would no longer give a good fit to data. However, Selleri also gives a new correction factor for the off-shell behaviour of f_{1+}, but no calculations of $d\sigma/dT$ with these new expressions have been made.

The $(p_1/q)^2$ factor in (6.1.2) is a dynamical factor, a consequence of the p-wave nature of the J=3/2 vertex, and was first derived by Salzman and Salzman (8).

Jackson (9) also derived (6.1.2), without the $\{(1+3\alpha_o)/(1+\alpha_o)^3\}^2$ factor, and claimed that the Ferrari-Selleri result was incorrect. Comparison with experiment is difficult because (6.1.3) varies so strongly with Δ^2 that the effect of this extra factor is slight, except at large Δ^2 where the theoretical foundation of the model is suspect, anyway.

A fair test of the OPE predictions is only possible when as much of the physics as possible has been explicitly evaluated. This is the intention of the off-shell a mplitude corrections. When this is done all that are unknown in the expression for the cross-sections are the vertex form factors and the propagator correction function, which can then be determined empirically. The resultant function of Δ^2 should show no variation with incident energy: the fact that Ferrari and Selleri fitted pp inelastic data at several energies with the same cut-off function can be regarded as a success for their model.

This is, however, entirely in accord with qualitative predictions of the absorption model. Here the effects of the absorptive processes in the initial and final channels are inferred from elastic scattering differential cross-sections (10). The pp elastic differential cross-section, plotted as a function of momentum transfer squared, shows little variation between 1 GeV (11) and 7 GeV (12). Hence any absorptive correction calculated from these results would show almost no variation. If, as seems likely, the form-factor function used by Ferrari and Selleri is no more than an empirical representation of the effects of absorption it is hardly surprising that it also shows little variation with energy. It is true that this is no more than a plausibility argument: there is room for work to be done on absorption effects in nucleon-nucleon collisions.

Returning to the data of this experiment, Figures 6.1.2 (a), (b) and (c) show the predictions for σ_b, where

$$\sigma_b(T) = \int_{T-3.5}^{T+3.5} 2m\,dT \int_{\omega_{lim}} \frac{d^2\sigma}{d\omega^2 d\Delta^2}\, d\omega^2$$

calculated from the "non-pole" expressions (II) and the f_{1+} amplitude only equations (3.76 and 3.79 of reference 5). The experimental points are those of Fig. 5.4.2.

The "non-pole" curve is a best fit with α=26: the "pole" expressions, even with very large α, gave cross-sections too low to fit the data. With $\alpha > 100$ the cross-sections are relatively insensitive to α. The quality of the fits is indicated by the table of χ^2 values below:

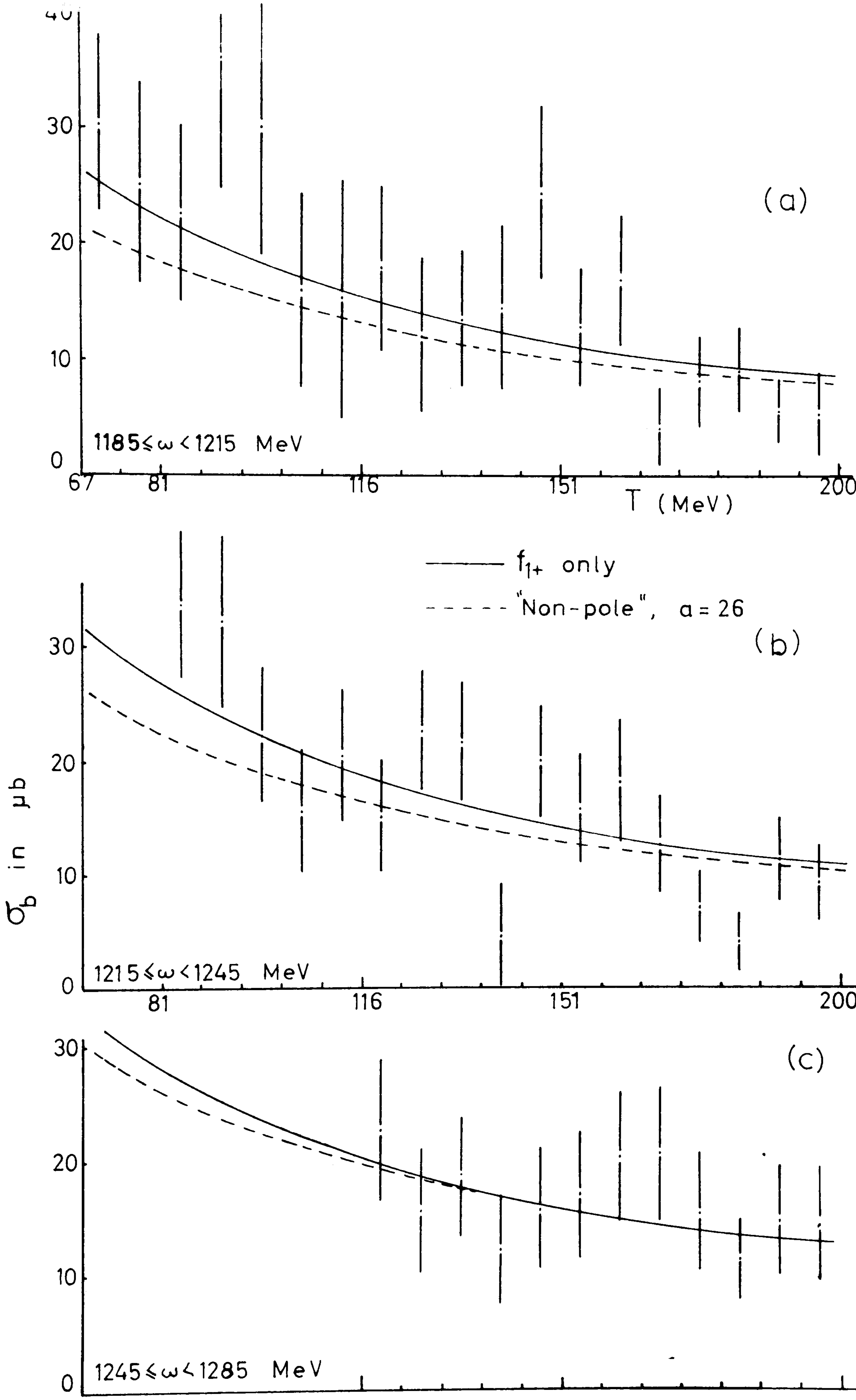

(a)
$1185 \leqslant \omega < 1215$ MeV
T (MeV)
67
81
116
151
200
f_{1+} only
"Non-pole", $a = 26$
(b)
$1215 \leqslant \omega < 1245$ MeV
(c)
$1245 \leqslant \omega < 1285$ MeV
σ_b in μb
0
10
20
30
40

Figure 6.1.2

ω MeV	Number of points	"Pole" $a=100$	"Non-pole" $a=26$	$f_{1+}(\omega)$ only
1185-1215	19	29.6	19.3	14.6
1215-1245	17	34.4	27.3	26.0
1245-1285	12	5.8	4.1	4.1

The f_{1+} only calculation is clearly favoured. In performing this calculation McKinley's (3) expression for δ_{33} was used, then $f_{1+} = e^{i\delta_{33}} \sin \delta_{33}/q$. Ferrari and Selleri used a Breit-Wigner shape, so to check on the compatibility of the two calculations $d\sigma/dT$ was calculated and compared with their published results (reproduced in Fig. 6.1.1). Agreement was to within 2%, with the curve based on McKinley lower than Ferrari and Selleri's.

The agreement between calculation and experiment extends to all three mass bins, suggesting that the systematic errors (not shown in Fig. 6.1.2) may have been set somewhat pessimistically and that the ionisation chamber was reading correctly to within 5-10%. These uncertainties cannot be ignored, however, and their existence weakens the case in favour of the Ferrari-Selleri calculations. However, the curves of Fig. 6.1.2 show that their predictions follow the general slope of the experimental points better, so the conclusion must be that the OPE model provides a good fit to the data of this experiment with

(a) only the I,J=3/2 pion nucleon scattering amplitude, corrected for off the mass shell effects, taken into account, and

(b) a cut-off function (6.1.3) determined by empirical fits to data covering all values of ω, and at several incident proton energies.

In this connection it should be noted that the "non-pole" calculation fitted $d\sigma/dT$ from bubble chamber data best with $\alpha \simeq 20$, but needed $\alpha \simeq 26$ for this experiment's data in the range $1185 \leq \omega < 1285$ MeV, whereas the f_{1+} only calculation fitted both. This can be considered evidence in favour of the off-shell correction factor (6.1.2) or, at least, of the dominant $(p_1/q)^2$ part of it. The basic criticism (see Chapter 2) of the cut-off function procedure must still stand, however.

(b) <u>Chew-Low Extrapolation</u>

An average value of $d^2\sigma/d\omega^2 d\Delta^2$ over the histogramming bin concerned was calculated from the experimental partial cross-section σ_b :

$$\left(\frac{d^2\sigma}{d\omega^2 d\Delta^2}\right)_{av} \simeq \frac{\sigma_b}{\Delta(\omega^2)\,\Delta(\Delta^2)}$$

where $\Delta(\omega^2) = 1215^2 - 1185^2$ MeV^2

$1245^2 - 1215^2$ MeV^2

$1285^2 - 1245^2$ MeV^2

and $\Delta(\Delta^2) = 2m \times 7 = 14m$ (MeV)^2.

Because of the large possible systematic errors in the lower ω bin only data in the two bins $1215 \leq \omega < 1245$, $1245 \leq \omega < 1285$ MeV was used.

The Chew-Low expression $G(\omega, \Delta^2)$ (equation 2.2.6) was calculated from the average value of $d^2\sigma/d\omega^2 d\Delta^2$, with ω, Δ^2 taken at the mid-points of the bin. The resultant values of $G(\omega, \Delta^2)$ are plotted against Δ^2/μ^2 in Figures 6.1.3 and 6.1.4.

In both ranges of ω the lowest Δ^2 value ($8.7\mu^2$ and $12.3\mu^2$) is far removed from the pole ($\Delta^2=-\mu^2$) and the extrapolation could not be expected to be reliable. Least squares straight line fits to the points were made (shown in the figures), the resultant lines being

$$-G(1230, \Delta^2) = (10.7\pm9.5)\Delta^2 + (163\pm114)$$

with $\chi^2 = 19.52$, and

$$-G(1265, \Delta^2) = (20.6\pm9.5)\Delta^2 - (63.6\pm152)$$

for which $\chi^2 = 8.34$.

These give the mean values of $\sigma_{\pi^o p}(\bar{\omega})$ as

$$\sigma_{\pi^o p}(1230) = -152\pm115 \text{ mb}$$

$$\sigma_{\pi^o p}(1265) = 84.2\pm153 \text{ mb.}$$

The former is meaningless, but it is clear from Fig. 6.1.3 and the calculated χ^2 that this line is a poor fit to the points.

If the three points at Δ^2/μ^2=14.45, 18.07 and 18.74 μ^2 in Fig. 6.1.3 are eliminated as the result of large

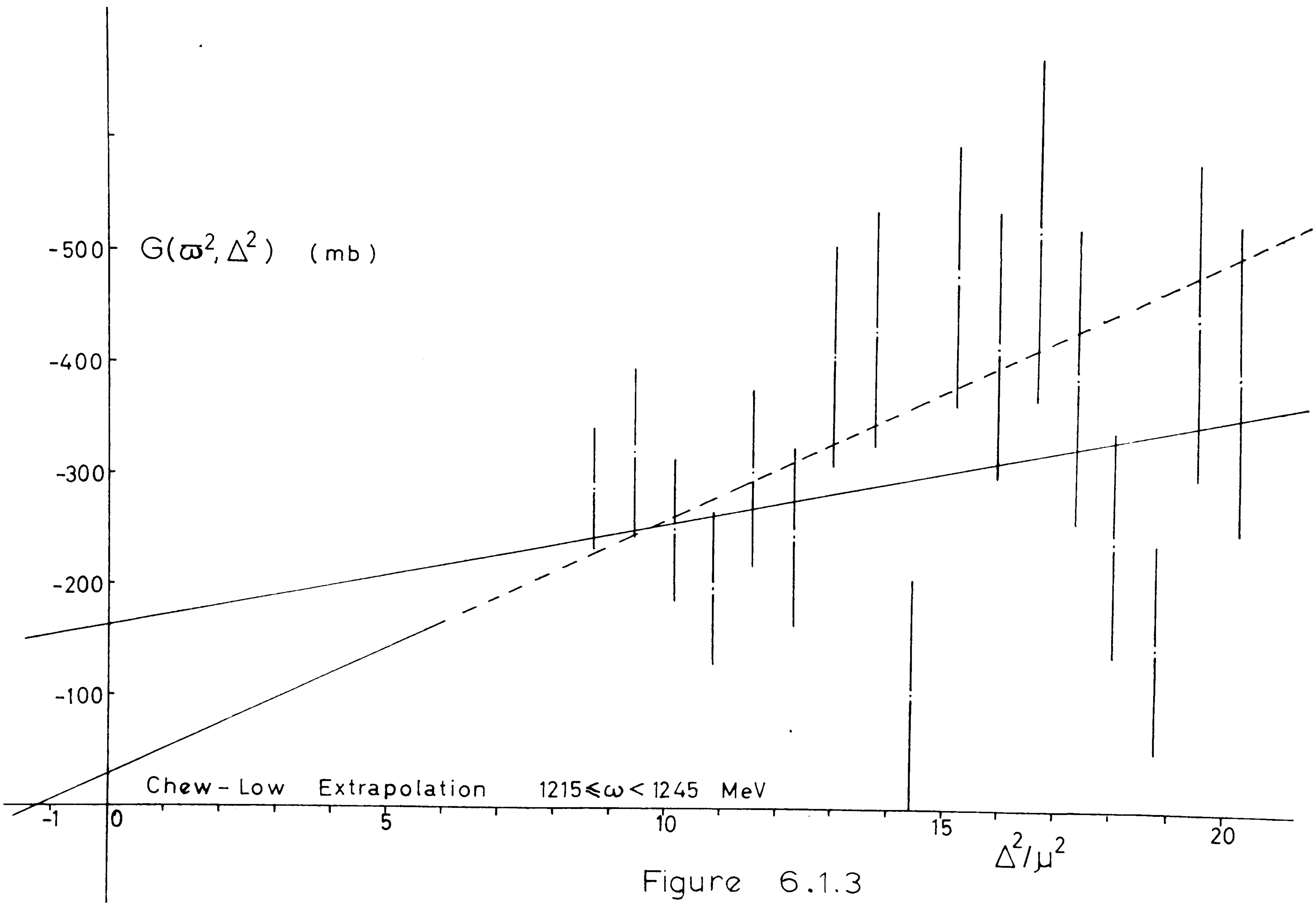

$G(\varpi^2, \Delta^2)$ (mb)
-500
-400
-300
-200
-100
Chew - Low Extrapolation $1215 \leqslant \omega < 1245$ MeV
-1
0
5
10
15
20
Δ^2/μ^2

Figure 6.1.3

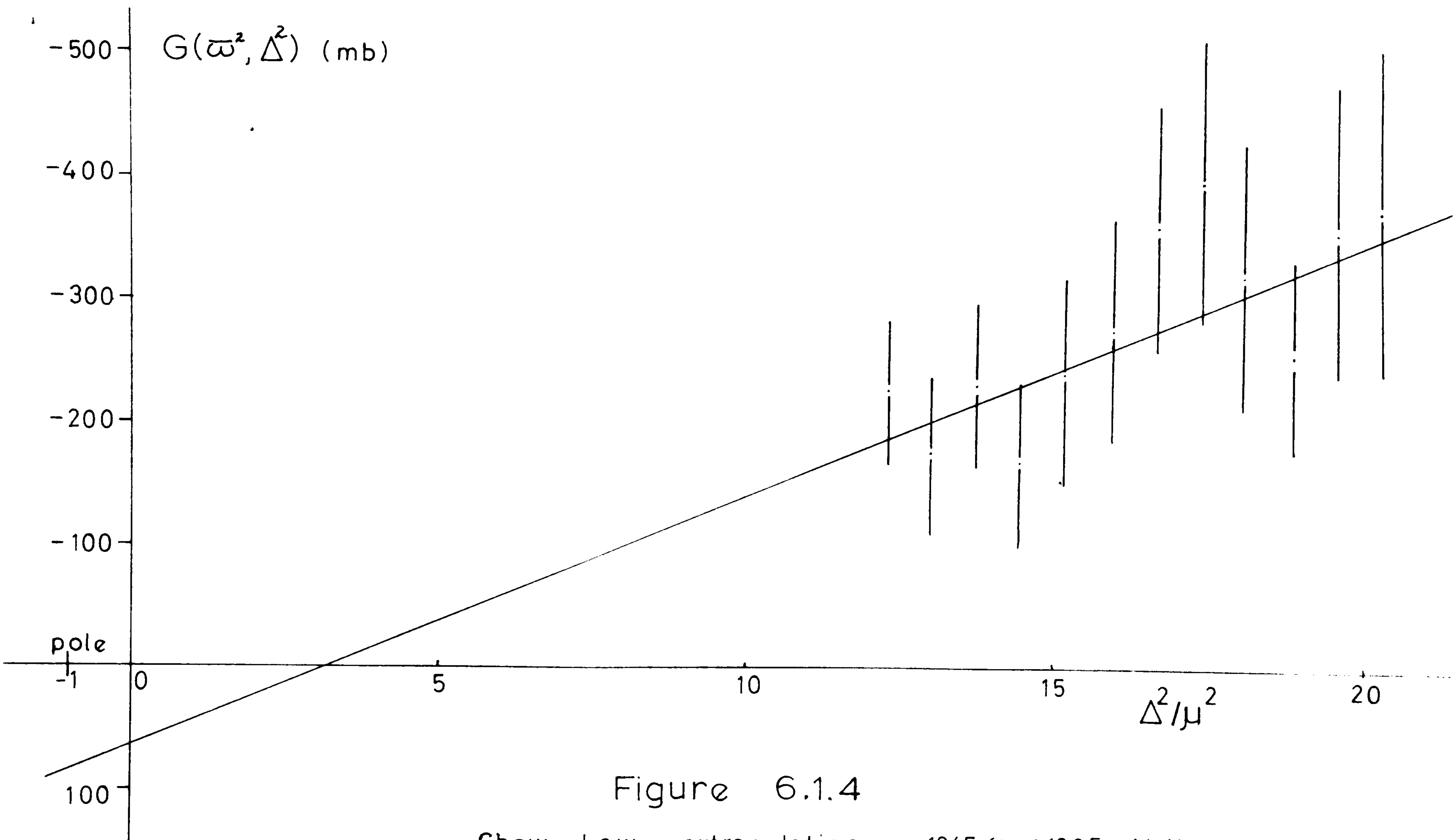

Figure 6.1.4

Chew - Low extrapolation, $1245 \leqslant \omega < 1285$ MeV fluctuations the best line (shown dotted in Fig. 6.1.3) becomes

$$-G(1230, \Delta^2) = (23.2 \pm 8.9)\Delta^2 + (28.05 \pm 132)$$

(χ^2=16.1), giving

$$\sigma_{\pi^o p}(1230) = -5.5 \pm 132 \text{ mb}.$$

Using the phenomenological pion-nucleon phase shifts of McKinley (3) the $\pi^o p$ elastic scattering cross-sections were calculated as

$$\sigma_{\pi^o p}(1230) = 86 \pm 5 \text{ mb}$$

$$\sigma_{\pi^o p}(1265) = 50 \pm 8 \text{ mb}$$

so the Chew-Low extrapolation yields cross-sections consistent, within the extremely large errors, with those expected from pion-nucleon scattering data.

Quadratic and cubic fits to $G(\bar{\omega}, \Delta^2)$ were made, but the results were inconsistent; the curvature of the quadratic fit changed sign when the three 'bad' points for $\bar{\omega}$=1230 MeV were removed, and had different signs for $\bar{\omega}$=1230 MeV and $\bar{\omega}$=1265 MeV. Since data which fits any OPE X form factor expression must extrapolate to $\sigma_{\pi^o p}(\omega)$ at the pole, the above illustrates the chief difficulty of the Chew-Low extrapolation procedure - performing the extrapolation in a meaningful manner. In this case the large range of Δ^2 to be traversed did not help.

6.2 $p\pi^0$ Mass (ω) Distribution

The corrected number of events in 10 MeV intervals of ω, summed over the range 116 MeV $\lesssim$ T < 200 MeV, are shown in Figure 6.2.1. This range of T had to be used because events with T $\lesssim$ 116 MeV did not have full coverage of half the isobar cone for all values of ω.

The rectangles extending the points (circled) in the figure are an estimate of the extreme limits of the effect of any systematic error in the geometrical correction factors; as mentioned in para. 6.1.1(a), these are probably pessimistic. The bins of low ω are very strongly affected.

The solid curve is the prediction of phase space, normalised to the same total number of events. In spite of the considerable errors on the points there is some indication of an enhancement over phase space for $\omega \lesssim 1225$ MeV, in agreement with the expected production mode

$$pp \to N^{*+} p, \quad N^{*+} \to p\pi^0$$

The phase space curve was calculated by a Monte Carlo method. From the expression for the Lorentz invariant phase space integral for a three particle final state

$$R = \int \prod_{i=1}^{3} \frac{d^3 q_i}{2E_i} \delta^4(P_f - P_i)$$

the spectrum of the invariant mass ω of any two of the

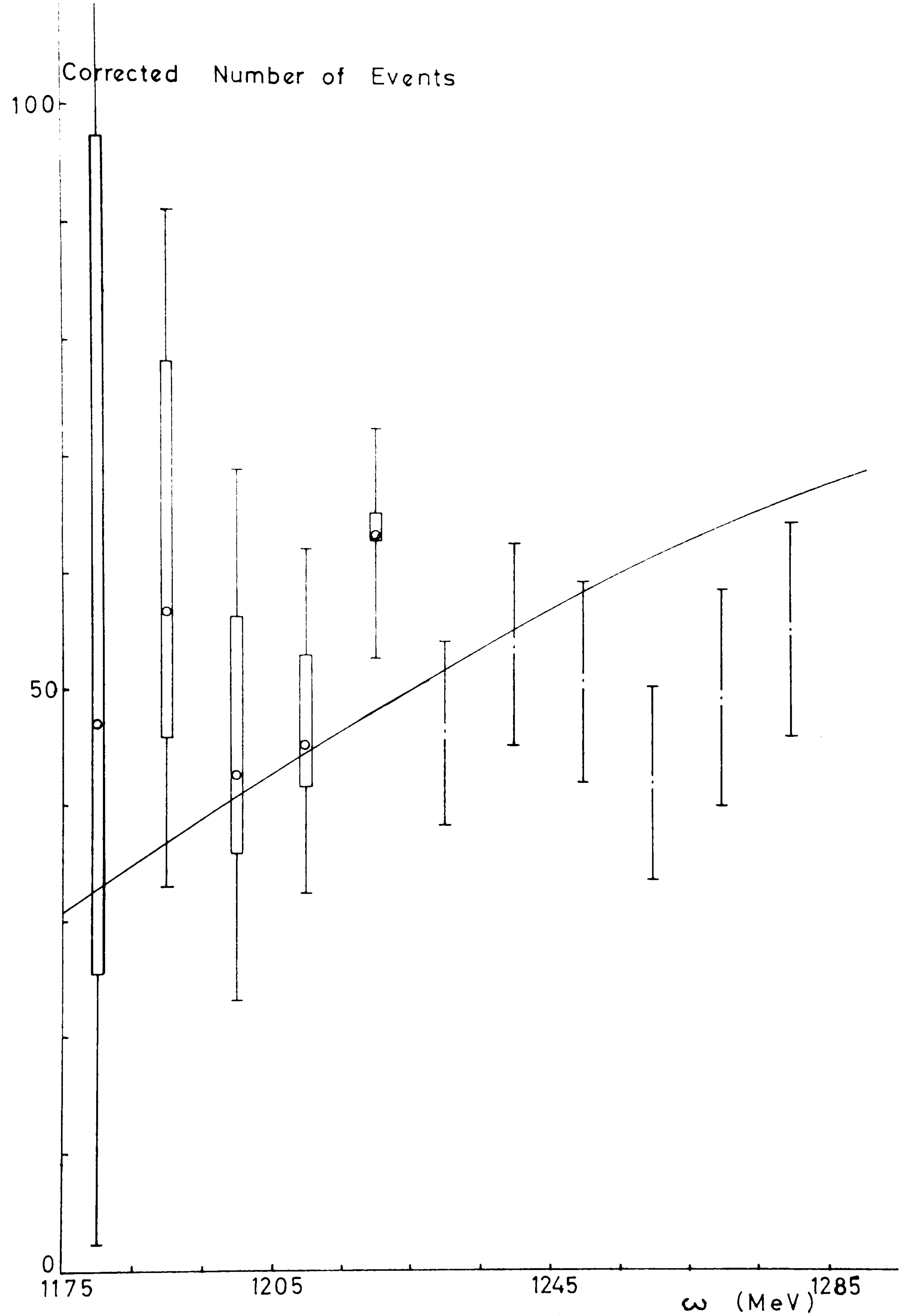

Figure 6.2.1

Mass (ω) Distribution —— 116 ≤ T ≤ 200 MeV particles can be obtained (13). For the case in point

$$\frac{dR}{d\omega^2} = \frac{\pi}{2W^2\omega^2} \left\{ (\omega^2-(m+\mu)^2)(\omega^2-(m-\mu)^2)(W^2-(m+\omega)^2)(W^2-(\omega-m)^2 \right\}$$

where W is the total available energy. In the calculation values of ω^2 were generated with frequency according to this expression. The value of ω^2 fixes the reaction centre of mass momentum of the remaining proton. Random values of the cosine of the reaction centre of mass scattering angle were generated and the proton momentum transformed into the lab. If its lab. kinetic energy was between 116 MeV and 200 MeV the event was accepted. The phase space curve shown is based on 7,000 such events with $1175 \leq \omega < 1285$ MeV, $116 \leq T < 200$ MeV selected from a total sample of 100,000 random events.

6.3 Angular Distributions

An attempt was made to obtain the form of the $p\pi^o$ centre of mass angular distributions of the proton (or pion) from the $p\pi^o$ system. As remarked in chapter 2, para. 2.3, the OPE calculation of this is extremely complicated and has not been made. For this reason the angular distribution extracted would be of limited physical interest but would allow corrections to be made for geometric detection efficiencies on the isobar side.

A Maximum Likelihood approach to the problem was adopted since this could use all the events. For any given event the postulated $p\pi^o$ centre of mass distribution had to be transformed into the lab. frame and the resultant lab. distribution modified to take into account the

(i) inaccuracy in calculating the spatial position of the $(p\pi^o)$ direction (the transformation axis)

(ii) inaccuracy in measuring the direction of the proton in the isobar chambers,

(iii) background or "outside cone" events.

With the OPE model in mind the natural axis in the $p\pi^o$ centre of mass for these distributions is the direction of the virtual exchanged pion, which is opposite to that of the incident proton in the simplest case (diagram 1 of Fig.21.3), and opposite to that of the target proton in diagram 2. It is not uniquely defined in diagrams 3 and 4 in this experiment, since the energy of the proton from the upper, 3 particle, vertex is not measured (it is the one seen in the isobar chambers). Also, in these two diagrams the mass and direction of the $p\pi^o$ from the lower vertex are not uniquely defined so there is no natural axis available, nor is there a well defined transformation direction. For this reason a simple distribution about the $(p\pi^o)$ direction, calculated on the basis of diagram 1, was assumed. The form chosen was

$$a + b \cos\theta^* + c \cos^2\theta^* + d \sin^2\theta^* \cos 2\phi + e \sin 2\theta^* \cos\phi$$

where θ^*, ϕ are the centre of mass spherical polar angles.

For an event of given ω^2, T the transformation of this distribution to the lab. system was quite straightforward, and from this was obtained the likelihood of seeing such an event with the observed lab. angles θ, ϕ, in the absence of resolution and background problems.

The resolution varied from event to event. Most events had $|\theta-\theta_m| \leqslant 2^\circ$ (θ_m is the maximum cone angle defined in Chapter 5), and their calculated likelihood depended very strongly on the resolution function used, so for each event a two dimensional angular resolution function about the observed angles had to be calculated, integrated through space with the transformed distribution and a background probability added. As before, background events were taken to be proportional to the solid angle about the interaction point, with an additional, variable, parameter controlling their proportion relative to genuine events.

Calculating each event's resolution function by a Monte Carlo method proved difficult and the only way to check that the functions obtained correctly represented the experimental situation would have meant generating Monte Carlo events from the observed events, then seeing if the experimental θ/θ_m distribution was reproduced. But to do this the angular distribution would have been needed, so the problem was insoluble without further iterations. This meant that the computing needs were impractical, and the project was abandoned.

References

(1) E. Ferrari and F. Selleri
Suppl. Nuovo Cimento 24, 453 (1962)

(2) G. Da Prato Nuovo Cimento 22, 123 (1961)

(3) J. McKinley University of Illinois Technical
Report 38 (1962)

(4) D.V. Bugg, A.J. Oxley, J.A. Zoll, J.G. Rushbrooke,
V.E. Barnes, J.B. Kinson, W.P. Dodd, G.A. Doran,
L. Riddiford Phys. Rev. 133, B1017 (1964)

(5) E. Ferrari and F. Selleri Nuovo Cimento 27, 1450 (1963)

(6) E. Ferrari and F. Selleri Nuovo Cimento 21, 1028 (1961)

(7) Private Communication via D. Walton

(8) F. Salzman and G. Salzman Phys. Rev. 120, 599 (1960)

(9) J.D. Jackson Nuovo Cimento 34, 1644 (1964)

(10) K. Gottfried and J.D. Jackson Nuovo Cimento 34, 735 (1964)

(11) J.D. Dowell, R.J. Homer, Q.H. Khan, W.K. McFarlane,
J.S.C. McKee Physics Letters 12, 252 (1964)

(12) A.E. Taylor, A. Ashmore, W.S. Chapman, D.F. Falla,
W.H. Range, D.B. Scott, A. Astbury, F. Capocci,
T.G. Walker Physics Letters 14, 54 (1965)

(13) See, for example, O. Skjeggestad Proceedings of the
1964 CERN Easter School Vol. II p.20 (CERN 64-13)